Available online at www.sciencedirect.com
SCIENCE DIRECT®
Physics Reports 383 (2003) 213–297
PHYSICS REPORTS
www.elsevier.com/locate/physrep

Antineutron physics

Tullio Bressani[a,b,*], Alessandra Filippi[b]

[a] *Dipartimento di Fisica Sperimentale, Università di Torino, Via P. Giuria 1, 10125 Torino, Italy*
[b] *Istituto Nazionale di Fisica Nucleare, Sezione di Torino, Torino, Italy*

Accepted 26 May 2003
editor: W. Weise

Abstract

Antineutrons ($\bar{n}$'s) have been used only in the last few years as projectiles for nuclear and particle physics experiments, mainly in the low momentum region. The reason is that, in spite of some undoubted advantages (absence of Coulomb corrections, pure $I = 1$ state for the ($\bar{n}p$) system), the difficulties in obtaining beams of $\bar{n}$'s of suitable intensity and energy definition were overwhelming. The setting-up of suitable beams at BNL and mainly at CERN LEAR (with momentum lower than 400 MeV/c) allowed a first round of interesting experiments.

In this review a summary of the most important experimental issues obtained in this field will be presented. They range from studies on the antineutron annihilation dynamics, intended to shed light on the mechanisms responsible for the particles production as well as for the possible formation of quasi-nuclear nucleon-antinucleon bound states, to meson spectroscopy researches, aiming to identify the existence of new, possibly exotic, resonant structures. Studies on the interactions of antineutrons on nuclei were performed as well, to investigate the nature of the annihilation process (free from Coulomb interactions) inside matter.

Finally, some hints about a possible future development of this research subject will be discussed.

PACS: 13.75.Cs; 14.40.Cs; 12.39.Mk

Keywords: Antineutron beams and detectors; Annihilation dynamics; Meson spectroscopy; Formation experiments

Contents

* Corresponding author. Dipartimento di Fisica Sperimentale, Università di Torino, Via P. Giuria 1, 10125 Torino, Italy. Fax: +39.011.6707324.
E-mail address: bressani@to.infn.it (T. Bressani).

0370-1573/$ - see front matter © 2003 Published by Elsevier B.V.
doi:10.1016/S0370-1573(03)00233-3

1. Introduction

The existence of the antineutron ($\bar{n}$), the antipartner of the neutron expected by the principle of invariance under charge conjugation, was experimentally proved in 1956 [1], one year after the discovery of the antiproton ($\bar{p}$) [2]. In contrast with all other stable anti-particles for which, quite soon after their discovery, suitable beams were designed and experiments were done exploiting their

specific properties to use them as probes, very few attempts were made to operate $\bar{n}$ beams. The reasons were essentially two:

- it was hard to design suitable beams of $\bar{n}$'s, in terms of flux and energy;
- it was believed that the interaction of $\bar{n}$'s with nucleons (in the following denoted as $\mathcal{N}$) and nuclei would not deliver much more information than those obtained by $\bar{p}$'s, for which it was much easier to design and exploit beams of good features.

The situation changed in mid 1980s, when dedicated $\bar{n}$ beams were designed at the BNL Alternate Gradient Synchrotron (AGS) and at the CERN Low Energy Antiproton Ring (LEAR) complex with first pilot experiments, which showed that some unique $\bar{n}$ features, up to that time neglected, could be successfully exploited. They were the following:

(1) the elementary $\bar{\mathcal{N}}\mathcal{N}$ interaction, when studied in the $(\bar{p}p)$ system, both at rest and in flight, is a mixture of $I = 0$ and $I = 1$ amplitudes. The $(\bar{n}p)$ system is, on the contrary, a pure $I = 1$ eigenstate, and only half the number of the interaction matrix amplitudes that must be used to describe the $(\bar{p}p)$ system is needed. Actually, the same information on the $I=1$ isospin amplitude could be obtained by means of the charge-symmetric system $(\bar{p}n)$, produced at rates order of magnitudes larger with deuterium targets. However, the use of deuterium introduces well known drawbacks: interactions occur on neutrons not at rest but having a momentum distribution (the so-called Hulthén distribution [3]) which:
   (a) makes a clear selection of the angular momentum of the initial state difficult;
   (b) induces rescattering effects that may largely distort the final spectra. In first generation experiments at low statistics these effects were tolerated, in more accurate measurements they cannot.

   Both effects are absent if the $(\bar{\mathcal{N}}\mathcal{N})$ system with pure $I = 1$ is formed by $\bar{n}$ interactions on protons;
(2) the $(\bar{n}p)$ interaction is free from Coulomb corrections, that necessarily are present in the $(\bar{p}p)$ interaction and may introduce further complications and ambiguities in the analysis of the data, especially at low-momenta;
(3) experimentally, $\bar{n}$'s do not suffer from energy loss in targets as $\bar{p}$'s and at low momenta this feature may be used to get cleaner results;
(4) at low momenta, typically below 300 MeV/c, only S- and P-waves are present in the elementary $\bar{n}p$ interactions. The relative percentage of the two components varies regularly, from a dominance of S-wave below 100 MeV/c to a dominance of P-wave beyond 200 MeV/c, and is well known from various parametrizations of the $\bar{\mathcal{N}}\mathcal{N}$ interactions. The most popular is the Dover–Richard parametrization, whose representation is shown in Fig. 1.

Following the result of the first experiments on $\bar{n}$ physics, a dedicated $\bar{n}$ beam, to be exploited by the powerful OBELIX (PS201 Experiment) facility at LEAR, was designed and built up. With this facility about 3×10^7 events due to the annihilation of $\bar{n}$'s in the momentum range (50–400) MeV/c on protons and nuclei were collected in the years 1992–1995. The final analysis of these data has been completed only recently, providing very interesting and new results. The purpose of this Review is to present in a coherent way all the work in the field, with historical reminders and more emphasis on the recent issues.

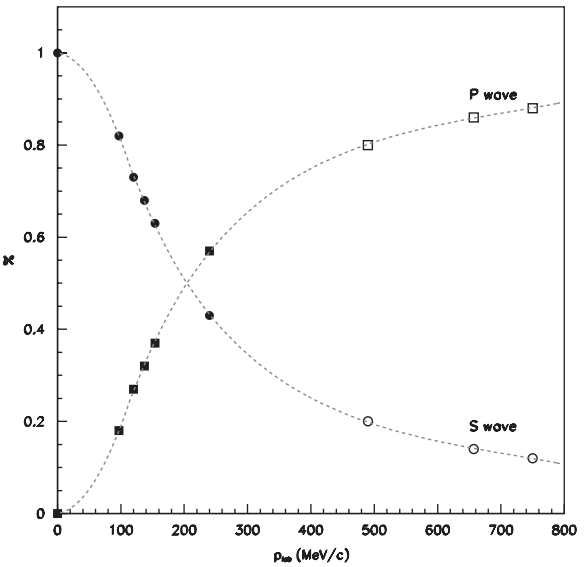

Fig. 1. Trends of S- and P-wave annihilation cross sections according to annihilation models: the full markers (circles for S-wave, squares for P-wave) are from the Dover–Richard model [4], while the open ones have been obtained by Ueda [5] using a version of the optical model.

1.1. Discovery of the antineutron

Cork et al. [1] obtained the first experimental evidence of the existence of the $\bar{n}$ by a clever experiment which in principle pioneers most of the experimental techniques that were afterwards used in the modern set-ups. They say "The purpose of this experiment was to detect the annihilation of antineutrons produced by Charge Exchange (CEX) from antiprotons". Antiprotons of 1.4 GeV/c (discovered just one year before!) were obtained from the 6.2 GeV protons of the Bevalac on an internal target. The flux was ($\sim$ 0.1–0.2) $\bar{p}$/s, in the huge background of negatively charged particles (π^-, μ^-, e^-). To make a comparison, the $\bar{p}$ beam at LEAR had a flux 10^7 times larger, with no contamination of other particles! The setup they used is represented in Fig. 2, with the nice original hand-writings. The description of the principle is simply described by the Authors: "Antiprotons interaction in the first converter X sometimes produce $\bar{n}$'s which pass through the scintillators S_1 and S_2 without detection and finally interact in the lead glass Čerenkov counter C, producing there a light pulse so large as to indicate the annihilation of a nucleon and an antinucleon".

Following several selection and analysis criteria, the Authors conclude to have observed about 60 events due to $\bar{n}$ annihilation, with a CEX cross section $(\bar{p}, \bar{n})$ in carbon of approximately 8 mb, a value largely consistent with later experiments.

1.2. Summary of the main antineutron features

The difficulty in obtaining suitable $\bar{n}$ beams has prevented the direct measurements of the main parameters (mass, magnetic moment, lifetime), assumed to be equal to the neutron's ones by CPT

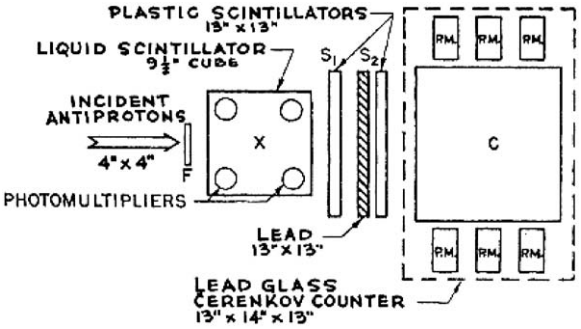

Fig. 2. Set-up of the first experiment for the production of $\bar{n}$'s. From Ref. [1].

invariance (but with opposite sign for the magnetic moment). However, some suggestions were put forward in the discussion of the experimental program at LEAR.

A first, quite complete proposal [6], even from the experimental point of view, was dealing with the measurement of the $\bar{n}$ mass ($M_{\bar{n}}$) to a relative precision of $\sim 10^{-6}$ by a kinematic analysis of the CEX reaction $\bar{p}p \to \bar{n}n$ near threshold ($T_{\bar{p}} = 10$ MeV). The suggested set-up had a symmetrical geometry and was based on detectors for neutrons and $\bar{n}$'s featuring the best state-of-the-art technology for the measurement of the energy of the neutral particles by time-of-flight (TOF) and of their impact point. The set-up was afterwards accomplished and used in the first generation of LEAR experiments on $\bar{n}$ production and detection, described in Section 2, but no attempts to measure the $\bar{n}$ mass were done. On the contrary, a first (and up to now unique) determination of $M_{\bar{n}}$ was achieved by an analysis of the events recorded in the CERN 2 m liquid hydrogen bubble chamber exposed to a low momentum $\bar{p}$ beam [7]. The principle was the same of Ref. [6], i.e. a kinematic analysis of the CEX reaction. The $\bar{n}$ was recognized by the annihilation star in the bubble chamber, the neutron by a measurable proton recoil track, following elastic scattering.

$M_{\bar{n}}$ was evaluated by the expression:

$$M_{\bar{n}}^2 = \{[(p_{\bar{p}}^2 + M_{\bar{p}}^2)^{1/2} + M_p] - [p_{\bar{p}}^2 \sin^2\theta_{\bar{n}}/\sin^2(\theta_{\bar{n}} + \theta_n) + M_n^2]^{1/2}\}^2 - p_{\bar{p}}^2 \sin^2\theta_n/\sin^2(\theta_n + \theta_{\bar{n}}) \quad (1)$$

in which $p_{\bar{p}}$ is the momentum of the interacting $\bar{p}$, $M_{\bar{p}}$ and M_p and M_n the masses of the $\bar{p}$, p and n respectively, $\theta_{\bar{n}}$ the $\bar{n}$ emission angle and θ_n the n one. $p_{\bar{p}}$ was obtained from the momentum of the $\bar{p}$ beam entering the bubble chamber (602.53 ± 0.07 MeV/c), corrected by the momentum lost in the material up to the interaction point. $M_{\bar{p}}$ (assumed equal to M_p), M_p and M_n were taken from the Review of Particle Properties (in the following referred to as PDG, Particle Data Group). $\theta_{\bar{n}}$ and θ_n were measured by a careful scan of the selected events (59 events surviving all the selection criteria, out of 2×10^4 "zero prong" events from $\bar{p}$ between 320 and 590 MeV/c).

The distribution of $M_{\bar{n}}^2$ is shown in Fig. 3. The two gaussian curves represent best fits to the full sample of 59 events (dashed line) and to a reduced sample of 56 events excluding three events lying on the tails of the distribution and likely due to background surviving the selection cuts. However their centroids, giving the final value of $M_{\bar{n}}$, do not differ significantly. The value found by the Authors is (939.586 ± 0.039) MeV, later corrected to (939.485 ± 0.051) MeV [8].

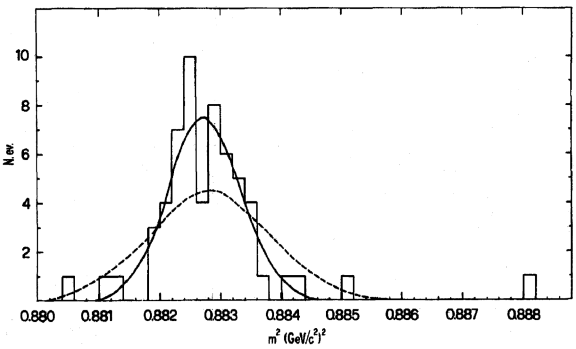

Fig. 3. Plot of $M^2_{\bar{n}}$ for the 59 selected events of Ref. [7].

It must be compared with the most up-to date PDG [9] value of the neutron mass: (939.56533 ± 0.00004) MeV.

In relation to the physics program for a 2–15 GeV/c antiproton ring to be built at CERN, called SuperLEAR, an evaluation of a possible measurement of the $\bar{n}$ lifetime was made [10]. It was based on the possibility of observing $\bar{n} \to \bar{p}e^+\nu_e$ events from ~ 2 MeV/c $\bar{n}$'s decaying in a ~ 100 m long fiducial volume. These low momentum $\bar{n}$'s could have been produced by the CEX reaction of $\bar{p}$'s of some GeV/c on an internal cluster target.

In conclusion, apart from the mass, no direct measurement of the $\bar{n}$ static parameters exist, nor are expected to be performed at forthcoming machines. Their measurement is very hard and not justified by physics arguments. Possible CPT invariance violation in the baryon sector may be searched for in experiments with $\bar{p}$'s (anti-hydrogen), which offer sensitivities at least 10 orders of magnitude better than possible experiments with $\bar{n}$'s.

1.3. Plan of the review

In Section 2 we present a review of the experimental approaches to the $\bar{n}$ production and detection. Special attention is deserved to the $\bar{n}$ beam used in connection to the OBELIX spectrometer, that provided the bulk of physics discussed in the following sections. Concerning the $\bar{n}$ detectors, we describe the general design properties and performances of several early set-ups, and with closer details the detector that has been recently generally used in all experiments requiring $\bar{n}$ recognition, i.e. the calorimeter made by modules of converter/scintillator hodoscope/tracking devices.

In Section 3 we discuss the data on ($\bar{n}p$) total and annihilation cross sections, in the region $p_{\bar{n},\mathrm{Lab}} < 500$ MeV/c, for which just two sets of data were collected. Their relevance to the determination of the best parameters in the $\bar{\mathcal{N}}\mathcal{N}$ phenomenological potential are discussed. The existence of just the $I = 1$ channel helps in the analysis of data.

In Section 4 some details about specific annihilation features will be reported, referring to reactions with inclusive and exclusive many pions final states.

Section 5 reports the behavior of ($\bar{n}p$) annihilations in several two-meson channels, as measured by the OBELIX Collaboration. Whereas some of them are simply described in terms of selected partial waves of the entrance channel, the behavior of the ($\phi\pi^+$) annihilation cross section

compared to the $(\omega\pi^+)$ one shows a strong violation (about a factor 35) of the well known OZI rule. Further evidence for the correctness of such an explanation is provided by the behavior of the $(\eta\pi^+)$ cross section.

Section 6 describes the contribution of $(\bar{n}p)$ annihilations into several mesons (π, K) to meson spectroscopy investigations. The advantage of using selected annihilations with only charged products in the final states allowed the use of powerful 4C kinematic fits in the analysis of the data, with a strong reduction of the background with respect to similar spectra obtained from $(\bar{p}p)$ annihilations. The $(\pi^+\pi^-)$ invariant mass from $\bar{n}p \to 2\pi^+\pi^-$ events shows the presence of large bumps previously observed by similar experiments; the available statistics allowed a detailed partial-wave analysis of the Dalitz plots. A spin-parity analysis was performed as well on the $\bar{n}p \to 3\pi^+2\pi^-$ exclusive sample, providing some insight about the possible decay of the $f_0(1500)$ in many pions. The study of the decay channels of $f_0(1500)$ is very important since there is evidence for a large glue component in its structure [11].

An analysis of the $(3\pi^+2\pi^-\pi^0)$ exclusive channel showed no evidence for the existence of a narrow state at about 1900 MeV appearing in formation, as reported in photoproduction experiments.

Section 7 describes the results obtained in the analysis of $\bar{n}$ annihilations on nuclei. Quite curiously the data bank for ($\bar{n}$-Nucleus) is now more complete and precise than the analogous one for ($\bar{p}$-Nucleus) annihilation. The full data set, for $12 \leqslant A \leqslant 208$ and $50\ \text{MeV}/c \leqslant p_{\bar{n}} \leqslant 400\ \text{MeV}/c$ is well represented by a universal scaling law $\sigma_{\text{ann}} = \sigma_0 A^{0.66} = (66.5 + 2 \times 10^4/p_{\bar{n}})A^{0.66}$ mb, with $p_{\bar{n}}$ in MeV/c.

Section 8 finally summarizes the main results reported in the Review and emphasizes the importance of continuing the experimentation at the future facilities JHJ in Japan and HESR at GSI, Germany.

First short reviews on $\bar{n}$ physics may be found in Refs. [12–18].

2. Antineutron beams and detectors

We may classify the methods for obtaining $\bar{n}$ beams in three categories:

(1) dumping a proton beam (of energy higher than ~ 6 GeV) into a production target and separating the $\bar{n}$'s, into the forward secondary neutral beam, by means of T.O.F. techniques, over large flight paths;
(2) using the CEX reaction in solid targets containing H_2;
(3) using the CEX reaction in a LH_2 (liquid hydrogen) production target.

Concerning the detectors, the physical principle on which they are operated is the detection of the charged (and neutral) products following annihilation in suitable converters. Many realizations of such a simple principle were made, largely based on the technology in use and even more on the performances that could be obtained, concerning the efficiency, the localization properties and the time resolution, i.e. the energy resolution since the energy of the $\bar{n}$'s is measured by TOF. The $\bar{n}$ detectors used directly in the beams were normally of reduced dimensions. Large $\bar{n}$ detectors were built for the study of reactions with $\bar{n}$'s in the final state, with the need of large angular coverages and normally of large halls. We shall describe these major set-ups for completeness, even though the physics results will not be discussed in this review, where we deal with $\bar{n}$'s as probes.

2.1. Early setups for antineutron beams

The idea of obtaining $\bar{n}$ beams directly from external production targets at high energy proton accelerators is certainly the most appealing one, since production rates comparable to those with $\bar{p}$'s can be expected. However, as no magnetic selection can be applied, $\bar{n}$'s can be present in a neutral beam since the production target, with an overwhelming contamination from other particles (neutrons, photons). Furthermore, in order to select $\bar{n}$'s in a definite momentum band, the only technique that could be used is based on TOF, the START signal being given by the radio-frequency signal during the flat top.

A feasibility study of such a technique was performed by Brando et al. at the AGS Proton Synchrotron [19]. An $\bar{n}$ detector consisting of an array of plastic and liquid scintillators, able to identify $\bar{n}$'s by the multiplicity of the annihilation products was used. The selection was relying essentially on the good timing properties and stability of the associated electronics. The Authors reported a production intensity of $(3 \times 10^{-3.2-24p_{\bar{n}}+27p_{\bar{n}}^2})$ $\bar{n}/p \cdot \mathrm{GeV}/c \cdot \mathrm{sr}$ in the forward direction, with $\bar{n}$ from ~ 0.3 to 1.0 GeV/c.

In spite of the inherent appeal of such a technique, no further attempts were made to obtain better beams and to try to perform some physics experiment. The experimental reason is that in spite of the progress in detectors and electronics, the elimination and control of backgrounds were not such as to allow precise measurements.

The first $\bar{n}$ beam obtained by the CEX reaction in a polyethylene target was produced by Gunderson et al. [20] at the Argonne ZGS. A 1 GeV/c single-stage separated $\bar{p}$ beam was brought to rest in a CH_2 target, sliced into three pieces interleaved by scintillators, which defined the slice where the reaction occurred. In this way, the broad momentum band of the $\bar{n}$'s produced in the forward direction by CEX could be divided into four intervals. Thick transmission targets (heptane liquid scintillator, with a H/C ratio of 2.115, and carbon for subtraction) were placed downstream the $\bar{n}$ production target. A simple $\bar{n}$ calorimeter, made of 2.5 cm Iron plates interleaved with scintillator ones was used to detect $\bar{n}$ annihilations, and to measure the $\bar{n}$ energy by TOF. With this set-up total σ_T and annihilation σ_{ann} cross sections for $\bar{n}$ on protons and carbon nuclei were measured. Unfortunately the measurements were affected by very large statistical errors (more than 50%) for the lowest $\bar{n}$ momenta, due to the low $\bar{n}$ flux. However, the experiment pioneered most of the experimental techniques used afterwards at BNL (see Section 2.2).

The first $\bar{n}$ beam obtained by the CEX reaction in a LH_2 target was operated at the LEAR complex at CERN by the PS178 experiment, a pilot set-up for $\bar{n}$ production and detection [21]. The excellent features of the $\bar{p}$ beams delivered by LEAR (momenta ranging from 0.1 to 2.0 GeV/c, with intensities up to more than 10^6 $\bar{p}$ s^{-1} and no contamination from other particles) allowed to perform such an attempt. The complication of using a cryogenic LH_2 target instead of a solid one containing H_2 was motivated by at least two reasons:

(1) the $\bar{n}$'s production rate on a LH_2 target is a factor of four larger than on a solid CH_2 one. We will discuss this point in Section 2.3;
(2) a tagged $\bar{n}$ beam may be designed by exploiting the CEX reaction two-body kinematics and measuring the neutron direction and energy.

Fig. 4 shows the kinematics for the CEX reaction below 600 MeV/c. The threshold is at 98.58 MeV/c (in the following we will shorten it to 98 MeV/c for the sake of brevity). Since the masses of both

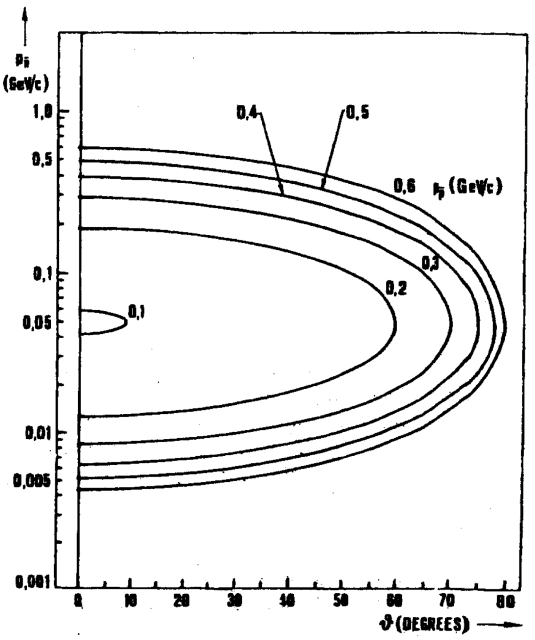

Fig. 4. Kinematics for the CEX reaction. At any incident $\bar{p}$ momentum (shown on the curves) for a fixed lab angle there are two solutions for the $\bar{n}$ momentum. From Ref. [21].

initial and final particles are equal, at any incident $\bar{p}$ momentum for a fixed laboratory angle there are two solutions for the $\bar{n}$ momentum (and, correspondingly, for the n momentum).

There are two sets of measurements for the total cross section for CEX below 600 MeV, from Hamilton et al. [22] and from Brückner et al. [23]. They show a 30% difference below 250 MeV/c as shown in Fig. 5a, i.e. in the region which is mostly important for the accomplishment of low-momentum $\bar{n}$ beams. The two sets of data were parametrized with the same fitting function, but different sets of parameters, both of them describing the data quite well, were obtained [24]. The two parametrizations give results remarkably different (a factor of 3) near threshold, as shown in Fig. 5b. Later, it was found by a new set-up for an $\bar{n}$ beam (OBELIX, see Section 2.3) that only the data by Hamilton et al. [22] could reproduce well the measured $\bar{n}$ spectra.

On the other hand, the differential cross sections for the CEX reaction were measured in the low momentum region by Nakamura et al. [25] and by Brückner et al. [23]; they are shown in Fig. 6a and b, at two different $\bar{p}$ incident momenta, 505 and 183 MeV/c. They are forward peaked but the effect decreases at low momenta of the incident $\bar{p}$.

If we stop a $\bar{p}$ beam of a given initial energy T_0 in a LH_2 target, it produces $\bar{n}$'s via CEX during its slowing down to 98 MeV/c. For $T_0 \simeq 45$ MeV ($p_{\bar{p}} \simeq 300$ MeV/c), the range is about 13 cm of LH_2. Of course the $\bar{n}$'s spectrum is broad, and its shape depends on the emission angle $\vartheta_{\bar{n}}$.

Referring to Fig. 7, where the experimental layout of the PS178 experiment is sketched, it is clear that it is possible to define unambiguously a "beam" of $\bar{n}$ of known momentum and direction by detecting the associated neutrons by a fine-grained hodoscope featuring good timing and localization properties. The $\bar{n}$ Veto, a tank of liquid scintillator, was used to eliminate $\bar{n}$'s elastically scattered by

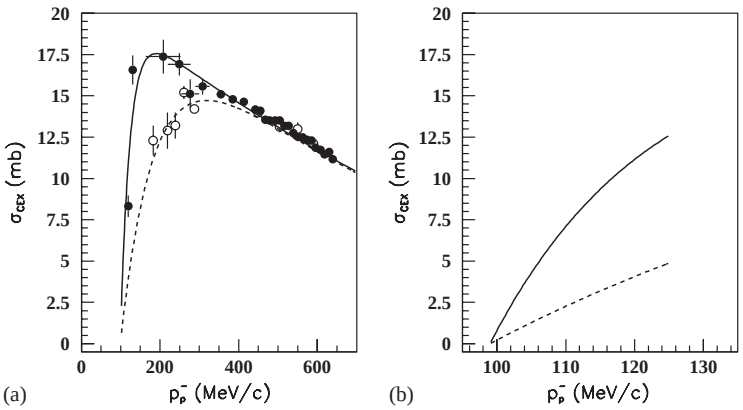

Fig. 5. (a) *CEX* cross sections data: black circles by Hamilton et al. [22], open circles by Brückner et al. [23]. The two sets of data were parametrized with the fitting function $(a + b/p)(1 - \exp(c(p - 98.58)))\exp(\mathrm{d}\,p)$, where a, b, c, d are free parameters and p is the $\bar{\mathrm{p}}$ momentum, providing the solid curve with the set of parameters: $a = 21.4$ mb, $b = -0.011$ mb MeV/c, $c = -0.041$ (MeV/c)$^{-1}$, $d = -0.36 \times 10^{-3}$ (MeV/c)$^{-1}$, and the dashed curve with the set of parameters: $a = 23.7$ mb, $b = -0.0078$ mb MeV/c, $c = -0.01$ (MeV/c)$^{-1}$, $d = -0.8 \times 10^{-3}$ (MeV/c)$^{-1}$. (b) Magnification of the two curves near threshold. From. Ref. [24].

the neutron hodoscope, that could fake the true neutrons from the CEX reaction. It had a detection efficiency for $\bar{\mathrm{n}}$ of $\sim 90\%$. Details on the neutron hodoscope may be found in Ref. [26].

The $\bar{\mathrm{n}}$ momentum band and the spatial distribution for such a tagged beam depend critically on the position of the neutron hodoscope. The best compromise gave a $\bar{\mathrm{n}}$ beam with the spectrum represented in Fig. 8, in which a comparison is made among the momentum distribution of the $\bar{\mathrm{n}}$'s as expected by Monte Carlo simulation, the one reconstructed by neutrons tagging and finally the one directly measured by means of an $\bar{\mathrm{n}}$ calorimeter that will be described in Section 2.4. An acceptable agreement is found. The total (i.e. integrated over the whole momentum spectrum) rate of tagged $\bar{\mathrm{n}}$'s was $(8.02 \pm 0.03)10^{-5}\,\bar{\mathrm{n}}/\bar{\mathrm{p}}$, in agreement with the expectations. It must be noted that in the above spectrum the energy of each tagged $\bar{\mathrm{n}}$ was known to a precision better than 1 MeV.

With the tagged $\bar{\mathrm{n}}$ beam an attempt to measure $\sigma_T(\mathrm{n\bar{p}})$ and $\sigma_{\mathrm{ann}}(\bar{\mathrm{n}}\mathrm{p})$ by inserting a second larger LH_2 transmission target between the production target and the $\bar{\mathrm{n}}$ detector was made. After a preliminary analysis [27], the final results were never published since meanwhile other experiments produced better data. On the other hand, the tagged $\bar{\mathrm{n}}$ beam set-up provided interesting physics data on ($\bar{\mathrm{n}}$-Nucleus) annihilation and, most of all, pioneered the $\bar{\mathrm{n}}$ beam for OBELIX and the $\bar{\mathrm{n}}$ detection technique with tracking.

2.2. The BNL source

The $\bar{\mathrm{n}}$ beam put into operation at BNL by the E-767 Experiment [28] represents the best achievement of the production method for $\bar{\mathrm{n}}$'s by CEX in solid targets, and featured several techniques already used in the ZGS installation [20]. Fig. 9 shows the layout. $\bar{\mathrm{p}}$'s were provided by the Low Energy Separated Beam (LESB II) at the BNL AGS, operated at transport momenta of 505 and 520 MeV/c. The lead collimator eliminated pions and muons which were not directly in the beam. The strong π^- contamination ($200\pi^-/\bar{\mathrm{p}}$) was eliminated by TOF between a beam hodoscope not

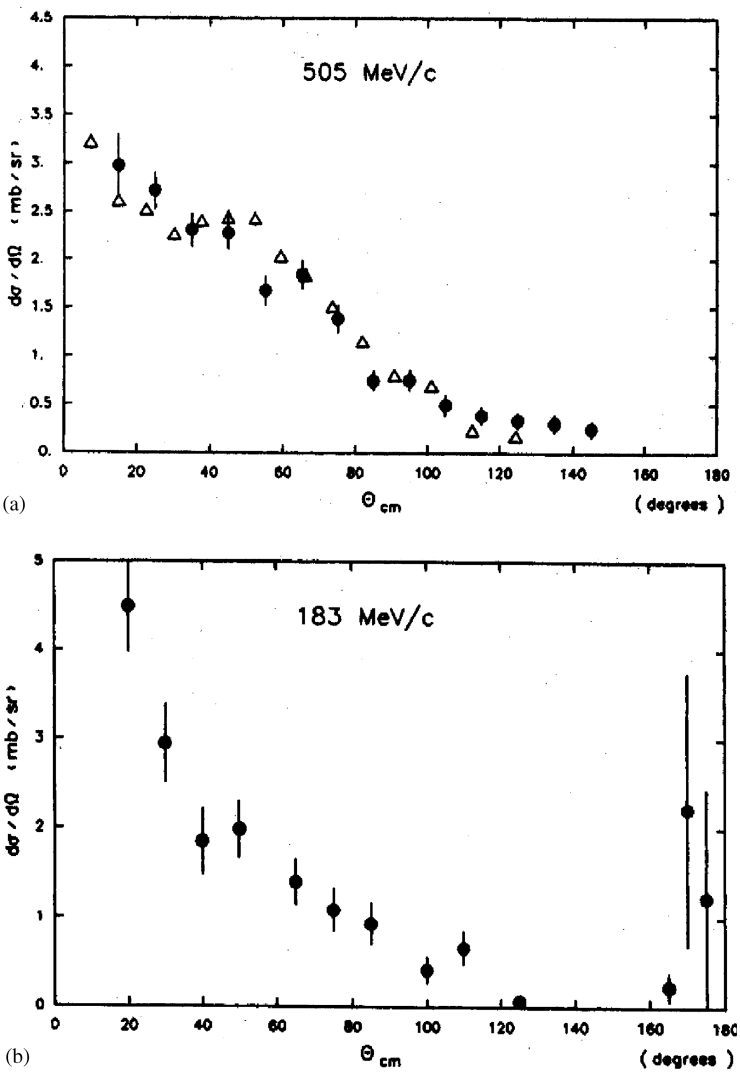

Fig. 6. The differential charge-exchange cross section at 505 MeV/c (a) and at 183 MeV/c (b). The full circles are the data from the experiment by Brückner et al. [23], the open triangles represent the data of Nakamura et al. [25].

shown in the figure and the scintillator S_2 and the $\bar{p}$ trajectory was determined by means of the proportional wire chambers PWC1 and PWC2. $\bar{n}$'s were produced by CEX of $\bar{p}$'s in the source, which was composed of 20 scintillator counters (T counters) stacked along the beam direction. Its overall thickness was sufficient to degrade the $\bar{p}$'s energy so that they stopped close to the end of the stack. Each T-counter acted as a source of $\bar{n}$'s (from interaction on both C and H nuclei in the scintillator), as well as a detector for tracking the $\bar{p}$'s as they passed through it.

The last counter hit provided information of the time and position of the $\bar{n}$ production. This ultimately enabled the momentum of the $\bar{n}$ to be determined, taking into account the CEX kinematic shown in Fig. 4.

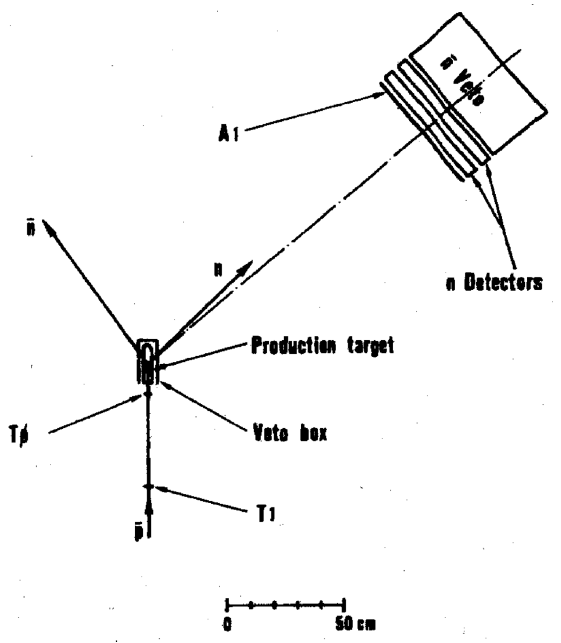

Fig. 7. Experimental layout of the tagged n̄ beam. From Ref. [21].

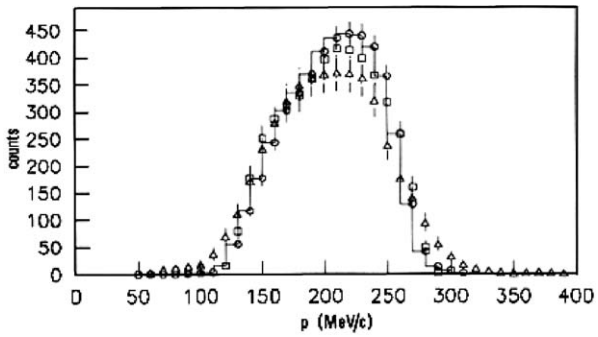

Fig. 8. Momentum distribution of the tagged n̄'s as expected by the Monte Carlo simulation (open circles), as reconstructed by the n tagging (open squares) and as measured by the n̄ detector (open triangles). From Ref. [21].

Since the momentum threshold for the CEX reaction is 98 MeV/c, n̄'s can only be produced by p̄'s in flight. Since only a few percent of the incident p̄'s produce n̄'s, the remainder annihilating either in flight or at rest, these reactions were rejected by a veto system arranged around four sides of the source (Veto Box B in the figure). The Veto Box consisted of three layers of lead and scintillators to identify charged particles and γ rays.

The n̄ beam was monitored by a calorimeter downstream the LH_2 target that will be described in Section 2.4. The n̄ momentum spectrum obtained by this set-up is shown in Fig. 10 and spans the region (100–500) MeV/c. The n̄ event rate was $\sim 2 \times 10^{-1}$ s^{-1} and with a LH_2 target

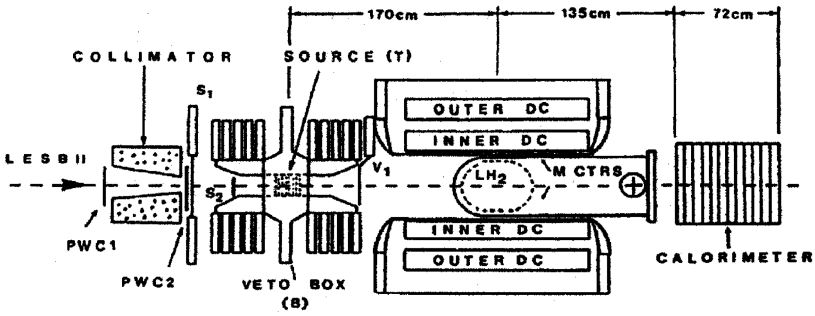

Fig. 9. Schematic plan-view of the E-767 apparatus at BNL. From Ref. [28].

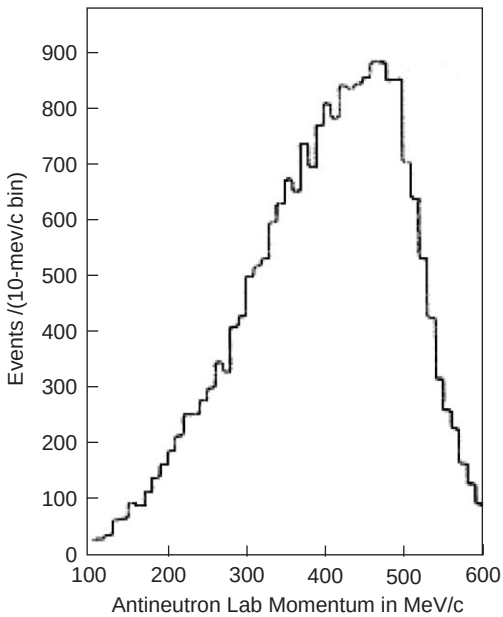

Fig. 10. Antineutron momentum spectrum obtained in the E-767 Experiment at BNL, from Ref. [28].

(35 cm long, 40 cm diameter) it was possible to measure $\sigma_T(\bar{n}p)$ and $\sigma_{ann}(\bar{n}p)$, as will be discussed in Section 3.

2.3. The CERN LEAR source

In the design of the second-generation LEAR experiment OBELIX (PS201) [29], a powerful, general purpose, magnetic spectrometer subtending a solid angle of $\sim 3\pi$ and able to detect all particles produced in the annihilation of antinucleons, the use of a new $\bar{n}$ beam [30] was programmed. It was set into operation for the first time in 1990 and afterwards extensively used in different

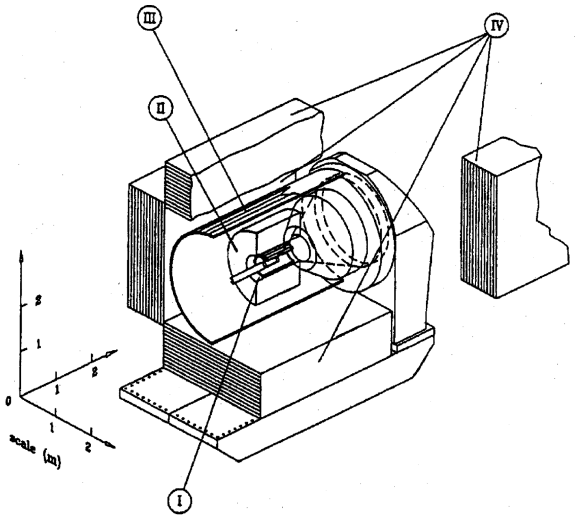

Fig. 11. Schematic representation of the OBELIX spectrometer: Internal (TOFINO) (I) and External (TOFONE) (III) scintillator barrels; half JDC (II) and Electromagnetic Calorimeter (HARGD) (IV). From Ref. [30].

versions. About 3.5×10^7 events were collected, producing the bulk of physics results discussed in this Review.

As discussed in Section 2.1 the best way to obtain a clean $\bar{n}$ beam, at low momenta ($\leqslant 400$ MeV/c), well defined in energy and direction, is the CEX reaction on protons of a LH_2 target, with $\bar{n}$ tagged by measuring the energy and impact position of the associated neutron. Limits of the tagging neutron method are the intensity of the $\bar{n}$ beam and the fact that $\bar{n}$ production at 10–20° angles has to be used.

The structure of the OBELIX spectrometer, as well as its location in the experimental area of LEAR, imposed several mechanical constraints preventing the use of the tagging technique. Fig. 11 shows a sketch of the spectrometer, described in detail in Ref. [31]. The detector components were installed between and around the poles of the Open Axial Field Magnet (OAFM), previously used at the CERN ISR (Exp. R807) [32]. The OAFM characteristics were a gap of 1.5 m, a field of 0.6 T (in the center), a radial field homogeneity of $\sim 1\%$. The poles had a conical shape, with a round hollow cone with a diameter of 50 cm.

The targets in which annihilation of $\bar{N}$ occur (gaseous, liquid, solid) were generally located at the center of the magnet. The first detector encountered by the particles emitted in the annihilation was a barrel-shaped array (TOFINO) of 30 scintillators, $80 \times 3 \times 1$ cm^3, each viewed at both ends by XP2982 photomultipliers (PM). Besides playing a crucial role in the first level triggering strategy of OBELIX, TOFINO was also very important in defining the $\bar{n}$ beam features. The momenta of the charged particles ($\pi^{\pm}, K^{\pm}$) produced in the annihilations were measured by a set of two semicylindrical Jet Drift Chambers (JDC's), equipped with 3444 wires. JDC's, moreover, allowed the determination of the annihilation vertex and also the event topology. An external barrel of scintillators (84 elements, $9 \times 4 \times 300$ cm^3 each), viewed at both ends by XP2020 PM's and named TOFONE, allowed the first level trigger on multiplicity and on particle identification by TOF. An electromagnetic calorimeter, named HARGD, enclosed on four sides by wall-shaped

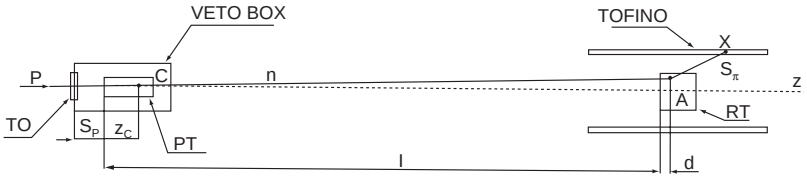

Fig. 12. Scheme of the $\bar{n}$ beam arrangement (not to scale) of the OBELIX Experiment, from the production to the annihilation; for symbols definition see text. From Ref. [30].

supermodules the tracking volume. Each supermodule was composed of Limited Streamer Tubes (LST) as active elements, with double read-out and interleaved by lead layers, and was optimized for the detection of intermediate energy photons direction.

A way of using an $\bar{n}$ beam in the OBELIX detector, with suitable intensity, was suggested by Iazzi [33]. Following the scheme of Fig. 12, the LH_2 production target (PT), was located inside the hollow upstream pole of OAFM, as close as possible (~ 2 m) to the interaction target. The $\bar{p}$'s from LEAR entered PT after being detected by the timing scintillator $T0$, providing the START signal for TOF measurements, and, during their slowing down, a fraction of them underwent a CEX reaction producing $\bar{n}$'s in every direction, with momenta ranging from ~ 40 MeV/c up to a little bit less than the $\bar{p}$ one. The remainder of $\bar{p}$'s annihilated ($\sim 90\%$ at rest) or elastically scattered: in both cases they produced charged particles that could be detected by a surrounding veto-box, except for the annihilation in all neutral channels, whose products were easily distinguished from the $\bar{n}$'s. The $\bar{n}$'s produced in the forward direction (within the opening of a proper lead collimator) reached the Reaction Target (RT) located at the center of the detector and constituted a beam of intensity $\sim 10^2$ s^{-1}. The momentum of each annihilating $\bar{n}$ was measured by TOF.

The $\bar{n}$'s which annihilated in RT (about 25% of the beam), produced at least one charged positive particle ($\sim 96\%\pi, \sim 4\%$K) if the RT was filled with LH_2, while in the case of nuclear Reaction Targets we may assume that the probability of having at least one charged particle is $\geqslant 99\%$. The first charged particle hitting a TOFINO slab gave the STOP signal for TOF allowing the momentum reconstruction of the annihilating $\bar{n}$, by means of an iterative process described in detail, together with all the features of the $\bar{n}$ beam, in Ref. [30].

It must be noted that a disadvantage of such an untagged $\bar{n}$ beam is that the $\bar{n}$ flux must be evaluated from measurements of the $\bar{p}$ flux by means of Monte Carlo simulations, but cannot be directly measured.

Two PT targets (LH_2), 15 and 40 cm long, respectively, were used with incident $\bar{p}$'s of 305 and 412 MeV/c: the targets' length has been chosen a bit larger than the $\bar{p}$ range in order to bring them to rest, preventing the primary beam to reach RT. It is worthwhile to notice that the concept of this $\bar{n}$ beam does not require a LH_2 production target since no tagging and then no precise angular kinematic correlation is needed. A nuclear production target, like CH_2, easier to build and to handle, in which $\bar{p}$'s may be stopped in a reduced thickness (less than 1 cm), could seem to be the best solution, also to simplify the calculations for the momentum reconstruction. But the intensity of such a beam would inevitably be lower than that from a LH_2 target (namely a factor of four for a CH_2 target).

Fig. 13 shows a view of the general layout of OBELIX with the $\bar{n}$ beam. The LH_2 assembly of the reaction target used in many physics measurements described in the following is visible at the

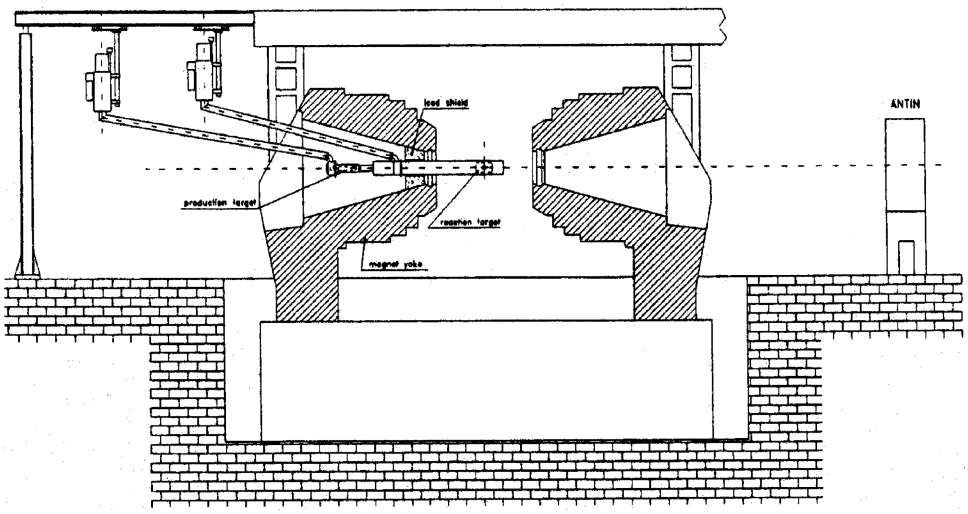

Fig. 13. Scheme of the experimental setup of OBELIX used with $\bar{n}$ beam. From Ref. [30].

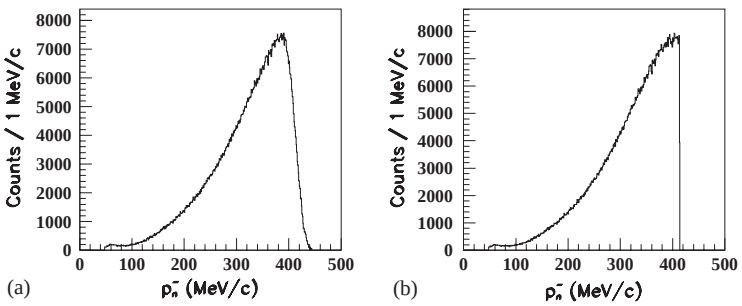

Fig. 14. Experimental momentum spectrum of $\bar{n}$'s produced via CEX reaction in the OBELIX $\bar{n}$ facility: (a) raw spectrum with random coincidences background subtracted; (b) true spectrum after apparatus resolution correction. From Ref. [24].

center of the detector. Since the $\bar{n}$ beam was not tagged, a continuous on-line monitoring of the beam parameters (size, intensity, alignment and energy spectrum) was necessary. To this purpose the prototype of the PS178 $\bar{n}$ detector, called ANTIN and described in Section 2.4, was placed downstream the OBELIX spectrometer and was used as shown in Fig. 13.

Several different beam configurations were used, and we report here only about the one corresponding to the longer data taking. Full details of the different layouts may be found in Ref. [30].

Fig. 14 shows the experimental $\bar{n}$ momentum distribution and the true $\bar{n}$ momentum spectrum, having taken into account the momentum resolution. As described in Section 2.3, the $\bar{n}$'s are produced via CEX by the $\bar{p}$'s slowing down in the LH_2 target following a characteristic spectrum extending from a maximum value (297 MeV/c for 305 MeV/c $\bar{p}$ beam and 406 MeV/c for 412 MeV/c $\bar{p}$ beam) corresponding to the production just at the entrance of the target, down to a minimum value of 50 MeV/c (production at the end of the target, $p_{\bar{p}} = 98$ MeV/c, threshold of the CEX reaction). We could expect also $\bar{n}$'s of lower momenta, corresponding to $\bar{n}$'s emitted backward in the center of

mass system (CM) but boosted forward by the Lorentz transformation. However, taking into account that $d\sigma/d\Omega$ for CEX is forward peaked, and furthermore that the low energy $\bar{n}$'s have a very high probability of being absorbed in the LH_2 target itself, due to the large total cross section for $(\bar{n}p)$ at low momenta, in all the calculations these low energy $\bar{n}$'s were neglected.

Qualitatively, the smooth fall-off at low momenta can be understood in terms of the fast decrease of the $(dE/dz)^{-1}$ function with the decrease of $p_{\bar{p}}$, not compensated by a modest rise of the CEX cross-section close to the threshold.

The $\bar{n}$ spectra were very well reproduced by detailed Monte Carlo calculations, described in Refs. [24,30]. The $\bar{n}$ flux ranged from 13 to 56 $\bar{n}/10^6$ $\bar{p}$. The incertitude on the absolute value of the flux was 7% [24].

The $\bar{n}$ beam was pure. $\bar{p}$'s could not be present since they were stopped in PT. Other particles present in the $\bar{n}$ beam were a few $\pi^{\pm}$ and photons from π^0 decay. These particles were produced in the annihilation at rest of $\bar{p}$'s in PT, transmitted through the lead collimator and not vetoed by the first-level trigger due to inefficiencies of the Veto-Box scintillators. Contamination of the $\bar{n}$ beam of $\sim 5 \times 10^{-3} \pi/\bar{n}$ and $\sim 5 \times 10^{-2}$ photons/$\bar{n}$ were expected. These particles were clearly visible in the minimum-bias on-line raw spectra as a peak separated by ~ 8 ns from the rise of the broad peak corresponding to $\bar{n}$'s. γ's have $\beta = 1$ (and for π's $\beta \sim 1$) so they could be easily eliminated by the second level trigger and in the analysis, since the fastest $\bar{n}$'s have just $\beta \simeq 0.4$.

2.4. Antineutron monitors

$\bar{n}$'s detectors are inevitably of complex structure because of:

(1) the need of a converter in which the $\bar{n}$'s interact (annihilate);
(2) the need of fast counters for the charged annihilation products (usually scintillators) in order to use the TOF technique for the determination of the $\bar{n}$ energy;
(3) the need of a rough but fast charged particle multiplicity selection to distinguish $\bar{n}$'s from other neutral products (neutron, photons).

In addition, these detectors must hopefully provide also the position of the $\bar{n}$'s impact point.

Simple $\bar{n}$'s monitors were used by Brando et al. [19] at the BNL AGS and by Gunderson et al. [20] at the Argonne ZGS and were shortly described in Section 2.1. Their main limitation was that no tracking of the annihilation products was provided. These monitors were then unable to reconstruct the annihilation vertex and had scarce possibilities of reducing the background in the off-line analysis.

The first $\bar{n}$ monitor featuring in a satisfactory way all the above requirements was operated by Bressani et al. [34] at CERN LEAR with the experiment PS178. In a simplified version [35] it was, after the completion of PS178 experiment, used as beam monitor (ANTIN) in the OBELIX experiment. The simplicity of the construction, the low cost as well as the very good performances made this monitor the prototype for larger $\bar{n}$ detection facilities described in Section 2.5.

The detector, described in detail in Ref. [35], is made by 10 equal modules, each of them consisting of (see Fig. 15):

(i) an Iron plate ($96 \times 100 \times 1$ cm^3), as a converter;

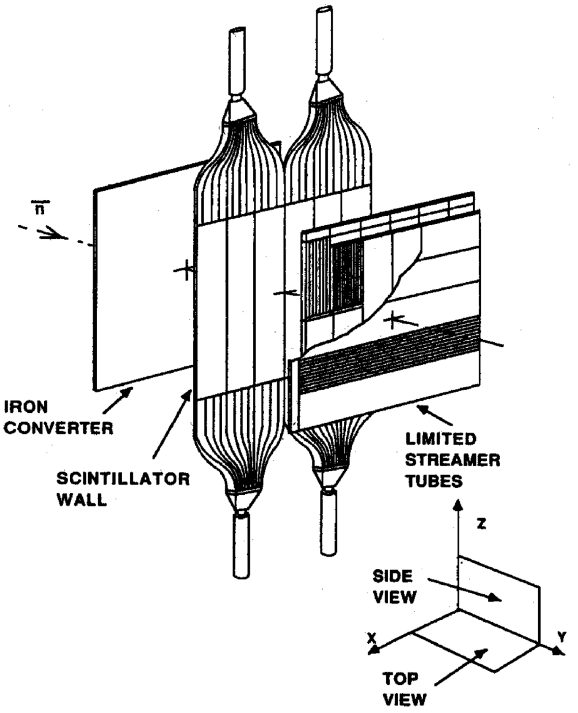

Fig. 15. Pictorial view of one module of the n̄ monitor of the PS 178 experiment. From Ref. [35].

(ii) a plane of two plastic NE110 scintillators ($100 \times 100 \times 1$ cm^3) viewed at both ends by XP2020 PM's, used for trigger and TOF measurements;
(iii) a plane of LST's (surface of 96×100 cm^2) with read-out on both directions, flushed with a Ar(70%)-C_4H_{10}(30%) mixture.

We remind that the main performances of this detector were:

(a) a precision on the annihilation vertex determination of ± 4 cm (FWHM);
(b) a TOF resolution of 800 ps (FWHM);
(c) an efficiency of $\sim 20\%$ for n̄ of 300 MeV/c and of $\sim 60\%$ for n̄ of 100 MeV/c.

Different trigger conditions could be applied and different efficiencies were correspondingly obtained. An n̄ event, as recorded by this monitor, appeared on-line as shown in Fig. 16.

A similar arrangement [28] was used to monitor the n̄ beam of the BNL E-767 Experiment. It consisted of twelve modules, each containing two (x, y) planes of aluminium proportional drift tubes, a four-element scintillator hodoscope (x or y), a 2 cm thick aluminium plate absorber in all but the first three modules. The mass of the first three modules was decreased to allow low energy n̄'s to penetrate further into the detector before annihilating. Each drift tube plane consisted of 48 individual cylindrical tubes 61 cm long and with outer diameter 1.27 cm. The used gas was a 80% argon, 20% CO_2 mixture. The total equivalent aluminium length along the beam direction was about 28 cm.

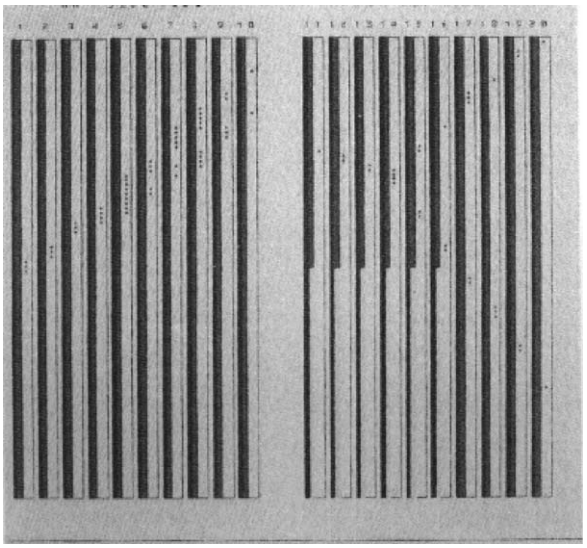

Fig. 16. On-line display of a typical $\bar{n}$ annihilation event, PS178 experiment. From Ref. [35].

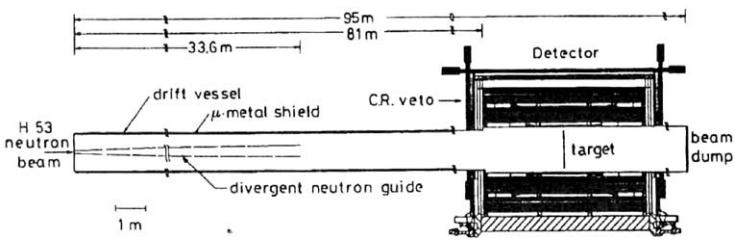

Fig. 17. The $N\bar{N}$ experimental set-up. From Ref. [36].

The 48 scintillator counters had cross-sectional dimensions (15×61) cm^2 and were 1.3 cm thick. The drift tubes provided logical yes/no information on charged particles passing through them. These hits were used to locate an approximate vertex (within ± 5 cm), with a precision limited by the detector granularity and multiple Coulomb scattering. The time resolution, after a quite elaborate software analysis, was 0.45 ns rms. The calculated overall efficiency for $\bar{n}$'s was $(50 \pm 8)\%$.

Finally let us recall that the so-called $N\bar{N}$ experiment, aiming to detect $\bar{n}$–n oscillations, if any, that was performed at the ILL research center at Grenoble [36], may be considered as the larger and more efficient $\bar{n}$ beam monitor operated so far. Here the $\bar{n}$'s possibly generated in a "ultra-cold" neutron beam, of average energy 2×10^{-3} eV, by means of a baryon number non-conserving interaction with $\Delta B = 2$, $\Delta L = 0$ (L being the orbital angular momentum), could be detected by the annihilation in a carbon foil, 130 μm thick and with a diameter of 120 cm, placed in the neutron beam line. The ultra-low energy of $\bar{n}$'s ensured that more than 99% of them would have annihilated. The annihilation products were recorded by large arrays of LST's and scintillators surrounding the carbon converter. Fig. 17 gives a sketch of the lay-out, from which it is possible to appreciate the dimensions.

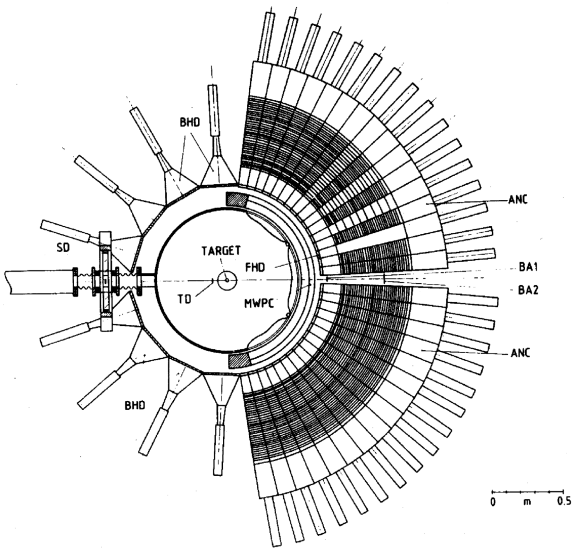

Fig. 18. Experimental set-up (top view) of the experiment by Brückner et al., Ref. [23]. SD and TD are beam defining scintillators, ANC the $\bar{n}$ counters described in the text. MWPC are multiwire proportional counters, FHD and BHD are scintillators hodoscopes used for the simultaneous measurements of the $(\bar{p}p)$ elastic cross section.

Particular care was devoted to the cosmic ray events, that could fake $\bar{n}$ annihilations. Unfortunately this beautiful $\bar{n}$ monitor did not detect any $\bar{n}$, providing the lower limit $\tau_{n\bar{n}} = (0.86 \times 10^8)$ s for the free-space $\bar{n}$–n oscillation time at 90% C.L. in a running time of 2.4×10^7 s.

2.5. Large antineutron detectors

Large arrays of $\bar{n}$ detectors were used in experiments with $\bar{n}$'s in the final state. The first arrangement was used to measure the differential CEX cross section at 390, 490, 590, 690 and 780 MeV/c by Nakamura et al. [25] and the $(\bar{p}, \bar{n})$ reaction on C at 590 MeV/c [37]. The $\bar{n}$'s were detected by 16 modular Iron-scintillator sandwich counters, consisting of seven layers of 1 cm thick scintillator interleaved with Iron plates for a total thickness of 24.8 cm. Each module was viewed by two PMs located above and below it. The efficiency of these modules was estimated as a function of the $\bar{n}$ momentum $p_{\bar{n}}$ as $\varepsilon = 1.67\,p_{\bar{n}}^2 + 1.5\,p_{\bar{n}} + 72.2 \pm 4\%$ (with $p_{\bar{n}}$ in GeV/c); the energy of $\bar{n}$'s was measured by TOF over (3–4) m flight paths.

A similar arrangement, more compact, was used by Brückner et al. [23] to measure the differential cross section for CEX and elastic scattering with $\bar{p}$ at lower momenta. Fig. 18 shows the experimental set-up. The 32 individual $\bar{n}$ counters, labelled ANC in the figure, consisted of 4 mm thick Iron and 6 mm thick scintillator alternated sheets, with a total thickness of 50 cm. Each module had an active area of (6×20) cm^2 at the front face, and was expanded in both height and width to cover a fixed solid angle for the $\bar{n}$'s coming from the target. The scintillators were read-out through wavelength shifter bars, and the achieved time resolution was 1.7 ns FWHM, enough to discriminate between photons and $\bar{n}$'s, due to the short flight path. The efficiency of these detectors was estimated by Monte Carlo calculations to be $(98 \pm 2)\%$.

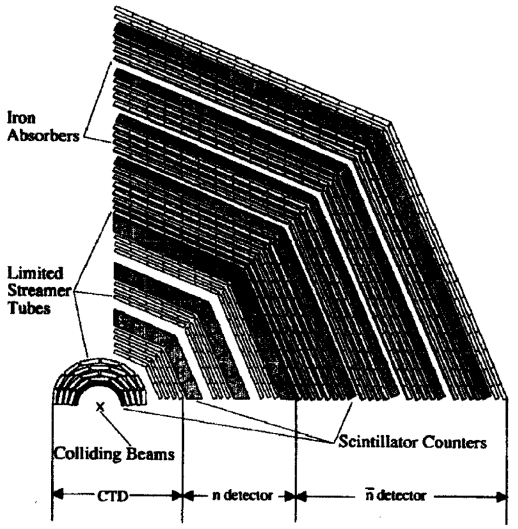

Fig. 19. Detailed view of the FENICE detector showing two contiguous octants. From Ref. [38].

It is worthwhile to mention that the above set-up did not provide a good localization of the n̄ impact point; the angular precision was given by the size of the detectors.

A complex n̄ detector constituted the main part of the non-magnetic FENICE apparatus used at ADONE, Laboratori Nazionali di Frascati [38], to measure the cross-section for $e^+e^- \to n\bar{n}$ from threshold up to 3.1 GeV, to get the neutron Form Factor in the time-like region. The FENICE apparatus was 2.5 m long, 3 m large, with an octagonal cross section and a $(0.76 \times 4\pi)$ sr acceptance. Fig. 19 shows the stratigraphy of two contiguous octants of FENICE.

The structure of the n̄ detector follows that of the PS178 n̄ monitor [35]. The basic module is composed of four interleaving Iron plates, 5 mm thick, as main converter, with four LST layers as tracking detector. A 2 cm thick scintillator counter hodoscope is added for triggering and TOF measurements. The full module is repeated four times and after the last hodoscope two more LST planes are added. Fig. 20 shows how an $e^+e^- \to \bar{n}n$ event, in particular the n̄ annihilation star, appeared in the on-line display of the detector.

Two large area n̄ detectors were the core instruments of the PS199 experiment at CERN LEAR [39]. The aim of the experiment was to measure the differential cross sections, the analyzing power A_{0n} and the spin depolarization parameter D_{0n0n} in the CEX reaction on a polarized target [40,41]. Data were collected at momenta between 608 and 1307 MeV/c for the incident p̄'s. The n̄'s detectors follow again closely the structure of the PS178 n̄ monitor. The cross-section of one of those detectors is represented in Fig. 21. Each detector consists of five modules, each one made of four LST layers with x and y external readout with a 1 cm pitch. The active area of these planes is (202×166) cm^2 (horizontal $\times$ vertical). Each module contains in its middle plane one scintillator counter hodoscope, made by six vertical slabs, 1 cm thick, 33 cm wide and 166 cm long, each viewed by two PMs, for triggering and TOF purposes. Two aluminium walls, 6.3 mm thick, close up each module, which is only 15.5 cm thick. Adjacent modules are separated by 3 cm thick iron slabs: together with the two aluminium walls they constitute the 90% of the detector interaction length.

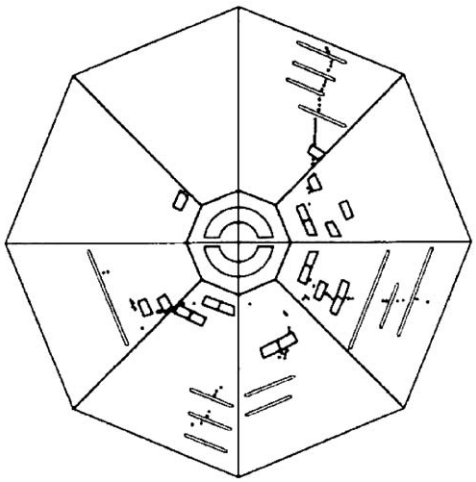

Fig. 20. Display in the transverse plane of a typical $e^+e^- \to \bar{n}n$ event detected by FENICE. Black dots indicate the LST hits while rectangles indicate the fired scintillators. From Ref. [38].

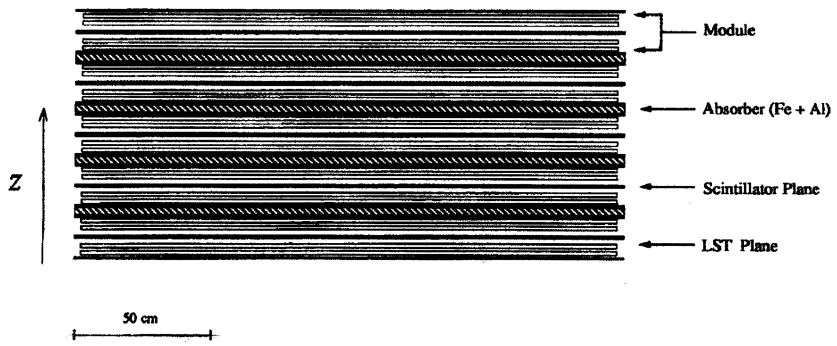

Fig. 21. Cross-section of one $\bar{n}$ detector of the PS199 experiment. From Ref. [39].

Since these detectors were operated in coincidence with neutron detectors of similar area, it was possible to perform a very careful determination of the efficiency. A $\sim$ 16% efficiency, nearly constant from 400 to 1200 MeV/c, was found, with a relative error of 5%. We may notice that the measured efficiency of the PS178 $\bar{n}$ monitor is larger that the PS199 detector one, in spite of the reduced thickness of the Fe converters, owing to the fact that looser triggering conditions to get a recognizable $\bar{n}$ event were be applied in the first experiment.

2.6. Summary of the achievements in antineutron beams and detectors

Following several experimental attempts it was proved that the best method to obtain an $\bar{n}$ beam of good characteristics (flux, beam size, momentum bite) is to use the CEX reaction of $\bar{p}$ on a LH_2 target of suitable length. The $\bar{n}$ beams that may be obtained by this technique can be tagged

by the associated neutron emitted in the CEX reaction or be untagged, in case the $\bar{n}$ is emitted in the forward direction. In case of low momenta beams the most advantageous design is to use a LH_2 target so long as to stop the incident $\bar{p}$ beam, as was done in OBELIX. Typical fluxes for such an arrangement are of the order of $\sim 10^{-4}\bar{n}/\bar{p}$, depending strongly on the acceptances of the defining collimators and/or neutron tagging detectors. The momentum spectra for such $\bar{n}$ beams are continuous, increasing from some tens of MeV/c up to the maximum momentum of $\bar{p}$'s stopped in the target. It is possible to identify unambiguously the momentum of each interacting $\bar{n}$ by means of TOF techniques. The final momentum resolution that may be achieved is around 1%. This feature is very useful to investigate the momentum dependence of a particular interaction channel, since just one beam setting allows a complete measurement, free from systematic errors as it may happen with $\bar{p}$ beams of different (low) momenta.

Concerning the $\bar{n}$ detectors, results from different set-ups have shown that the most reliable accomplishment, first adopted by the PS178 Experiment at LEAR, is a multi-layered modules assembly consisting of a converter (usually Iron), a segmented scintillator wall for triggering on multiplicities of the products from $\bar{n}$ annihilation in the converter, and a plane of localizing devices (LST's, drift tubes, drift chambers). Such $\bar{n}$ detectors provide the following gross performances:

(1) efficiencies ranging from $\sim 15\%$ to better than $\sim 90\%$, depending on the $\bar{n}$ momentum and the number of modules that are used;
(2) time resolutions of less than 1 ns FWHM;
(3) spatial resolution in the annihilation vertex of 1–2 cm.

3. Antineutron–proton cross sections

3.1. General remarks

As already stated, the $(\bar{n}p)$ system is an isospin (I) eigenstate, with $|I, I_3\rangle = |1, +1\rangle$. However, it is not a C-parity eigenstate, so for this system only P (spatial parity), J (total angular momentum) and G-parity are good quantum numbers. The relationships valid for a fermion–antifermion system apply also to $(\bar{n}p)$:

$$P = (-1)^{(L+1)} ,$$

$$G = (-1)^{(L+S+I)} ,$$

L being the relative angular momentum between the antineutron and the proton, and S the spin of the system (which can be 0 or 1). The $I^G(J^P)$ quantum numbers allowed for the lowest initial states (in the notation $^{(2S+1)}L_J$) are the following:

- S-wave

$$^1S_0\text{: } I^G(J^P) = 1^-(0^-) ,$$

$$^3S_1\text{: } I^G(J^P) = 1^+(1^-) ,$$

- P-wave

$$^1\mathrm{P}_1\colon\ I^G(J^P) = 1^+(1^+)\ ,$$

$$^3\mathrm{P}_0\colon\ I^G(J^P) = 1^-(0^+)\ ,$$

$$^3\mathrm{P}_1\colon\ I^G(J^P) = 1^-(1^+)\ ,$$

$$^3\mathrm{P}_2\colon\ I^G(J^P) = 1^-(2^+)\ ,$$

- D-wave

$$^1\mathrm{D}_2\colon\ I^G(J^P) = 1^-(2^-)\ ,$$

$$^3\mathrm{D}_1\colon\ I^G(J^P) = 1^+(1^-)\ ,$$

$$^3\mathrm{D}_2\colon\ I^G(J^P) = 1^+(2^-)\ ,$$

$$^3\mathrm{D}_3\colon\ I^G(J^P) = 1^+(3^-)\ .$$

The P- and G-parities of the final states select the possible initial states from which a definite annihilation channel may proceed. Examples of selection rule applications will be reported in the following sections.

3.2. The antinucleon–nucleon interaction: potential models

The description of the interaction processes occurring in the $\bar{\mathcal{N}}\mathcal{N}$ system may be achieved resorting to two different approaches:

- the use of interaction models, and in particular of potential ones;
- by means of model independent formalisms, based on a cross section expansion in terms of scattering lengths and effective ranges, and extracting these parameters directly from experimental data.

In the following a short overview of the two approaches will be given.

3.2.1. Interaction models

The use of interaction models is required to describe strong interaction phenomena at low energy, like those between nucleons ($\mathcal{N}\mathcal{N}$) or, even more, between nucleons and antinucleons ($\bar{\mathcal{N}}\mathcal{N}$), since in these cases the perturbative approach to QCD cannot be applied, due to the coupling constant divergent behavior.

The simplest statistical approach is not enough to interpret correctly the strong processes involving antinucleons, since in this case, differently from $\mathcal{N}\mathcal{N}$ interactions, all low energy processes are dominated by the annihilation mechanism. Nonetheless, some qualitative features of the $\bar{\mathcal{N}}\mathcal{N}$ annihilation exist that may be reproduced correctly enough. Two of them are the final state multiplicity and the momenta distribution of the produced particles, which have inherently a statistical behavior. The central idea is that, due to $\bar{\mathcal{N}}\mathcal{N}$ annihilation, a *fireball* with definite energy and volume $\Omega = 4\pi R_0^3/3$ is formed. All the final states may be reached through the "decay" of this fireball according to a statistical pattern [42]. To reproduce the experimental value of the mean pionic multiplicity $\langle n_\pi \rangle = 5$

(with standard deviation $\sigma_{n_\pi} = 0.9$ [43]), an annihilation volume Ω of about 100 fm^3 was required in the calculations of Ref. [44], quite too large if compared to the expected reasonable value ~ 1 fm^3. Inserting in the model the possibility that pions may interact inside the volume, forming resonances too, like ρ and ω (as prescribed by the *Statistical Bootstrap Model* [45]), one gets more correct results: a gaussian fit delivers $\langle n_\pi \rangle = 4.61$, with standard deviation $\sigma_{n_\pi} = 0.95$. The annihilation radius is estimated as $R \simeq 1.6$ fm.

The use of phenomenological optical potentials allows a generally correct description of annihilation as well as of several other phenomena connected to $\bar{\mathcal{N}}\mathcal{N}$ interaction, however, again, is not able to reproduce completely the whole experimental scenario. This is mainly due to the fact that the potential formulation used to describe the short range interactions (where annihilation plays the most important role) is not sensitive to the details of the internal dynamics, in particular the interactions between quarks and gluons. Therefore, the predictive power of these models about the probability of definite final states production, and the existence of dynamical selection rules, is rather limited: to this purpose, quark models seem to be more suitable.

The idea at the basis of any optical potential model formulation is to replace a many body problem (the coupling of an $\bar{\mathcal{N}}\mathcal{N}$ system to a many meson final state) by a one-body Schrödinger equation for the $\bar{\mathcal{N}}\mathcal{N}$ wave function

$$(\Delta + p^2 - 2M_N V_{\text{opt}})\psi_{\bar{\mathcal{N}}\mathcal{N}} = 0 \tag{2}$$

where $p = \sqrt{(s - 4m_N^2)/4}$ and a complex potential V_{opt} is introduced, given by a real part $V_{\bar{\mathcal{N}}\mathcal{N}}$ from t-channel meson exchange, a real V_{ann} annihilation potential, and an imaginary absorptive part W:

$$V_{\text{opt}} = V_{\bar{\mathcal{N}}\mathcal{N}} + V_{\text{ann}} + \mathrm{i}W \ . \tag{3}$$

A single channel optical model analysis allows to obtain information on the $\bar{\mathcal{N}}\mathcal{N}$ annihilation cross section, but the details about final state particles dynamics are integrated over. To recover some insight about the individual annihilation channel dynamics the Schrödinger equation (2) must be translated into a system of coupled equations. Many single channel analyses of $\bar{\mathcal{N}}\mathcal{N}$ scattering and annihilation data have been performed, using different formulations for each part of the optical potential. Among many others, it is worthwhile to mention, for their historical relevance, the ones by Bryan and Phillips [46], by Dover and Richard [47], and by Côté et al. [48].

The real part of the optical potential, related to the exchange of mesons in the t-channel, is in general simply derived from the $\mathcal{N}\mathcal{N}$ potential after the application of a G-parity transformation, which turns some of the repulsive components of the $\bar{\mathcal{N}}\mathcal{N}$ system force into attractive (and vice versa), allowing for the possibility of bound states existence:

$$V_{\bar{\mathcal{N}}\mathcal{N}} = \sum_i G_i V_i \ . \tag{4}$$

The sum runs over some i mesons exchanged in the t-channel. Each component V_i may be decomposed, following the usual procedure, into a central (V_0), spin-spin (V_σ), spin-orbit (V_{LS}) and tensor (V_T) components:

$$V_i = \begin{pmatrix} 1 \\ (\vec{\tau}_1 \cdot \vec{\tau}_2) \end{pmatrix} \cdot (V_0 + V_\sigma \sigma_1 \cdot \sigma_2 + V_{LS} \vec{L} \cdot \vec{S} + V_T S_{12}) \tag{5}$$

with $\vec{S} = (\vec{\sigma}_1 + \vec{\sigma}_2)/2$ the total spin, $\vec{L}$ the orbital angular momentum, and S_{12} is the tensor operator defined as $S_{12} = 3(\sigma_1 \cdot \hat{r})(\sigma_2 \cdot \hat{r}) - \vec{\sigma}_1 \cdot \vec{\sigma}_2$. An isospin factor, $(\vec{\tau}_1 \cdot \vec{\tau}_2)$, enters when isovector mesons are exchanged. This description is in general valid for the medium and long-range part of the potential, but below 1 fm the potential well becomes so deep that a description by means of a local, non-relativistic potential looses reliability.

According to the exchanged meson G-parity coherence effects may arise between some components; the sign flip of the odd G-parity exchanged mesons (namely, π, ω and δ) makes the big difference between $V_{\mathcal{N}\mathcal{N}}$ and $V_{\bar{\mathcal{N}}\mathcal{N}}$ concerning the spin and isospin dependence—namely, these contributions become attractive. The $V_{\bar{\mathcal{N}}\mathcal{N}}$ potential is particularly strong and attractive in $I = 0$ channels with $J = L - 1$. This led Dover et al. [47] to foresee the existence of a band of quasi-nuclear bound states coupling to annihilation channels with widths of 100–200 MeV. Some hints at plausible candidates for such states were put forward in the 1990s [49,50], as will be discussed in Section 6. Moreover, the coherence of the isoscalar central and tensor terms could be the main responsible for the excess of total $(\bar{\mathrm{p}}\mathrm{p})$ cross section as compared to $(\bar{\mathrm{n}}\mathrm{p})$ one.

The main difference between various optical potential models versions stands in the formulation of the absorptive part W, which can be local. In the Bryan-Phillips model [46] the annihilation is described by means of a purely imaginary Woods–Saxon potential, which does not depend on spin and isospin (being this dependence embedded in the real meson exchange part of the potential). This model is not compatible with the existence of bound states close to threshold.

The annihilation part of the potential in the Dover–Richard formulation [51] is again given by a Woods–Saxon like expression:

$$V_{\mathrm{ann}} - \mathrm{i}W = \frac{(-V_0 + \mathrm{i}W_0)}{1 + \exp[(r - R)/a]} \tag{6}$$

and is independent on energy, spin and isospin. The best fit parameters are $V_0 \simeq W_0 \simeq 20$ GeV, $a \simeq 0.2$ fm, $R = 0$.

In the model by Côté et al., again Woods–Saxon based, the absorptive part contains explicitly the dependence on energy as well as on spin, isospin and angular momentum. The W potential in this case is composed of a radial, a spin-spin and a spin-orbit part, and has a different shape in isospin singlet and triplet partial waves.

A feature common to all these models is a divergence for ranges smaller than 0.6 fm, which however is not dramatic as, in annihilation reactions, this spatial region is practically black. Beyond 0.7 fm, an energy dependence of W must be included in the Côté et al. model to account for a lower potential intensity. The same behavior in this region is shown by models in which the absorptive part, instead of a Woods–Saxon formulation, is derived by geometrical considerations on quark and antiquark densities overlaps, as in the model by Alberg [52] and by Kohno and Weise [53].

The Côté et al. model foresees as well the possibility of a baryon exchange mechanism, besides the meson exchange one. In spite of the much smaller range parameter for nucleon exchange (about 0.1 fm), the *effective range*, i.e. the distance at which the most of the $\bar{\mathcal{N}}\mathcal{N}$ absorption probability is localized, is consistently about 1 fm for all the potential versions. The baryon potential picture has some problems in the low energy sector, unless proper form factors are introduced. These form factors are arbitrary and have no microscopic explanations, differently to what happens in quark models where they rise up automatically due to the finite extension of meson and baryon bags.

Microscopic (quark) models take into account explicitly the degrees of freedom of the elementary components of the interacting hadrons. They are essentially based on quarks and gluons exchange diagrams, with several topologies and weights depending on the specific features of any different final state. An exhaustive description of all the proposed models is not possible in this Report; the reader is suggested to refer to dedicated reviews on this subject [4,54,55]. Resorting to microscopic models one can get a better description of the different annihilation channels branching ratios as well as of some dynamic selection rules; however up to now a comprehensive explanation of all the experimental results gathered so far is hard to be reached even within this framework.

3.2.2. *Effective range expansion formalisms*

The Effective Range (ER) expansion approach is independent on any hypothesis concerning the interaction potential. It is based on the fit of experimental cross sections, written in terms of proper expansions, with free parameters. A particular application of the method is known as "coupled channel approach", and it was often used to get phenomenological interpretations of annihilation cross sections, as we will see in the following discussing OBELIX data.

The annihilation cross section for two interacting particles may be written by means of a partial waves expansion (in the orbital angular momentum L of the system) in the well-known general form:

$$\sigma_{\text{ann}} = \sum_L \sigma_L^{\text{ann}} = \frac{4\pi}{k^2} \sum_L (2L+1)(\Im m f_L - |f_L|^2) \ , \tag{7}$$

where k is the center-of-mass momentum of the incident particle, and the f_L partial amplitude may be written as a function of the δ_L phase shifts induced by the interaction in the system wave function:

$$f_L = \frac{1}{\cot \delta_L - i} \ . \tag{8}$$

The f_L partial waves may be expanded, in the energy range under study, as a power series in the k variable, following the so-called effective range expansion formalism, for which, in general:

$$k^{2L+1} \cdot \cot \delta_L = \frac{1}{A} + \rho k^2 + O(k^4) \tag{9}$$

where A is the scattering length, and ρ the interaction range. Specializing to S and P partial waves, one gets the two relationships:

$$k \cdot \cot \delta_0 = \frac{1}{a} + \frac{1}{2} r k^2 \ , \tag{10}$$

$$k^3 \cdot \cot \delta_1 = \frac{1}{b} - \frac{3}{2} \frac{1}{R} k^2 \ , \tag{11}$$

in which a and b are, respectively, the scattering length and volume, while r and R are the two effective ranges for the two partial waves. These parameters have to be determined by a phenomenological fit of the annihilation cross section data.

When more interaction channels are simultaneously used in the fits within this framework, the approach is known as coupled channel model [56]. This approach had been used to fit at the same time ($\bar{\text{p}}\text{p}$) cross sections and parameters (namely: total and differential elastic cross sections; total and differential charge exchange cross section; total cross section; protonium strong interaction widths and

energy level shifts; the real-to-imaginary scattering amplitudes ratio) as well as ($\bar{n}p$) cross sections (annihilation and total) up to 300 MeV/c, using the data by Armstrong et al. [28]. It was possible to derive separately the interaction parameters in the two isospin states, $I=0$ and $I=1$. For the $I=1$ source, relevant to the $\bar{n}$ case, it was found, respectively, $a_1=(0.4+0.5i)$ fm and $r_1=(-1.4+1.8i)$ fm for S-wave, and $b_1=(0.8+0.1i)$ fm^3 and $R_1=(0.2-0.4i)$ fm for P-wave.

Following this method, a new analysis was performed including OBELIX data up to 400 MeV/c [57]. Details will be given in Section 3.4.

3.3. Total cross section

Even though the total cross section σ_T is the first, straightforward piece of information on the interaction between two particles, often it is not the easiest one to extract experimentally. This is the case for $\sigma_T(\bar{n}p)$ in the low momentum region ($p_{\bar{n}} \leqslant 500$ MeV/c). After first trials mentioned in Section 2.1, the first systematic measurement was performed by Armstrong et al. [28] in the E-767 Experiment at BNL, with the set-up shown in Fig. 9. The measurements were performed by the transmission method, alternating runs with empty and full LH_2 target. Owing to the dimensions of the transmission target (a cylinder 35 cm long and with 40 cm diameter), quite important correction factors had to be applied to the raw data, evaluated through accurate simulation programs. A preliminary analysis of the data was performed to search for narrow states below 1900 MeV in the ($n\bar{p}$) system, predicted to appear frequently in potential model calculations [49,50,58–60]. No statistically significant structures were found [61].

The final values of σ_T, published in Ref. [28], are reported in Fig. 22. The data could be well fitted to a simple parametrization $\sigma_T = A + B/p$, with an excellent fit (χ^2/d.o.f. $= 29/38$) with $A=(94.4\pm 9.0)$ mb and $B=(36.0\pm 2.9)$ mb $\cdot$ GeV/c.

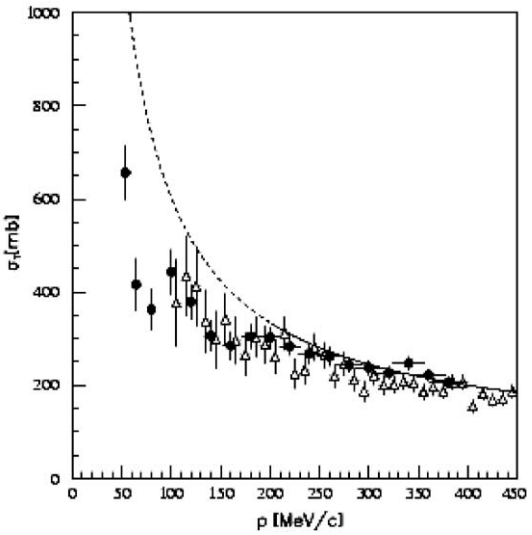

Fig. 22. Comparison of $\bar{\mathcal{N}}\mathcal{N}$ total cross section at low momenta. The black circles for ($\bar{n}p$) are from Ref. [62], the open triangles for ($\bar{n}p$) from Ref. [28]; the solid curve represents the fit of Bugg et al. to the ($\bar{p}p$) data [63]. The dashed part represents the extrapolation to lower momenta. From Ref. [62].

A different technique was adopted by the OBELIX Collaboration, thanks to the fact that in long data taking runs, the LH_2 *RT* was always full, for exclusive two-body annihilations and meson spectroscopy studies with $\bar{n}$'s. The method, described in Refs. [62,64,65], is based essentially on a thick target/narrow beam transmission technique. In *RT* a fraction of the $\bar{n}$ beam (from $\sim 15\%$ to $\sim 25\%$, depending on the momentum $p_{\bar{n}}$) annihilates. By reconstructing the annihilation vertices it is possible to determine the number $\Delta N_{\mathrm{ann}}(p_{\bar{n}}, z)$ of $\bar{n}$'s of a given momentum $p_{\bar{n}}$, annihilating in the interval $(z, z+\Delta z)$, at a depth z in the target:

$$\Delta N_{\mathrm{ann}}(p_{\bar{n}}, z) = \sigma_{\mathrm{ann}}(p_{\bar{n}}) I_{\bar{n}}(p_{\bar{n}}, z) \rho \mathcal{N}_A \Delta z \ , \tag{12}$$

where $\sigma_{\mathrm{ann}}(p_{\bar{n}})$ is the $(\bar{n}p)$ annihilation cross section at $p_{\bar{n}}$, $I_{\bar{n}}(p_{\bar{n}})$ the flux of the $\bar{n}$'s of momentum $p_{\bar{n}}$ at the depth z, ρ the density of LH_2 and $\mathcal{N}_A$ the Avogadro's number. $I_{\bar{n}}(p_{\bar{n}})$ is given by

$$I_{\bar{n}}(p_{\bar{n}}, z) = I_{\bar{n}}(p_{\bar{n}}, 0) \exp(-\sigma_T \rho \mathcal{N}_A z) \ , \tag{13}$$

where $I_{\bar{n}}(p_{\bar{n}}, 0)$ is the flux of $\bar{n}$ of momentum $p_{\bar{n}}$ at the entrance of the LH_2 target. Then

$$\frac{\Delta N_{\mathrm{ann}}(p_{\bar{n}}, z)}{\Delta z} = I_{\bar{n}}(p_{\bar{n}}, 0) \sigma_{\mathrm{ann}}(p_{\bar{n}}) \rho \mathcal{N}_A \exp(-\sigma_T \rho \mathcal{N}_A z). \tag{14}$$

From Eq. (14) it is clear that σ_T is simply deduced by the exponential slope of $\Delta N_{\mathrm{ann}}(p_{\bar{n}}, z)/\Delta z$.

The data from OBELIX are compared with those by Armstrong et al. [28] in Fig. 22. For a coherent comparison the statistical and systematic errors of both experiments were added in quadrature. The agreement between the two sets of data, in the region in which they overlap, is satisfactory. For comparison, $\sigma_T(\bar{p}p)$, represented by the best fit of the measurement of Bugg et al. [63], is also reported in the figure. $\sigma_T(\bar{p}p)$ seems to become slightly higher than $\sigma_T(\bar{n}p)$ at the lower momenta ($\simeq 200$ MeV/c). Below 100 MeV/c, the OBELIX data show a quite anomalous trend, suggesting a dip around 80 MeV/c. The statistical significance for both the two points at 64.5 and 80 MeV/c, that deviate from a smooth rise from 100 down to 54 MeV/c, is $\sim 3.5\sigma$. We will discuss this point in more detail in Sections 3.4 and 3.5.

By defining R as the ratio $\sigma(\bar{p}p)/\sigma(\bar{n}p)$, it is straightforward to see that

$$R = \frac{\sigma_T(I=0) + \sigma_T(I=1)}{2\sigma_T(I=1)} \tag{15}$$

in which $\sigma_T(I=0)$ and $\sigma_T(I=1)$ are the total cross sections related to the $I=0$ and $I=1$ components of the $\bar{\mathcal{N}}\mathcal{N}$ interaction.

A strong dominance of the $I=0$ component at low momenta is observed. In fact, the ratio $\sigma_T(I=0)/\sigma_T(I=1)$ at 70 MeV/c is (2.5 ± 0.4), to be compared to (1.1 ± 0.1) at 300 MeV/c. Following Dover et al. [4] this effect could be a manifestation of the coherence of ρ, ω, δ and σ meson exchange in the central and tensor terms of the $\bar{\mathcal{N}}\mathcal{N}$ medium range force. An indirect indication of such an effect following measurements in light nuclei was reported earlier in Ref. [66].

3.4. Annihilation cross section

We remind here that, besides the counter experiments mentioned in the previous sections, in the late Seventies the Bombay-CERN-Neuchâtel-Tokyo Collaboration (and the following ones), using the 81 cm Saclay Hydrogen filled bubble chamber [67–69], was able to collect a sample of $(\bar{n}p)$ interactions that produced first interesting results.

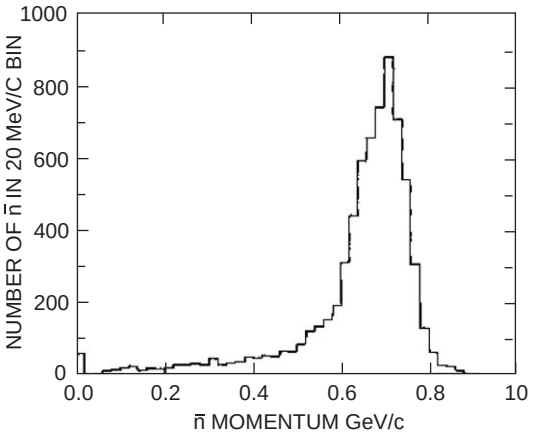

Fig. 23. n̄ momentum distribution in the lab. frame, data collected by the 81 cm Saclay bubble chamber, from Ref. [68].

Even in this case the CEX reaction was exploited to produce n̄'s from the incoming p̄ beam. In the hydrogen bubble chamber the n̄ annihilation reactions were identified by the observation of an annihilation star at most one centimeter away from the point where the CEX reaction occurred, that is where the p̄ track disappeared. In a first run the p̄ momentum could vary in the range 700–760 MeV/c [67]; about 3500 events could be collected with the required topology. Later on, two beam momenta had been fixed, namely 700 and 760 MeV/c, and an about three times larger statistics could be collected [68,69]. In this case the n̄ momentum could vary continuously from the minimum value up to about 800 MeV/c. Fig. 23 shows the n̄ momentum distribution in the laboratory frame for the selected events; the analyses had been performed over the restricted n̄ momentum range 500–800 MeV/c. The measurement error on the p̄ beam momentum was typically about 25 MeV/c, and this was the main source of uncertainty over the n̄ momentum evaluation. The energy resolution in the ($\bar{n}p$) system after the kinematic fit selections was about 2 MeV. These data are complementary to those by the E-767 and OBELIX Collaborations.

In spite of the limited statistics, first surveys on annihilation multiplicities, pion production dynamics and resonances production in the s-channel (which will be treated in the following sections) could already be performed with the bubble chamber data. Inclusive and exclusive multipionic final states were studied and first cross-section evaluations were made, over the full solid angle (for both the CEX and the ($\bar{n}p$) annihilation reaction) thanks to the complete angular coverage of the bubble chamber device.

$\sigma_{ann}(\bar{n}p)$, integrated over the (500−800) MeV/c momentum range, was found to be (55.4±2.2) mb, to be compared to (77.9±0.6) mb for $\sigma_{ann}(\bar{p}p)$, measured in the same experiment. The dominance of the $I=0$ source over the $I=1$ one is apparent also from these data ($R=1.41$), $\sigma_{ann}(I=0)/\sigma_{ann}(I=1)$ being 1.82.

A determination of $\sigma_{ann}(\bar{n}p)$ in the (100–500) MeV/c momentum range was reported by Armstrong et al. [28] in the E-767 Experiment at BNL. Also for $\sigma_{ann}(\bar{n}p)$ a preliminary analysis aiming at the search for narrow states was performed, with negative results [61]. In the final analysis [28] $\sigma_{ann}(\bar{n}p)$ was not determined in a way independent from $\sigma_T(\bar{n}p)$, but it was evaluated subtracting from the latter a parametrization of the elastic scattering cross section $\sigma_{el}(\bar{n}p)$. The data could be fitted well

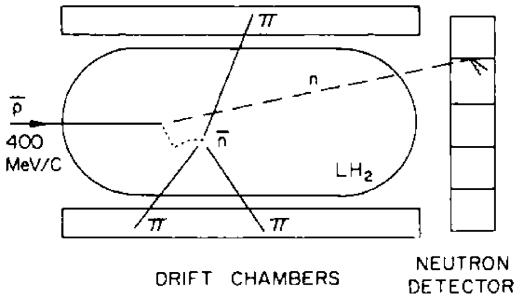

Fig. 24. Schematic diagram of the experiment of Ref. [70]. The 400 MeV/c $\bar{p}$ charge-exchanges in the liquid Hydrogen target. The forward-going neutron is produced at back angles (c.m.) and scatters in the LH_2 until it annihilates. The annihilation products are detected in the vertex detector (drift chambers). From Ref. [70].

(χ^2/d.o.f. $= 29/38$) with the usual $\sigma_{ann} = A + B/p_{\bar{n}}$ parametrization, with $A = (41.4 \pm 9.0)$ mb and $B = (29.0 \pm 2.9)$ mb $\cdot$ GeV/c.

By a clever modification of the E-767 set-up (replacing the $\bar{n}$ calorimeter with a neutron hodoscope and allowing the $\bar{p}$'s to stop in the LH_2 target, taking out the target assembly T, see Fig. 9 for reference), Mutchler et al. were able to measure $\sigma_{ann}(\bar{n}p)$ down to very low momenta [70]. The basic concept of the experiment (E-795) is illustrated in Fig. 24.

A low energy $\bar{n}$ is produced in the large LH_2 target by CEX reaction. Reminding the kinematics of Fig. 4, a fast forward neutron signals the creation of a low-energy $\bar{n}$. If the angle and momentum of the neutron are measured, the energy of the incident $\bar{p}$ and the created $\bar{n}$ can be calculated. The low-energy $\bar{n}$ then scatters in the LH_2 target until it annihilates or escapes.

The survival time of the $\bar{n}$'s depends on $\sigma_{ann}(\bar{n}p)$ at low energy. If only S-waves are present the cross-section is proportional to β^{-1} (β being the $\bar{n}$ velocity) and $\beta\sigma_{ann}(\bar{n}p)$ approaches a constant as $\beta \to 0$. In an infinite LH_2 target, $\beta\sigma_{ann}(\bar{n}p)$ would be inversely proportional to the measured survival time τ:

$$\tau = \frac{790 \text{ mb} \cdot \text{ns}}{\beta\sigma_{ann}(\bar{n}p)} \ . \tag{16}$$

The method, reminiscent of the Fermi-age measurements [71,72], could be applied only after huge corrections by accurate simulations. The final values reported by the Authors are $\beta\sigma_{ann}(\bar{n}p) = (40 \pm 3)$ mb at 22 MeV/c and (32 ± 5) mb at 43 MeV/c. The extrapolation at $\beta \to 0$ provided a determination of the imaginary part of the $I = 1$ spin-averaged S-wave scattering length, $a_1 = (-0.83 \pm 0.07)$ fm.

Very precise measurements of $\sigma_{ann}(\bar{n}p)$ in the momentum range (50–400) MeV/c were produced by OBELIX [57]. Efficiencies and acceptances were well known and determined by means of many Monte Carlo simulations, specific measurements, calibrations with well-measured annihilation reactions. Statistics were plentiful for a measurement as simple as $\sigma_{ann}(\bar{n}p)$, inclusive over all channels. The values by OBELIX, reported in Fig. 25, were well in agreement with the previous ones by Armstrong et al. [28], affected by 15–20% errors, not reported in the picture for simplicity. The only drawback in the OBELIX $\sigma_{ann}(\bar{n}p)$ data was an overall normalization error of about 7%, due to the $\bar{n}$ beam counting method. It must also be stressed that the method by which $\sigma_{ann}(\bar{n}p)$ was

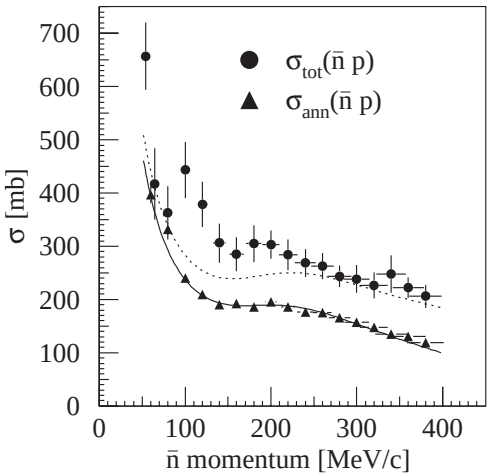

Fig. 25. Experimental value of the total (Ref. [62], black triangles) and annihilation (Ref. [57], black circles) ($\bar{n}p$) cross sections. The solid curve represents the calculation of $\sigma_{ann}(\bar{n}p)$ performed in Ref. [57], the dotted one the calculation of $\sigma_T(\bar{n}p)$ by using the same parametrization.

evaluated is completely independent from the one used for $\sigma_T(\bar{n}p)$, in contrast with the method adopted by Armstrong et al.

$\sigma_{ann}(\bar{p}n)$, which should be in principle equal to $\sigma_{ann}(\bar{n}p)$, was reported by Kalogeropoulos and Tzanakos [73] from a deuterium bubble chamber experiment in the momentum range 250–450 MeV/c. The data are also not reported in Fig. 25 since they agree within errors ($\sim 10\%$) with the corresponding data by OBELIX.

The measured $\sigma_{ann}(\bar{n}p)$ up to 300 MeV/c was very well reproduced by a fit by means of an ER expansion technique starting from the values of Ref. [56] and considering S- and P-waves only. The final values giving the best reduced χ^2 value ($\chi^2/\text{n.d.f} = 7.6/5$) were only slightly different from the starting ones. The fit with S- and P-waves only worsened clearly when $\sigma_{ann}(\bar{n}p)$ measurements up to 400 MeV/c ($\chi^2/\text{n.d.f.} = 49/9$) were included. Adding to Eq. (7) the D-wave contribution with

$$k^5 \cot \delta_2 = \frac{1}{c_1} + \frac{5}{2}\frac{1}{\rho_1^3} k^2 \ , \tag{17}$$

a clear improvement in the fit was however obtained, as shown in Fig. 26, with a $\chi^2/\text{n.d.f.} = 9.5/5$. The fitted values for c_1 and ρ_1 were respectively $c_1 = (0.086 + \text{i}0.019)$ fm^5 and $\rho_1 = (-2.17 + \text{i}2.6)$ fm. The D-wave contribution at 400 MeV/c was about 10%. This result was used for an evaluation of the D-wave percentage in the $\bar{n}$ momentum range between 250 and 400 MeV/c, obtaining a value $\alpha_D = (4.7 \pm 0.6)\%$ [57].

The other parametrizations and models [48,51,74,75] trying to reproduce $\sigma_{ann}(\bar{n}p)$ gave worse results. Moreover, the use of the parameters by Ref. [57] for the description of $\sigma_T(\bar{n}p)$ gave a result not satisfactory at all ($\chi^2/\text{d.o.f.} = 6.1$), as shown by Fig. 25. The agreement was even worse if the two data points at 64.5 and 80 MeV/c were removed from the analysis, under the hypothesis that they might be wrong for some unknown reason: the $\chi^2/\text{d.o.f.}$ increased to 10.6.

Several trials to fit the $\sigma_T(\bar{n}p)$ data adopting different truncations of the ER expansions were performed and in all cases parameters providing satisfactory fits were found ($\chi^2/\text{d.o.f.} \simeq 1.0$–$1.4$).

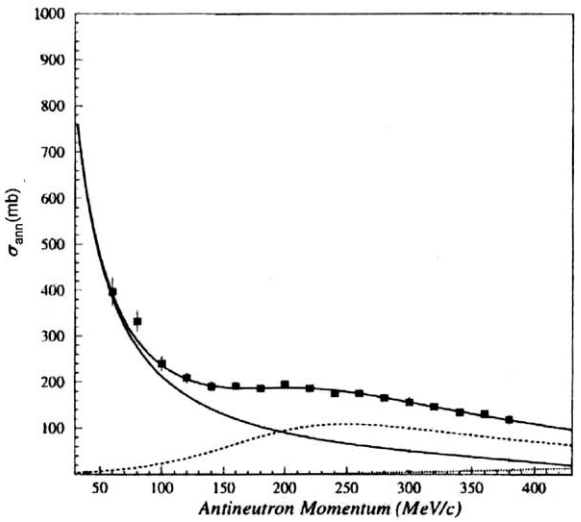

Fig. 26. Fit of $\sigma_{ann}(\bar{n}p)$ measured by OBELIX up to 400 MeV/c including S- (solid line), P- (broken line) and D- (point line) wave contribution. From Ref. [57].

On the other hand such parameters could not reproduce at all $\sigma_{ann}(\bar{n}p)$. Therefore it seems impossible to find a set of parameters able to describe correctly at the same time both $\sigma_T(\bar{n}p)$ and $\sigma_{ann}(\bar{n}p)$. The reason is that the elastic cross section $\sigma_{el}(\bar{n}p) = \sigma_T(\bar{n}p) - \sigma_{ann}(\bar{n}p)$ exhibits an unexpected trend, as will be discussed in the next subsection.

$\sigma_{ann}(\bar{n}p)$ is always lower than $\sigma_{ann}(\bar{p}p)$, like σ_T. The ratio R, previously defined in Eq. (15), becomes (1.76 ± 0.11) at 70 MeV/c, considering the value for $\sigma_{ann}(\bar{p}p)$ quoted by Zenoni et al. [76], corresponding to (2.5 ± 0.4) for the ratio $\sigma_{ann}(I = 0)/\sigma_{ann}(I = 1)$.

In conclusion, $\sigma(I = 1)$ (be it σ_{ann} or σ_T), is always lower, even by a factor of 2.5, than $\sigma(I = 0)$. However, looking at the experimental data, the trend of R is not regular. At ~ 700 MeV/c it is about 1.5, in the region (300–500) MeV/c it approaches 1, at lower momenta it is about 1.7. Whether this behavior is due to a physical effect, or simply the manifestation of some inconsistencies among different experiments, is a matter for future experiments to ascertain.

3.5. Elastic cross section and subnuclear Ramsauer-like effect

Fig. 27 shows the behavior of $\sigma_{el}(\bar{n}p)$. A dip at low momenta is observed. The two points at 64.5 and 80 MeV/c are closer to the lower bound imposed by the unitarity constraints for S-wave [77]:

$$\sigma_{el} \geqslant \frac{k^2}{4\pi}\sigma_T^2 \tag{18}$$

where k is the c.m. $\bar{n}$ momentum.

The vanishing of the elastic cross section is a quite rare, although possible, situation, whose most known manifestation is the Ramsauer–Townsend effect [78] for the low energy electron scattering off atoms.

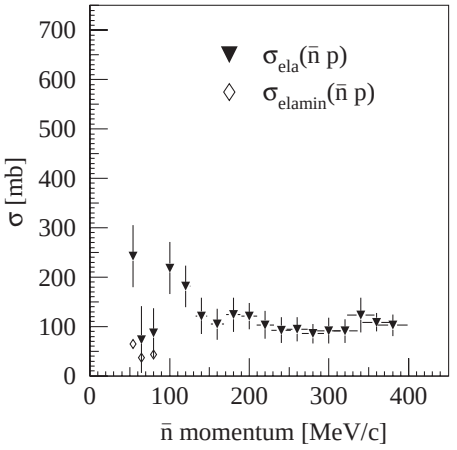

Fig. 27. Black triangles: elastic cross section as a function of $p_{\bar{n}}$ obtained from the difference between the total (Ref. [62]) and annihilation (Ref. [57]) cross sections. Diamonds: lower limits of the elastic cross sections due to the unitarity constraints. From Ref. [62].

The explanation of the Ramsauer–Townsend effect is a textbook, historical application of quantum mechanics, in terms of interference between incident and scattered electron waves. A nice description of the theoretical approach can be found in the classical book of Mott and Massey [79]. It is less known that a similar effect is observed for neutron interaction with nuclei, where broad minima and maxima are observed in total cross sections as a function of the neutron energy, whereas inelastic cross sections are flat.

Peterson [80] interpreted this behavior in terms of a nuclear Ramsauer effect and this very simple approach can be applied to the description of $\sigma_{el}(\bar{n}p)$ [81]. The $\bar{n}$ wave, that outside a proton is characterized by the wave number k_{out}, is incident on a proton represented by a square potential well of depth V_0 and radius R. Interference between the part of the wave which has passed through the proton, whose wave number becomes k_{in}, and the part which has gone round it causes oscillations in the elastic cross section. The average phase difference between the wave traversing the proton and the one getting around is

$$\Delta = \frac{4}{3}\alpha(k_{in} - k_{out})R \ , \tag{19}$$

where α is a number larger than 1 (typically 1.5) allowing for the increased path length inside the proton due to refraction effects. The condition for minimum cross section is maximum constructive interference between the two wave components, i.e.

$$\Delta = \frac{4}{3}\alpha(k_{in} - k_{out})R = 2\pi \ . \tag{20}$$

Using Eq. (20) in order to find the values of the real potential well parameters, V_0 and R, that correspond to the minimum cross section, which is located at ~ 70 MeV/c (see Fig. 27), one can find, e.g., $V_0 = 70$ MeV and $R = 2$ fm, or $V_0 = 80$ MeV and $R = 1.9$ fm.

It is quite instructive to compare these values with those of more complete analyses of the $\bar{\mathcal{N}}\mathcal{N}$ elastic scattering, in particular ($\bar{\mathrm{p}}\mathrm{p}$). In Ref. [82] a typical solution fitting the elastic scattering data from 180 to 600 MeV/c was obtained with a real part of the optical potential represented by a Wood–Saxon well with $V_0 = (46.0 \pm 8.0)$ MeV, $R = 1.89$ fm and diffuseness 0.2 fm. The values found from analyses of the ($\bar{\mathrm{p}}\mathrm{p}$) system (mixture of $I = 1$ and $I = 0$ amplitudes) cannot be directly used in the analyses of the ($\bar{\mathrm{n}}\mathrm{p}$) system (pure $I = 1$), since we have seen that the amplitudes for the two isospin components become very different (more than a factor 2) at momenta below 100 MeV/c.

Thus, the values provided for the proton potential well by the naive application of the expression deduced from the Ramsauer description of the phenomenon are not contradicting those found in more complete and sophisticated analyses.

3.6. Summary of antineutron–proton cross sections

At present the data bank for ($\bar{\mathrm{n}}\mathrm{p}$) cross section in the low momentum region, where S- and P-waves only are present, is more complete than the corresponding one for ($\bar{\mathrm{p}}\mathrm{p}$). There are several data for $\sigma_T(\bar{\mathrm{p}}\mathrm{p})$, $\sigma_{\mathrm{ann}}(\bar{\mathrm{p}}\mathrm{p})$ [63], and $\sigma_{\mathrm{el}}(\bar{\mathrm{p}}\mathrm{p})$ [83] over 200 MeV/c but only a set, not complete, for σ_{ann} below 200 MeV/c [76], whereas for ($\bar{\mathrm{n}}\mathrm{p}$) there are the sets of data presented in the previous Section, the most complete and accurate of which belong to OBELIX. This situation is determined by experimental reasons already discussed: $\bar{\mathrm{n}}$'s can penetrate consistent amounts of LH_2 without suffering from energy loss, as it happens with $\bar{\mathrm{p}}$'s. Therefore the counting rates from thick targets are quite large for $\bar{\mathrm{n}}$ and overcompensate the effect of the low flux of incident $\bar{\mathrm{n}}$'s.

$\sigma_T(\bar{\mathrm{p}}\mathrm{p})$ and $\sigma_{\mathrm{ann}}(\bar{\mathrm{p}}\mathrm{p})$ are always larger than $\sigma_T(\bar{\mathrm{n}}\mathrm{p})$ and $\sigma_{\mathrm{ann}}(\bar{\mathrm{n}}\mathrm{p})$ at the same beam momentum. The magnitude of the effect, quite small at ~ 300 MeV/c, increases strongly going down to the lower momenta, indicating that the $I = 0$ source of the $\bar{\mathcal{N}}\mathcal{N}$ interaction is stronger than the $I = 1$ one. This effect could be a manifestation of the coherence of ρ, ω, δ and σ meson exchange in the central and tensor terms of the $\bar{\mathcal{N}}\mathcal{N}$ medium range force. A similar behavior for $\sigma_{\mathrm{ann}}(\bar{\mathrm{n}}\mathrm{p})$ ($\sigma_T(\bar{\mathrm{n}}\mathrm{p})$ is not measured) is apparent also in the 500–800 MeV/c range.

There is a 3.5σ statistical evidence for a dip around 80 MeV/c in $\sigma_T(\bar{\mathrm{n}}\mathrm{p})$, due to a dip in $\sigma_{\mathrm{el}}(\bar{\mathrm{n}}\mathrm{p}) = \sigma_T(\bar{\mathrm{n}}\mathrm{p}) - \sigma_{\mathrm{ann}}(\bar{\mathrm{n}}\mathrm{p})$, since $\sigma_{\mathrm{ann}}(\bar{\mathrm{n}}\mathrm{p})$ is structureless. The phenomenon can be interpreted as a subnuclear Ramsauer-like effect.

4. Antineutron annihilations into multipionic channels

Two experiments only were able to collect good enough statistics to perform final states selections and evaluate annihilation cross sections into specific channels, both inclusive and exclusive: the already mentioned bubble chamber experiment by Banerjee et al. [67–69] and OBELIX. The bubble chamber experiment studied several annihilation features, like, for instance, the annihilation multiplicities and the reaction topologies, and provided the annihilation cross sections for several channels in the (500–800) MeV/c $\bar{\mathrm{n}}$ momentum range [68,69].

They are reported in the second column of Table 1. The average multiplicity of charged particles the Authors quote is (3.24 ± 0.16).

According to the bubble chamber experiment at high $p_{\bar{\mathrm{n}}}$ the topological branching fractions of odd prong ($\bar{\mathrm{n}}\mathrm{p}$) annihilations are in agreement, within errors, with the same branching fractions for ($\bar{\mathrm{p}}\mathrm{n}$)

Table 1
Inclusive and exclusive cross sections for multipionic final states measured by OBELIX in the momentum range ($\sim$ 50–405) MeV/c, and by bubble chamber (Ref. [68]) in the momentum range (500–800) MeV/c

Final state	Cross section (mb) $\sim 50 \leqslant p_{\bar{n}} \leqslant 405$ MeV/c	Cross section (mb) $500 \leqslant p_{\bar{n}} \leqslant 800$ MeV/c
$\bar{n}p \to \pi^+ X$		7.7 ± 0.5
$\bar{n}p \to \pi^+\pi^0$	0.19 ± 0.06	0.16 ± 0.05
$\bar{n}p \to 2\pi^+\pi^- X$	78.5 ± 7.0	33.7 ± 1.5
$\bar{n}p \to 2\pi^+\pi^-$	3.82 ± 0.304	1.16 ± 0.16
$\bar{n}p \to 2\pi^+\pi^-\pi^0$	36.37 ± 3.30	10.15 ± 0.51
$\bar{n}p \to 2\pi^+\pi^- 2\pi^0$	20.67 ± 1.86	
$\bar{n}p \to 3\pi^+ 2\pi^- X$		13.4 ± 0.7
$\bar{n}p \to 3\pi^+ 2\pi^-$	10.52 ± 0.59	2.41 ± 0.18
$\bar{n}p \to 3\pi^+ 2\pi^-\pi^0$		4.86 ± 0.31
$\bar{n}p \to 4\pi^+ 3\pi^- X$		0.6 ± 0.1
$\bar{n}p \to 4\pi^+ 3\pi^-$		0.31 ± 0.08
$\bar{n}p \to 4\pi^+ 3\pi^-\pi^0$		0.05 ± 0.02

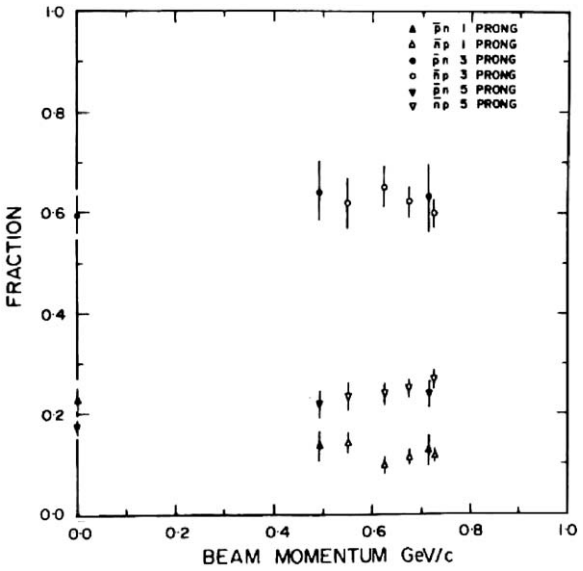

Fig. 28. Fractional branching ratios of different topologies in ($\bar{n}p$) and ($\bar{p}n$) annihilations, from Ref. [68].

annihilations in the same beam momentum range [84], as shown in Fig. 28. This means essentially that, at these energies, the annihilation mechanism must be similar for the two reactions. These values are in agreement as well with the predictions by the Orfanidis–Rittenberg statistical model

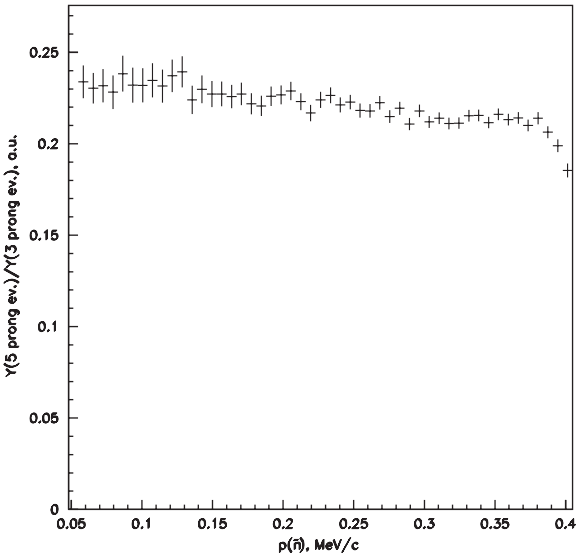

Fig. 29. Ratio between n̄ momentum distributions for inclusive five- and three-prong events (not corrected for apparatus acceptance and efficiencies), OBELIX data.

[85]. The absolute fraction of inclusive annihilations into five prongs is about 20%, while for three prongs it is around 60%, and both of them are practically independent on the projectile momentum.

It was moreover observed that, in general, the annihilation reaction topology is compatible with a central emission, in an analysis of the Feynman x distributions for inclusively emitted negative and positive pions, which have similar shapes [68]. This observation is in agreement with the temperatures which can be assigned to the Maxwell-Boltzmann distribution fitting the (non-invariant) cross section $f(E) = \int \mathrm{d}\sigma/\mathrm{d}^3 p\, \mathrm{d}\Omega$ plotted as a function of the inclusively emitted pion energy, which is in the range (105–110) MeV, typical value for central emission in hadronic collisions.

At lower energies, with $p_{\bar{\mathrm{n}}}$ from $\sim$ 50 to 405 MeV/c, some evaluations of cross-sections were performed by OBELIX in some selected channels; they are reported in the first column of Table 1. The topological branching fractions for the events collected by OBELIX are reported in Figs. 29 and 30. In the first one the ratio between the momentum distributions for five- over three-prong (inclusive) events is plotted. The trend decreases smoothly with the n̄ momentum, without any evident deformation that could hint at the existence of dynamic effects in formation. More details about this subject will be given in Section 6.6. The relative ratio between the yields, $Y_{5\pi}/Y_{3\pi} =$ (0.2–0.25), is roughly in agreement with the bubble chamber branching ratios evaluations reported above, $\sim$ 30%.

In Fig. 30a the ratios between the momentum distributions for exclusive five- over three-pion events is shown, while Fig. 30b shows the ratio for six- over four-pion ones. In both the cases, for $p_{\bar{\mathrm{n}}} > 100$ MeV/c, again a smooth behavior can be observed; this means that the production final states with an odd (or even) number of pions follows the same pattern. The region below 100 MeV/c, on the other hand, is more critical due to the reduced flux of n̄'s at low momenta. Deviations from a smooth trend in this region are most likely due to statistical fluctuations.

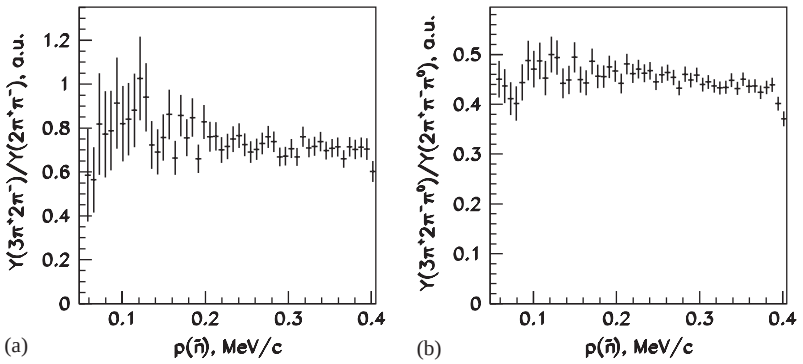

Fig. 30. Ratios between $\bar{n}$ momentum distributions for exclusive pions: (a) odd pions ($3\pi^+2\pi^-/2\pi^+\pi^-$), (b) even pions ($3\pi^+2\pi^-\pi^0/2\pi^+\pi^-\pi^0$), OBELIX data.

5. Two-body antineutron annihilation reactions

Apart from the issues by OBELIX [86–88] no other result exist in literature about the production cross sections and annihilation frequencies in specific $\bar{n}p \rightarrow$ two-body channels. These measurements allow to investigate the annihilation dynamics from a pure $I = 1$ initial state, as well as the contribution of the single partial waves in different annihilation channels. Of particular interest are the annihilation channels in which open and hidden strangeness mesons are produced, since in this case some information about the sea-quark content of the hadrons involved in the interaction may be inferred.

In two-body annihilation channels the quantum numbers selection rules summarized in Section 3.1 may be applied straightforwardly, therefore a direct test of the production of each channel from the allowed initial states may be performed. Once the extent of the production from each allowed partial wave is known, information about the hadronic branching ratios may be obtained.

As long as the $\bar{n}$ momentum is sufficiently low, S and P-waves only can be considered. In general, the partial waves with $L > 0$ contribute to the $\bar{\mathcal{N}}\mathcal{N}$ annihilation at lower momenta as compared to $\mathcal{N}\mathcal{N}$ interactions [89], an explanation being given by the occurrence of attractive components of the potential as described in Section 3.2. However, with $\bar{n}$'s of momenta up to 400 MeV/c, the integrated contribution of D-wave in ($\bar{n}p$) annihilation was shown not to exceed 10% [5]; therefore its contribution to the cross-section may be safely neglected in the derivation of the hadronic branching ratios.

In the following the most important features of some analyzed two-body channels will be described.

5.1. Trends of simplest reactions

The $\bar{n}p \rightarrow \pi^+\pi^0$ reaction may proceed only from S- and D-waves, namely from $^3S_1$, $^3D_1$ and $^3D_3$. The events were selected applying a 2C kinematic fit to the one-prong data set in order to single out $\bar{n}p \rightarrow \pi^+\gamma\gamma$ events, where the γ's directions could be measured thanks to the OBELIX electromagnetic calorimeter [57,86]. Fig. 31 shows the $\gamma\gamma$ invariant mass for these events, where the two peaks from π^0 and η may be clearly distinguished.

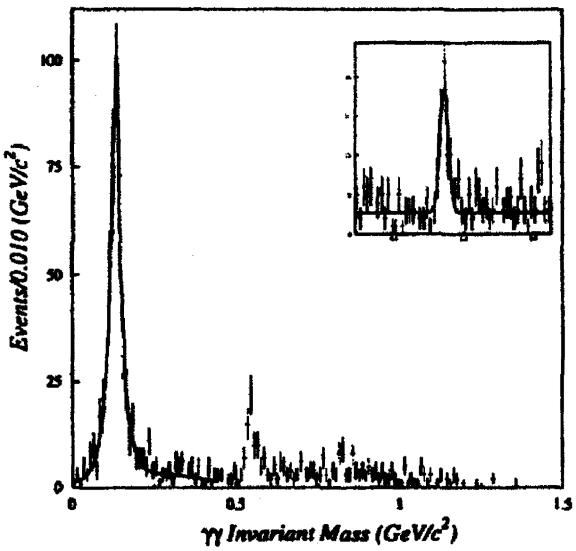

Fig. 31. Invariant mass of the $\gamma\gamma$ system, with events selected by means of a 2C fit, OBELIX data. The inset reports with better detail the η peak. From Ref. [86].

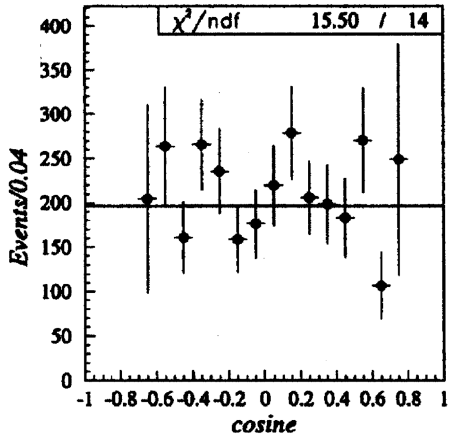

Fig. 32. Cosine of the angle between the π^+ direction and the beam axis in the reaction center of mass, OBELIX $\bar{n}p \to \pi^+\pi^0$ selected events. The line represents the result of a fit of the data with a flat angular distribution. From Ref. [86].

The distribution of the angle between the outgoing π^+ direction and the beam axis, reported in Fig. 32, is practically flat, suggesting an isotropic annihilation, as indeed expected from S-wave annihilation. The available statistics was distributed in three sub-sets as a function of the incoming $\bar{n}$ momentum ($p_{\bar{n}}$), and the annihilation cross sections in each interval were evaluated. Table 2 reports the cross sections for this channels evaluated in three $p_{\bar{n}}$ intervals, which in the following will be denoted as (a) $\sim 50 \leqslant p_{\bar{n}} \leqslant 200$ MeV/c, (b) $200 < p_{\bar{n}} \leqslant 300$ MeV/c and (c) $300 < p_{\bar{n}} \leqslant 405$ MeV/c.

Table 2
Collection of annihilation cross sections for selected two-body ($\bar{n}p$) annihilations, in three reference ranges selected according to $\bar{n}$ momentum

Reaction	σ_{ann} (mb) $\sim 50 < p_{\bar{n}} \leqslant 200$ MeV/c	σ_{ann} (mb) $200 < p_{\bar{n}} \leqslant 300$ MeV/c	σ_{ann} (mb) $300 < p_{\bar{n}} \leqslant 405$ MeV/c
$\bar{n}p \to \pi^0\pi^+$	0.291 ± 0.059	0.230 ± 0.068	0.166 ± 0.049
$\bar{n}p \to K^0_S\pi^+$	0.244 ± 0.094	0.067 ± 0.022	0.055 ± 0.016
$\bar{n}p \to \phi\pi^+$	0.123 ± 0.019	0.085 ± 0.011	0.061 ± 0.011
$\bar{n}p \to \omega\pi^+$	1.23 ± 0.13	1.07 ± 0.11	0.97 ± 0.11
$\bar{n}p \to \eta\pi^+$	0.153 ± 0.045	0.207 ± 0.037	0.233 ± 0.036
$\bar{n}p \to \bar{K}^{*0}K^+$	0.175 ± 0.027	0.186 ± 0.023	0.179 ± 0.021

The evaluated annihilations frequencies were used, together with the frequencies estimated for $\bar{n}p \to \eta\pi^+$ (which proceeds from P-waves only) and for the $\bar{n}p \to K^+K^0_S$ reaction, to infer the initial states composition as well as the hadronic branching ratios for the two reactions. The annihilation frequencies were decomposed according to the expression

$$f_{ch} = \sum_L \alpha_L(i) W^L_{ch} \ , \tag{21}$$

where α_L are the decay fractions for the ith $p_{\bar{n}}$ interval and W^L_{ch} are the hadronic branching fractions for the (ch) channel, produced by the initial states of angular momentum L.

The $\bar{n}p \to K^+K^0_S$ events were selected by means of a 4C kinematic fit to test the $\bar{n}p \to K^+\pi^+\pi^-$ hypothesis, applying then a cut on the $(\pi^+\pi^-)$ system invariant mass, whose plot is shown in Fig. 33, around the K^0_S peak. This reaction may proceed, including D-wave as well, from five initial states: $^3S_1$, $^3P_0$, $^3P_2$, $^3D_1$, $^3D_3$.

The solution of the linear equations system of Eq. (21), mentioned in Section 3.2, where α_S had been parametrized following Dover–Richard potential model [4,51], led to the following conclusions:

- the hadronic branching ratios from S-wave for both $(\pi^+\pi^0)$ and $(K^+K^0_S)$ channels are:

$$W_{\pi^+\pi^0}(^3S_1) = (3.1 \pm 0.5) \times 10^{-3} \ ,$$
$$W_{K^+K^0_S}(^3S_1) = (1.3 \pm 0.2) \times 10^{-3} \ ;$$

- using the previous value for $W_{K^+K^0_S}(^3S_1)$ as well as the branching ratios from $^3S_1$ for the $\bar{p}p \to K^+K^-$, $K^0\bar{K}^0$ reactions [90], which proceed from both $I = 0$ and $I = 1$ initial states, one gets that the $(K\bar{K})$ amplitudes from both the isospin sources have comparable intensities. We recall, as figures of merit, that the average values of the measured branching ratios for the $\bar{p}p \to K^+K^-$, K_SK_L annihilations at rest in liquid hydrogen (where the S-wave amount is about 90%) are, respectively, $B^{liq}_{K^+K^-} = (0.992 \pm 0.017) \times 10^{-3}$ and $B^{liq}_{K_SK_L} = (0.784 \pm 0.032) \times 10^{-3}$ [91];
- a suppression of the $(K^+K^0_S)$ channel from P-wave is suggested, in agreement with the evaluations of $\bar{p}p \to K^+K^-$ branching ratios, which decrease of a factor of four going from S- to P-wave;

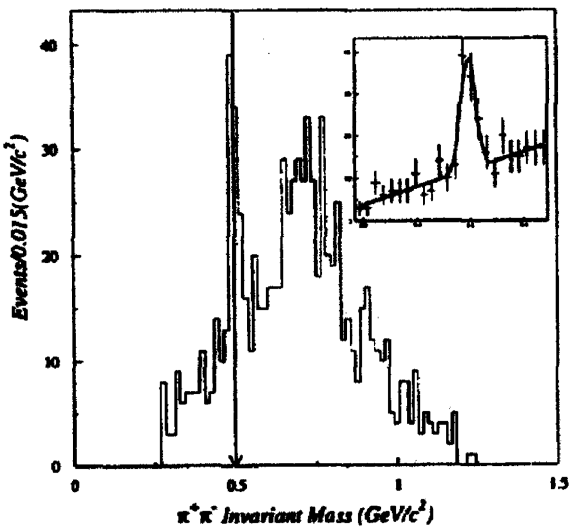

Fig. 33. Invariant mass of the $(\pi^+\pi^-)$ system, for $\bar{n}p \to \pi^+\pi^- K^+$ events selected by means of a 4C fit, OBELIX data. The K^0_S peak is shown in the inset as well. From Ref. [86].

- a non-negligible contribution from D-waves is needed only for higher $\bar{n}$ momentum values, not exceeding, though, 5%, in agreement with estimations deduced directly from $(\bar{n}p)$ annihilation cross sections [57] (see Section 3.4).

5.2. (ϕ, π^+) *and* (ω, π^+) *annihilation reaction*

According to the non-relativistic quark model, the physical states are obtained via a mixing between the SU(3) singlet and octet eigenstates. If the mixing were ideal, the production of the ϕ meson, composed of strange quarks only, would not be possible in reactions induced by hadrons composed of light quarks [92]; this is the basic formulation of the well known OZI rule [93–95] However, the deviation of the physical mixing angle from the ideal one ($\delta \simeq 3.2^\circ$ in the vector mesons sector), implies a relative probability of producing ϕ mesons in light hadrons induced reactions, as compared to ω production, of $R_{OZI} = 4.3 \times 10^{-3}$ (as evaluated from Okubo's quadratic mass-formula).

Any deviation from this value would indicate the presence of some other dynamic mechanism responsible for an abnormal $(\bar{s}s)$ quarks production in the annihilation reaction. An early measurement of OZI rule violation in the $\bar{n}p \to \phi\pi^+$ channel was performed on a first sample of OBELIX data with $\bar{n}$ momentum lower than 300 MeV/c [96]: the violation, measured from the comparison of ϕ and ω yields when they recoil against the same spectator particle, was shown to be as large as a factor of 33 with respect to the expected R_{OZI} value.

The extent of OZI rule violation was moreover shown to be strongly dependent on the quantum numbers of the initial state. The $\bar{n}p \to \phi\pi^+$ reaction, given the $J^{PC} = 1^{--}$ quantum numbers for ϕ, may proceed from $^3S_1$ and $^1P_1$ initial states only. Since the first observations by ASTERIX [97] it has become clear that the production of the $\phi\pi$ final state in $\bar{N}N$ S-wave annihilations is enhanced, as compared to the level expected by OZI. They quoted, for the $\omega\pi^0/\phi\pi^0$ ratio from

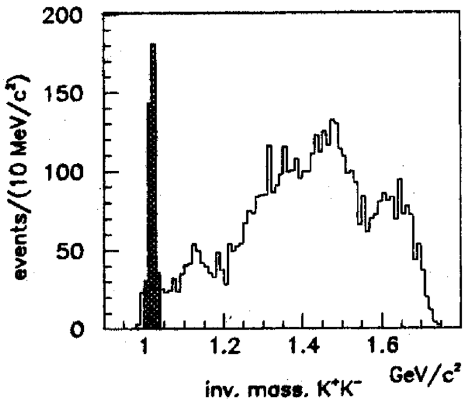

Fig. 34. Invariant mass of the (K^+K^-) system, with events with one kaon only identified by means of OBELIX specific ionization and/or time of flight measurements. From Ref. [87].

S-wave $\bar{p}p$ annihilations, the value $r_S(\omega\pi^0/\phi\pi^0) = (14 \pm 3)$, corresponding to a OZI rule violation of a factor of about 30. Years later the Crystal Barrel Collaboration reported a measurement of the ratio $R = f(\phi\pi^0)/f(\omega\pi^0)$ for annihilation events in liquid hydrogen, giving $R_{\text{liq}} = (0.096 \pm 0.015)$ [98], a factor of about 20 larger than the expected OZI rule value.

OBELIX performed several measurements of the $\bar{p}p \to \phi\pi^0$ annihilation fractions, using hydrogen targets of different densities to control the relative population of S- and P-wave levels in the initial states (the denser the target, the more enhanced is the annihilation from S-wave), and a confirmation of this dynamical selection rule was obtained [99].

The use of $\bar{n}$'s allows a further check, as in this case it is possible to trace the existence of possible trends in annihilation frequencies and cross sections as a function of the incoming $\bar{n}$ momentum, since the beam particles annihilate in flight. The total available statistics, selected by applying specific ionization and/or velocity measurements provided by OBELIX to get a correct particle identification as a kaon for at least one particle per event, was then distributed in the three intervals $\sim 50 \leqslant p_{\bar{n}} \leqslant 200$ MeV/c, $200 \leqslant p_{\bar{n}} \leqslant 300$ MeV/c and $300 \leqslant p_{\bar{n}} \leqslant 405$ MeV/c.

The (K^+K^-) invariant mass spectrum for the all the selected events, showing a clear ϕ peak, is reported in Fig. 34, while Fig. 35 shows the reaction Dalitz plot in which, besides the vertical band corresponding to ϕ, even an horizontal band relative to K^{0*} can be clearly distinguished.

A proof of the dominant production of the ($\phi\pi^+$) final state from S-wave is given by the shapes of the distribution of the ϕ decay angle, which are compatible with a $\sin^2\theta$ distribution for every sample, independently on the $\bar{n}$ momentum value. On the other hand, the expected distribution for annihilations from P wave should exhibit a $(1 + p^2/s \cdot \cos\theta)$ shape, where $\sqrt{s}$ is the total available energy, and $p^2 = (s - m_\phi^2 - m_{\pi^+}^2)^2 - m_{\pi^+}^2$. The fit of the experimental distributions with a mixture, with free weights, of S- and P-wave contributions reports $(96.1 \pm 2.1)\%$ as lower limit for S-wave (obtained from the highest momentum band data sample). The experimental distributions are reported in Fig. 36.

Evaluating the annihilation efficiencies for this channel under the hypothesis of production from pure S-wave, one gets for the cross sections in the three intervals the values reported in Table 2. Their trend with the $\bar{n}$ momentum is decreasing, and, graphically, the corresponding points can be

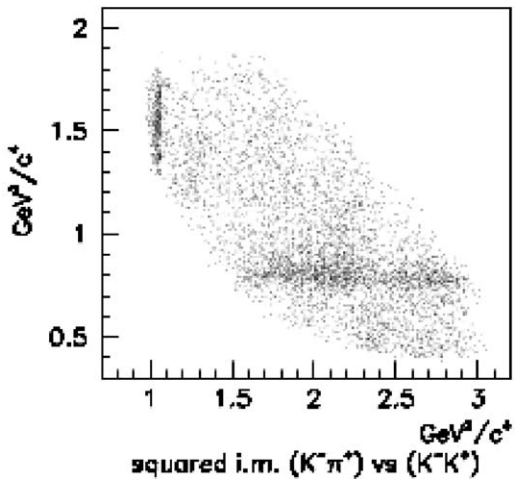

Fig. 35. Dalitz plot for the reaction $\bar{n}p \to K^+K^-\pi^+$, data collected by OBELIX with $p_{\bar{n}}$ up to 405 MeV/c. From Ref. [87].

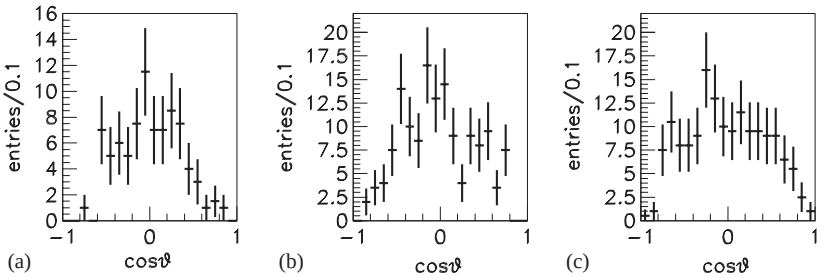

Fig. 36. Distributions of the angle between the direction of one kaon in the ϕ center of mass and the ϕ line of flight, in the reaction rest frame, for data selected in the three $p_{\bar{n}}$ ranges (a) ($\sim$ 50–200) MeV/c, (b) (200–300) MeV/c, (c) (300–405) MeV/c. From Ref. [87].

easily accommodated on the curve giving the annihilation probability from S-wave evaluated by Dover–Richard potential model [4] (see Fig. 1), as reported in Fig. 37a. A further confirmation of the dominant ϕ production from S-wave can be inferred, moreover, from the ratio between the annihilation cross-sections for the $(\phi\pi^+)$ and $(\pi^0\pi^+)$ channels, which is almost constant over the full available energy range [87].

The initial states from which the $\bar{n}p \to \omega\pi^+$ reaction may proceed are the same as for $\phi\pi^+$; however, in this case no dynamical selection rule is observed. The events have been selected applying the λ parameter method [100] to evaluate the number of ω mesons present in each sample, after a general selection by means of energy-momentum conservation cuts and 1C kinematic fit in order to single out $\bar{n}p \to 2\pi^+\pi^-\pi^0$ events (the ω is searched in its $\omega \to \pi^+\pi^-\pi^0$ decay channel). The invariant mass spectrum for the $\pi^+\pi^-\pi^0$ events selected in such a way is shown in Fig. 38, where the signal from ω as well as from η are clearly visible.

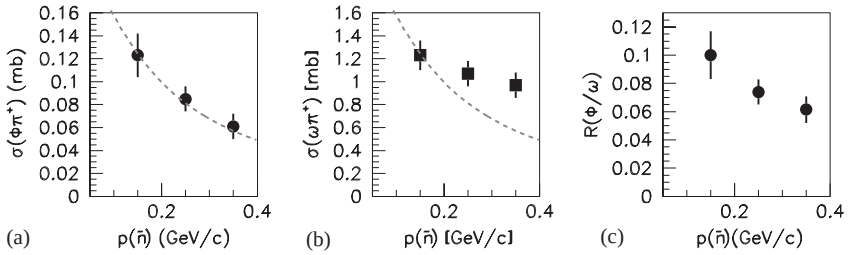

Fig. 37. Trends as a function of $\bar{n}$ momentum of: (a) $(\phi\pi^+)$ and (b) $(\omega\pi^+)$ cross sections. The curve superimposed is the trend expected for pure S-wave annihilation as given by Dover-Richard model. (c) Ratio $R_{\pi^+}(\phi/\omega)$ between the ϕ and ω yields, as a function of $p_{\bar{n}}$. From Ref. [99].

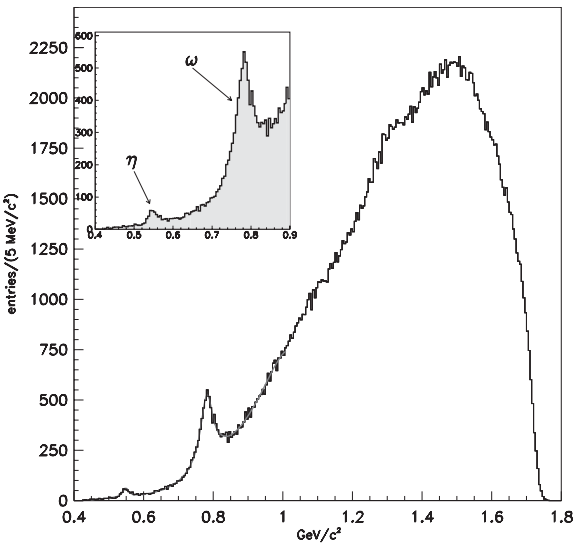

Fig. 38. Invariant mass of the $(\pi^+\pi^-\pi^0)$ system, data collected by OBELIX, integrated over all $p_{\bar{n}}$ values up to 405 MeV/c. The data selection criteria are described in the text. From Ref. [87]. In the inset the mass region with the η and ω peaks is shown in more detail.

The distributions for the ω decay angle θ_ω (between the normal to the decay plane in the ω rest frame and the ω line of flight in the reaction rest frame) are not compatible with a pure S-wave trend. Again, one would expect a $\sin^2\theta_\omega$ shape for annihilations from $^3S_1$ initial state, and a $(1+a\cos^2\theta_\omega)$ shape (where a depends on kinematic factors, as illustrated above in the $\phi\pi^+$) case for $^1P_1$.

The experimental angular distributions are reported in Fig. 39. Thanks to the large available statistics, a partial-wave fit could be performed on the ω decay Dalitz plot, inferring the amount of S- and P-wave annihilation in each of the intervals under study; a contribution as large as $(42\pm6)\%$ was found for the events with the highest $\bar{n}$ momenta. For the lowest $\bar{n}$ momenta, the minimum amount of P-wave found was $(19\pm5)\%$ [87]. Given the relative contributions of S- and P-wave in each interval, the annihilation efficiencies were evaluated with correct weights (since they depend on the angular distribution of the emitted particles, and therefore on the initial state from which

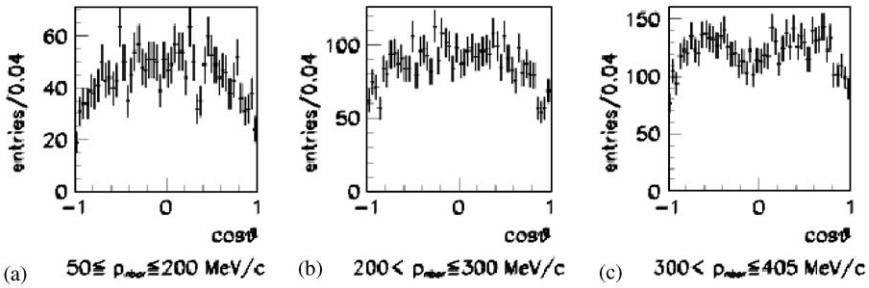

Fig. 39. Angular distribution of the ω decay angle (between the normal to the ω decay plane in the ω rest frame and the ω line of flight in the reaction rest frame), for experimental data selected in the $p_{\bar{n}}$ ranges (a) ($\sim$ 50–200) MeV/c, (b) (200–300) MeV/c, (c) (300–405) MeV/c. From Ref. [87].

each annihilation proceeds), and then the annihilation cross-sections, whose values are reported in Table 2. These values are pictorially sketched in Fig. 37b; their trend deviates remarkably from the curve representing the pure S-wave annihilation, according to Dover–Richard model.

5.3. (η, π^+) and (η', π^+) annihilation reaction

In the pseudoscalar meson sector the mixing is far from being ideal. Several observations of the pseudoscalar physical mixing angle agree with the value suggested by the Gell–Mann–Okubo linear mass formula, $\Theta_{PS} \simeq -23^\circ$ [101]. According to this picture, the η should be the meson of the octet with dominant light quark content, while in η' a more consistent strange quark component should be present. An accurate evaluation of the pseudoscalar mixing angle was provided by the Crystal Barrel Collaboration exploiting the $\bar{p}p \to \eta\pi^0$ and $\bar{p}p \to \eta'\pi^0$ annihilation reactions [102]: $\Theta_{PS} = -(17.3 \pm 1.8)^\circ$.

Due to the pseudoscalar quantum numbers of the two mesons, both $\bar{n}p \to \eta\pi^+$ and $\bar{n}p \to \eta'\pi^+$ proceed from P-wave initial states, namely $^3P_0$ and $^3P_2$. The available statistics collected by OBELIX is not enough to trace the production of η' as a function of the $\bar{n}$ momentum, but for η this is indeed possible [88,103].

The most efficient way to select η mesons with OBELIX was to exploit their $\eta \to \pi^+\pi^-\pi^0$ decay mode. The events have been selected applying a 1C kinematic fit, to test the $\bar{n}p \to 2\pi^+\pi^-\pi^0$ hypothesis, on the three prong ones compatible with the presence of three charged pions and an additional π^0. Moreover, a cut was applied on the momentum of the fastest π^+, which should recoil against the η with a momentum around 650 MeV/c. In this way the background under the η signal is reduced of 80%; the $(\pi^+\pi^-\pi^0)$ invariant mass spectrum for the selected events is shown in Fig. 40, to be compared to Fig. 38: a clear peak of ω emerges in this case as well.

With the η events selected by means of background subtraction from the invariant mass peak, in selected antineutron momentum ranges, angular distributions were made. They are reported in Fig. 41. They are fully compatible with a flat distribution, which would be expected for a two-body reaction with two pseudoscalar mesons produced from spin triplet P-wave. This observation was used to evaluate correctly the annihilation efficiencies, which depend critically on the partial waves from which the annihilation proceeds. Then, the evaluated cross-sections are reported in Table 2.

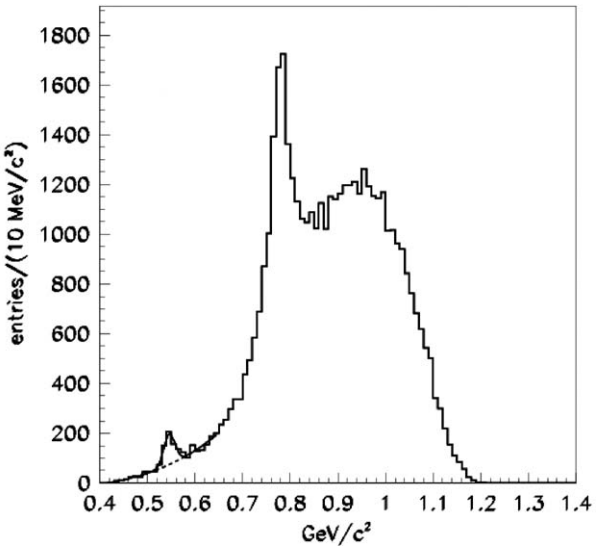

Fig. 40. Invariant mass of the $\pi^+\pi^-\pi^0$ system recoiling against a fast π^+ ($p_{\pi^+} > 600$ MeV/c), data collected by OBELIX, integrated over all $p_{\bar{n}}$ values up to 405 MeV/c. The η peak is fitted by a Gaussian plus a third degree polynomial function. From Ref. [88].

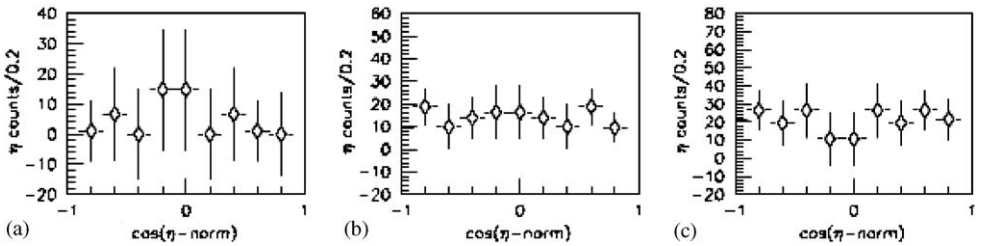

Fig. 41. Angular distribution of the η decay angle (between the normal to the η decay plane in the η rest frame and the η line of flight in the reaction rest frame), for experimental data selected in the $p_{\bar{n}}$ ranges (a) ($\sim$ 50–200) MeV/c, (b) (200–300) MeV/c, (c) (300–405) MeV/c. The plots are already acceptance corrected. From Ref. [88].

Several ways to select $\bar{n}p \to \eta'\pi^+$ channel were devised to extract the maximum information from the available data. An annihilation cross section value for the full sample was evaluated and compared to the $(\eta\pi^+)$ one in the same $\bar{n}$ momentum range, to estimate the pseudoscalar mixing angle. The $\eta' \to \eta\pi^+\pi^-$ charged decay mode was used, while for η both the charged and the neutral $\eta \to \gamma\gamma$ decay modes were searched for (in the second case η was considered as missing). All the selected events are required to have one and only one positive pion with a momentum larger that 600 MeV/c (π_f^+). The plots in Fig. 42 show the invariant mass of the $(\eta\pi^+\pi^-)$ system, as well as the squared missing mass of the system recoiling against the fastest recoiling π_f^+, for events selected with the following criteria: (i) 2C kinematic fit to test the $\bar{n}p \to \pi_f^+\pi^+\pi^-\eta$, with η decaying in its charged mode, on events with five charged pions and a π^0 selected by means of a 1C fit

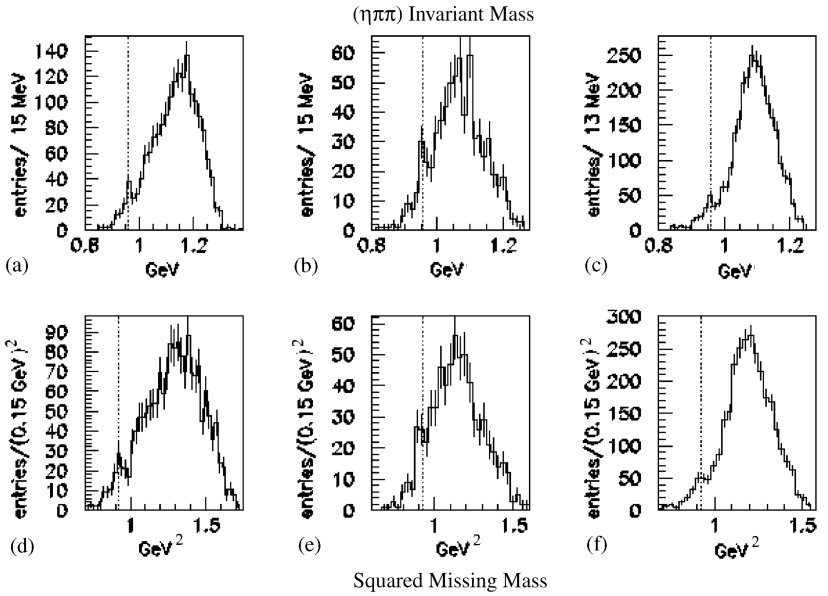

Fig. 42. ($\eta\pi^+\pi^-$) invariant mass system a, b, c and squared missing mass distributions for the system recoiling against the π^+ in the $\bar{n}p \to \eta'\pi^+$ reaction d, e, f. The applied selection criteria are described in the text. Data collected by the OBELIX experiment with $p_{\bar{n}}$ up to 405 MeV/c, Ref. [88].

(Fig. 42a and d); (ii) 3C kinematic fit to test the $\bar{n}p \to \eta'\pi^+$ hypothesis with energy-momentum conservation imposed at both the η and η' decay vertices, applied on the same six pions data (Fig. 42b and e); (iii) a 1C kinematic fit to test the hypothesis $\bar{n}p \to \pi^+_f\pi^+\pi^-\eta_{\rm miss}$, as well as to reject the $\bar{n}p \to \pi^+_f\pi^+\pi^-\pi^0$ one (Fig. 42c and f). The total amount of selected events, applying the three methods, was about 50. These are the first and only observations for an η' signal in OBELIX data.

The cross section for the reaction, with $\bar{n}$ momentum from $\sim$ 50 to 405 MeV/c, was quoted as $\sigma(\bar{n}p \to \eta'\pi^+) = (0.128 \pm 0.043_{\rm stat} \pm 0.011_{\rm sys})$ mb [88]. In the same momentum range, the cross section for $\eta\pi^+$ is $\sigma(\bar{n}p \to \eta\pi^+) = (0.203 \pm 0.019_{\rm stat} \pm 0.014_{\rm sys})$ mb. From the ratio between the two yields, $R = N_{\eta'}/N_\eta = (0.63 \pm 0.16_{\rm stat} \pm 0.04_{syst})$, one can get the value for the pseudoscalar mixing angle, with a proper phase space correction to account for mesons productions and possible dynamics effects, as pointed out, for example, by Vandermeulen [104]. The evaluation is somehow model dependent, since it's very sensitive to the way the phase space corrections are applied, however all the values found are in good agreement with theoretical expectations. The value $\Theta_{PS} = (-17.59^\circ \pm 3.39^\circ_{\rm stat} \pm 0.82^\circ_{\rm sys})$ was found [88], in good agreement with Crystal Barrel evaluation [102].

According to Quark Line Rule (i.e., the Naive quark model), if in η and/or η' the ($s\bar{s}$) quark content were sizeable, one should expect a marked suppression in their production. It is possible to infer the extent of quark line rule violation once the yields ratio R (as reported above) is known. A good agreement between the expectations of the Naive quark model and the experimental data is found, so no violation is seen in the pseudoscalar sector.

5.4. OZI-rule violation and possible interpretations

In the vector meson sector a sizeable violation of OZI rule is evident in certain experimental situations: the production of the ϕ meson, as observed in $\bar{N}N$ annihilation reactions, is exceedingly high as compared to Quark Model expectations. Comparing the production yields for ϕ and ω recoiling against the same particle in $(\bar{p}p)$ and $(\bar{n}p)$ the OZI rule is found to depend on several factors, like the mass of the recoiling particle (i.e. on the momentum transfer), and the quantum number of the initial states from which the reaction may proceed [92]. A violation as big as a factor of about 35 was measured in the $(\phi\pi)$ channel, as compared to $(\omega\pi)$; most of the measurements were performed by OBELIX [99]. It is however important to remind that several annihilation channels (like $(\phi\eta)$ [105], or $(\phi\pi\pi)$ [106]) don't exhibit exceedingly anomalous behaviors.

Fig. 37c shows the trend of the OZI experimental ratio $R^S_{\mathrm{OZI}} = f_\omega/f_\phi \cdot \sigma(\bar{n}p \to \phi\pi^+)/\sigma(\bar{n}p \to \omega\pi^+)$ (where the f's are phase space correction factors implemented following the prescriptions by Ref. [104]), in three selected $p_{\bar{n}}$ ranges. It is clear that all the values deviate strongly from the OZI-expected value R_{OZI}, and in a larger way the lower the $\bar{n}$ momentum is, as a consequence of the already discussed S-wave dominant production for ϕ, which becomes more diluted with the energy increase.

Several explanations have been proposed to account for this anomalous behavior. The formation of a $(s\bar{s}q\bar{q})$ multiquark resonant state, known as C(1480), with dominant $\phi\pi$ decay, had been suggested [107] but, apart from a unique observation in the $\pi^- p \to \phi\pi^0 n$ reaction [108], no other evidences for such a state were found.

Two are the approaches which nowadays provide the most convincing explanation for this anomalous behavior: one is based on the inclusion of intermediate rescattering amplitudes to attain the final state [109–111]; the second one derives from the EMC measurements at high energies, which have shown a sizeable $(s\bar{s})$ condensate to be present in the nucleon, and adapts this observation to the low-energy regime supposing that even in this case some effects of this condensate may already show up [112,113]. In both the approaches the quark line rule formulation is preserved, and ϕ production is allowed thanks to connected quark diagrams, which arise from the presence of open strangeness intermediate states, or of $(s\bar{s})$ clusters in the initial states wavefunctions.

According to rescattering models the final state can be reached through intermediate diagrams of second and third order, like $(\bar{K}K^*)$ and $(\rho^+\rho^-)$. The branching ratios into the given final state may be deduced including all the intermediate amplitudes, taking care of the possible cancellations between some of them. The approach is straightforward and is able to reproduce accurately enough many experimental results, among which the branching ratio for the $\phi \to \gamma f_0(980)$ radiative decay [114], whose size hints at a sizeable $(s\bar{s})$ content in the scalar meson, compatible with one of its most common interpretations, a $\bar{K}K$ molecule.

As a drawback, the possible dependence on spin and quantum number effects cannot be easily embedded in this framework. In same cases, unfortunately, the predictions from these models fail in a rather sizeable way (for instance of two order of magnitude, in the tensor sector case); moreover, sometimes the assumptions on which some deductions are based are not easily justifiable. One of the most critical points is the assumption of a $(\bar{K}K^*)$ suppression from P-wave, which can easily account for the S-wave ϕ production, but is contrary to some experimental observations. For instance, the study of the $\bar{p}p \to K^*\bar{K}$ annihilation reaction shows that sizeable contributions come from both $^3S_1$ and $^1P_1$ initial states [115]. With $\bar{n}$'s, OBELIX could show that the trend as a function of the

momentum of the $\bar{n}p \to K^+\bar{K}^{0*}$ cross sections (reported in Table 2) is constant, implying a relevant contribution from P-waves as well. In this case, due to the fact that G-parity is not defined for K^*, no relevant selection rules apply, therefore all possible S- and P-wave hyperfine sublevels may produce the measured final state.

The second approach rests, on the contrary, on the existence of pre-formed long-living ($s\bar{s}$) quarks condensates inside nucleons, which can be emitted through a full shake-out or via rearrangement of the quark lines to form open and hidden strangeness mesons in the final state. As observed by deep inelastic scattering experiments, the ($s\bar{s}$) pair has an own polarization, opposite to the nucleon one—for this reason the approach is known as "polarized intrinsic strangeness" model [112,113]. The polarization of the ($s\bar{s}$) pair allows to infer some relationships between the spin and angular momentum configuration of the initial and final states. The existence of a $J^{PC} = 1^{--}$ ($s\bar{s}$) cluster in at least one nucleon in the initial state could explain the production of ϕ mesons by direct expulsion. However, this hypothesis should imply a universally enhanced ϕ production, independently on the nature of the recoiling particle, contrary to experimental observations. If the ($s\bar{s}$) has the vacuum quantum numbers, $J^{PC} = 0^{++}$ ($^3P_0$), ϕ (and other hidden strangeness) mesons could be produced via a rearrangement of the quark lines between the hadrons of the initial state. This means that to get a spin one object recoiling against a pion the initial state must be in $^3S_1$ wave, which is indeed occurring, as shown by experimental results. This spin configuration for the ($s\bar{s}$) cluster should moreover favor the enhancement of pseudoscalar mesons production from spin singlet initial states, which happens for the ($\eta\phi$) final state whose production is enhanced in $^1P_1$, as well as a more abundant tensor meson production from spin triplet P-waves, which was observed too in the study of the ($f_2'(1525)\pi^0$) final state produced in $\bar{p}p$ annihilation at rest [115]. For the sake of completeness we must add that new results from $\bar{p}p$ annihilation in flight at higher momenta [116] show, though, that the most abundant $f_2'(1525)$ production proceeds from 2^{-+} wave, namely from $^1D_2$.

No experimental facts contrary to the polarized intrinsic strangeness model expectations have been found so far. This model is rather simple but very powerful in its predictions, which concern even baryon production, and are especially related to Λ and its polarization [117].

5.5. *Summary of two-body* $\bar{n}$ *annihilation reactions*

Selected two-body annihilation channels were measured by OBELIX to study whether they followed or not the behavior expected by quantum numbers selection rules and general trends of the $\bar{N}N$ annihilation process. The trends of $\bar{n}p \to \pi^+\pi^0$, $\bar{n}p \to K_S^0\pi^+$ and $\bar{n}p \to \phi\pi^+$ are compatible with a production proceeding mainly from S-wave, differently from what is observed in the $\omega\pi^+$ and $\bar{K}^{0*}K^+$ channels, which seemingly proceed from both S- and P-waves, and for $\bar{n}p \to \eta\pi^+$, for which the experimental observations confirm its occurring in spin triplet P-wave only.

In one case, namely the $\bar{n}p \to \phi\pi^+$ reaction, a strong violation of the OZI rule, generally valid for hadronic interactions, was observed. The ϕ production rate was ~ 35 times larger that the OZI rule prediction and both the angular distributions of kaons from ϕ decay and the $p_{\bar{n}}$ dependence of $\sigma(\bar{n}p \to \phi\pi^+)$ were consistent with the existence of a dynamical rule selecting only the $^3S_1$ initial state from the ($^3S_1, ^1P_1$) statistical mixture of the allowed states. A similar behavior was already reported for the $\bar{p}p \to \phi\pi^0$ annihilation at rest [97,118] but in the case of $\bar{n}$ annihilation there is the further evidence of the $p_{\bar{n}}$ dependence which makes the effect even clearer and more convincing.

Over several hypotheses suggested to explain the experimental observations the most convincing one seems to be that based on a "polarized intrinsic strangeness" content of the nucleon [112,113], able to explain also the $p_{\bar{n}}$ dependence of the ϕ production, whereas other models have difficulties in reproducing it correctly.

6. Meson spectroscopy with antineutrons

The $\bar{\mathcal{N}}\mathcal{N}$ annihilation provides a gluon rich environment suitable for the production of possibly exotic states with enhanced gluon content. Meson spectroscopy studies, especially in the low energy sector, have as main purpose the identification of such states, whose existence is foreseen by QCD (for a general review about light quark meson spectroscopy see, for instance, Ref. [119]).

The antineutron–proton annihilation reaction is a proper reaction for the study of meson production because of the absence of sizeable rescattering effects in the final states and the effectiveness of the initial states selection due to isospin conservation.

With $\bar{n}$'s one can get complementary results to $\bar{p}$ annihilations, with unprecedented cleanliness, due to the ease of selection of exclusive final states. Of course, the number of available results obtained with $\bar{n}$'s is little, because of the already mentioned difficulty of obtaining $\bar{n}$ beams of suitable intensity and momentum resolution. Again, the only two experiments able to give important results in the meson spectroscopy field are the already mentioned bubble chamber experiment by Banerjee et al. [67–69] and, especially OBELIX [120–125].

6.1. Annihilation into the exclusive $(\pi^+\pi^+\pi^-)$ channel

Two approaches can be adopted to study the features of annihilation reactions into three pion final states: one is based on final-state interactions [126], the other on dual amplitudes [127,128]. In the first case several assumptions about the particles' behavior are demanded for the construction of an amplitude good enough to reproduce the Dalitz plots features; on the other hand, dual models provide a natural and straightforward way to reproduce the Dalitz plot shape, simply based on the analiticity features of the annihilation reaction [129]. However, especially in the fits of high statistics samples, the interpretation provided by dual models is often too rough and additional "satellite" terms are needed to complete the basic amplitude [130], spoiling the original simplicity of the approach.

Both methods were used in the first attempts to analyze the features of the $\bar{n}p \to \pi^+\pi^+\pi^-$ reaction, with the data collected in the Saclay bubble chamber with $\bar{n}$ momentum up to 800 MeV/c, first on a partial sample consisting of 85 events only [67], then on the total available statistics, amounting to 197 events [69]. In this case a maximum likelihood technique was applied to fit simultaneously several coupled channels, namely all the exclusive channels with charged pions only (from three up to seven), and possibly a single additional π^0. The amplitudes inserted in the analysis of the $\bar{n}p \to \pi^+\pi^+\pi^-$ reaction described a direct three pion production and the two channels $(\rho^0\pi^+)$ and $(f_0\pi^+)$. The results provided are just on the qualitative level.

A much more refined analysis was on the contrary performed later on the charge-conjugated channel $\bar{p}n \to 2\pi^-\pi^+$, where 2785 annihilation events at rest were available [131,132]. In these events the spectator proton momentum was selected to be less than 150 MeV/c, in order to ensure

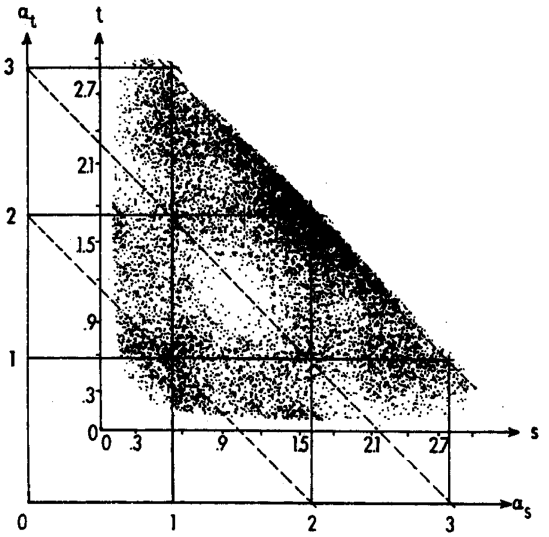

Fig. 43. Dalitz plot for the $\bar{p}n \to \pi^+\pi^-\pi^-$ annihilation at rest, with the results of dual amplitude analysis from Ref. [129] superimposed. See text for details.

a dominant annihilation from S-wave. The Dalitz plot for this reaction, shown in Fig. 43, exhibited peculiar features, which recall somehow the gross observations of Ref. [69]:

(i) the presence of a strong enhancement in the low region for the $(\pi^-\pi^-)$ invariant mass system, occurring almost where the two bands belonging to $f_2(1270)$ signal cross, at $m^2(\pi^+\pi_1^-) \simeq m^2(\pi^+\pi_2^-) \simeq 1.64\ \mathrm{GeV}^2$;
(ii) a hole close to the center of the Dalitz plot, with absence of events in the region $m^2(\pi^+\pi_1^-) \simeq m^2(\pi^+\pi_2^-) \simeq 1.08\ \mathrm{GeV}^2$;
(iii) a lack of events in the region where the invariant mass of one of the neutral dipion system is small, and the other is large;
(iv) an apparently abundant production of ρ^0 and $f_2(1270)$, that in the plot may be identified by vertical and horizontal bands.

The analysis performed in Ref. [131] was based on Breit–Wigner "form factors" to reproduce resonances as well as effective range amplitudes for non-resonant interactions (namely, the $(\pi\pi)$ isoscalar S-wave interaction, known as σ), and to Legendre polynomials to account for the spin-angular part. The introduction of the σ signal was of great importance, as well as an additional non-resonant isotensorial amplitude which was helpful to reproduce the lower $(\pi^-\pi^-)$ invariant mass region (more details about this problem will be given in Section 6.3). This last point especially was criticized by the dual amplitudes approaches, which claimed to be able to reproduce the Dalitz plot shape without resorting to any "exotic" amplitude as the isotensorial one.

Fig. 43 shows also the results of a dual amplitude analysis [129] on the $\bar{p}n$ data. The method consists of fitting the reaction Dalitz plot by means of an amplitude of the form

$$A(s,t) \propto \frac{\Gamma(1-\alpha_s)\Gamma(1-\alpha_t)}{\Gamma(2-\alpha_s-\alpha_t)}\ , \tag{22}$$

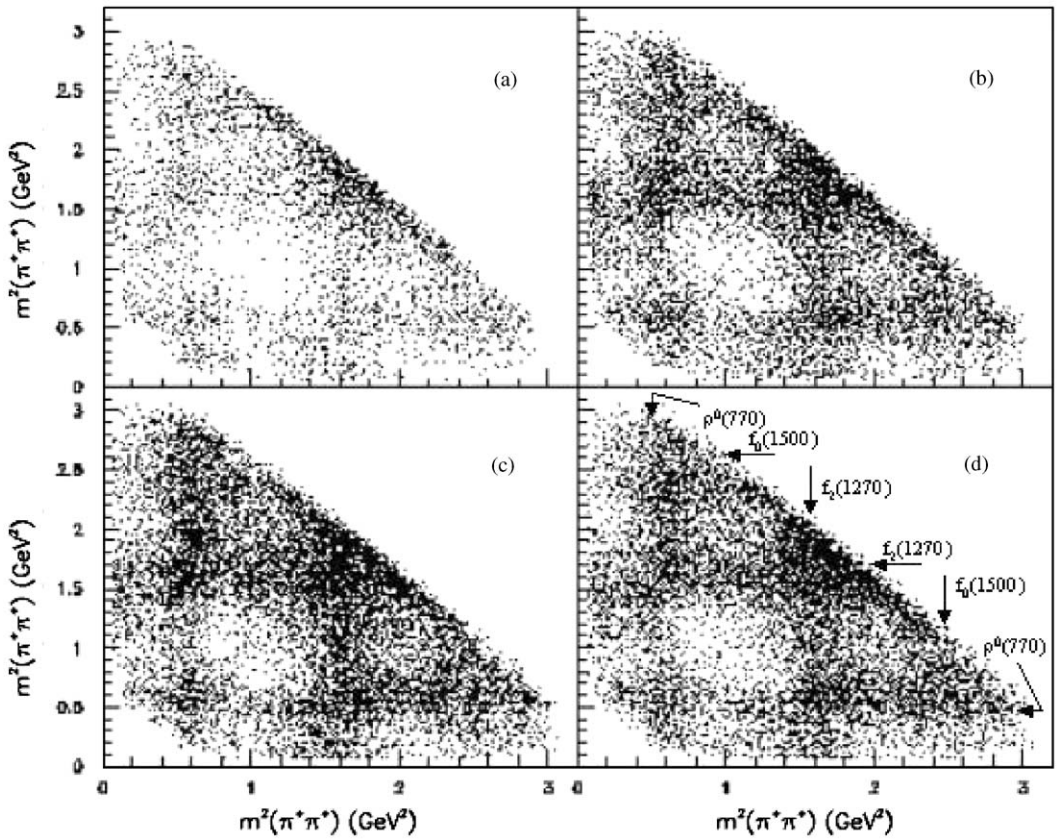

Fig. 44. Symmetrized Dalitz plots for the $\bar{n}p \to 2\pi^+\pi^-$ reaction ($m^2(\pi^+_{1,2}\pi^-)$ vs. $m^2(\pi^+_{2,1}\pi^-)$) for events selected according to $\bar{n}$ momentum values in the ranges: (a) $50 \leqslant p_{\bar{n}} \leqslant 200$ MeV/c, (b) $200 < p_{\bar{n}} \leqslant 300$ MeV/c, (c) $300 < p_{\bar{n}} \leqslant 405$ MeV/c, and (d) for the whole sample. From Ref. [121]. In plot (d) the arrows indicate the bands due to resonances production.

where $s \equiv m^2(\pi^+\pi^-_{1,2})$, $t \equiv m^2(\pi^+\pi^-_{2,1})$, and α_s and α_t are the known Regge-trajectory parameters. Corresponding to the singularities of the Γ functions the amplitude generates peaks and valleys which ought to reproduce the shape of the Dalitz plot. In Fig. 43 the solid lines correspond to the maxima of the Γ functions at the numerator of Eq. (22) (which should produce enhancements), while the dashed ones correspond to the maxima of the Γ functions at the denominator (which should produce holes). The main features of the plot may be described sufficiently well by this method; but the real hole depth and the peaks heights cannot be properly reproduced, as well as the region on the ρ^0 band with $m^2(\pi^+\pi^-_{2,1}) \simeq 2.3$ GeV^2.

With increased statistics one may observe in this region a real data clustering. This is evident considering the Dalitz plot built with the data collected by the OBELIX experiment (maximum value $p_{\bar{n}} = 405$ MeV/c), reported in Fig. 44 for events selected in ranges according to $\bar{n}$ momentum. The apparatus acceptance for all the plots and over their full volume was flat, within 3%, therefore density variations can be truly addressed to the presence of dynamical effects.

OBELIX collected a total of 35118 $\bar{n}p \to 2\pi^+\pi^-$ events, all of them selected by means of severe quality cuts applied on measured total momentum and energy and based on a 4C kinematic fit to

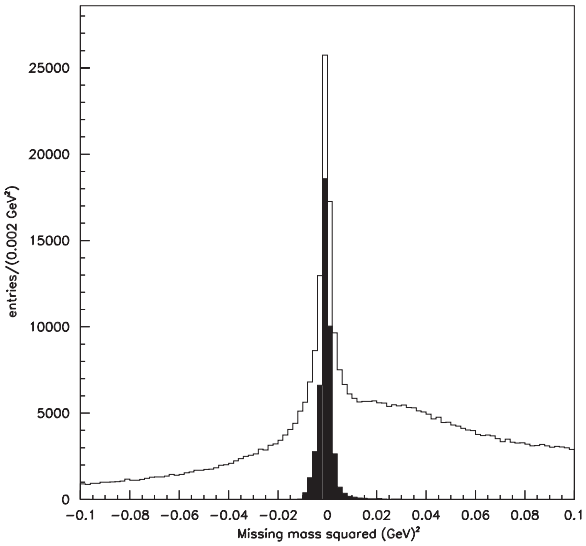

Fig. 45. Missing mass spectrum for $\bar{n}p \to 2\pi^+\pi^-$ events with topological selection only (white area) and for events selected by means of energy–momentum cuts and 4C kinematic fit (black area). From Ref. [121].

discard non-exclusive three pion events. The quality of the data reduction procedure for the selected data may be inferred from Fig. 45, where the black region in the $\bar{n}p \to 2\pi^+\pi^-$ missing mass plot represents the selected data. The resolution on the squared missing mass spectrum is better than $0.004\ \mathrm{GeV}^2$.

About the other features, the plots exhibit the same properties already observed in $\bar{p}n$ annihilations, in spite of the presumably enhanced P-wave content in these samples. With $\bar{n}$ in flight at low momentum, the annihilations may proceed, due to G-parity conservation, even from at least $^3P_1$ and $^3P_2$, besides $^1S_0$. The relative depth of the central hole is less pronounced for data selected with higher $\bar{n}$ momentum, as a consequence of the contribution of more partial waves to the annihilation.

6.2. The $(\pi^+\pi^-)$ invariant mass spectrum: contribution of the antineutron–proton annihilation data to the $f_0(1500)$ study

Fig. 46 shows the Dalitz plot projections for the data collected by the OBELIX experiment: the enhancement close to the Dalitz plots' corners observable in Fig. 44 can be clearly seen in the $(\pi^+\pi^-)$ invariant mass spectra as peaks around 1500 MeV. Their relative intensity, as compared to the full plots volume, is modulated with the variation of the $\bar{n}$ momentum.

The first attempt for a spin and parity assignment to this enhancement was performed by ASTERIX, in the study of the $\bar{p}p \to \pi^+\pi^-\pi^0$ reaction [133], with annihilations events in a NTP gaseous target selected with coincident L–X rays emission to enhance P-wave annihilations. A clear peak at about 1500 MeV could be observed in the $(\pi^+\pi^-)$ invariant mass system. The signal was however less pronounced if data without L–X rays selection were used. Excluding the possibility that it might be the neutral component of an isospin two multiplet (due to its absence in the $(\pi^\pm\pi^0)$ invariant mass systems), a spin-parity analysis based on final state interactions approach led to the

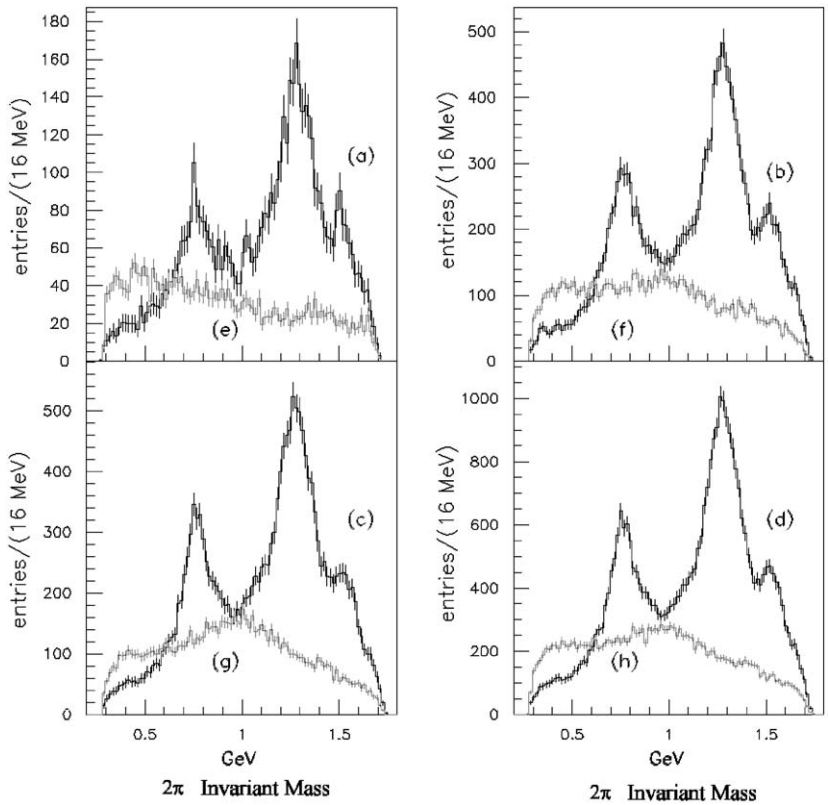

Fig. 46. Invariant mass distributions for the $m(\pi^+_{1,2}\pi^-)$ (2 entries/event) and $m(\pi^+_1\pi^+_2)$ (1 entry/event) systems for $\bar{n}p \to 2\pi^+\pi^-$ events selected according to $\bar{n}$ momentum values in the ranges: $50 \leqslant p_{\bar{n}} \leqslant 200$ MeV/c (plots a and e), $200 < p_{\bar{n}} \leqslant 300$ MeV/c (plots b and f), $300 < p_{\bar{n}} \leqslant 405$ MeV/c (plots c and g), and for the whole sample (plots d and h). Vertical rows have the same units and scale. From Ref. [121].

conclusion that it could be identified with a $J^{PC} = 2^{++}$ resonance, at a mass (1565 ± 20) MeV, (170 ± 40) MeV wide. The resonance was dubbed as $AX(1565)$; in the Review of Particle Properties [9] the state is now labelled as $f_2(1565)$. A tensor resonance in this mass region could well represent a $\bar{\mathcal{N}}\mathcal{N}$ quasi-nuclear bound state [47]. Besides the better fits quality, the tensor hypothesis appeared to be favored on several grounds, from the similarity of the pattern production of this signal as compared to $f_2(1270)$ (no production from the 0^{-+} ($^1S_0$) ($\bar{p}p$) initial state, some production from $^3P_2$ and strong production from $^3P_1$), to the absence of a similar signal in the same reaction occurring in liquid hydrogen (for instance in bubble chamber experiments), where S-wave annihilations could favor the production of a scalar state due to the absence of the centrifugal barrier.

In the following years, further observations of an analogous signal in the same mass region were performed in several other annihilation channels. The final state interaction approach had been extensively used, adopting for resonant states the usual Breit–Wigner parametrization completed with centrifugal barrier factors depending on angular momentum composition, or more sophisticated

treatments that preserve amplitude unitarity, like the K-matrix formalism which deals with several overlapping states with the same spin-parity. The dependence of the partial amplitudes on the relative angular momentum, total J and resonances' spin was accounted for by applying Zemach tensors [134,135], in their non-relativistic or covariant form [136,137].

All the first analyses confirmed the presence of a tensor signal, both in the $\bar{p}p \to 3\pi^0$ annihilation at rest in liquid hydrogen, with the first observations by Crystal Barrel [138], and in the first data collected by OBELIX in the $\bar{n}p \to 2\pi^+\pi^-$ channel [139], with 300 MeV/c as maximum $\bar{n}$ momentum. However, the statistics increase as well as the refinement of the analysis methods led to a partial retreat of these issues: the scalar hypothesis seemed to be more suitable to get a good fit, both in the Crystal Barrel $\bar{p}p \to 3\pi^0$ data [140] and in the $\bar{p}p \to \pi^+\pi^-\pi^0$ samples collected by OBELIX using targets of different density to select effectively the initial partial wave [141]. In addition, Crystal Barrel performed an analysis based on K-matrix formalism applied to coupled channels [142], which confirmed the presence of a third K-matrix pole in the scalar sector, corresponding to a state at $m = (1500 \pm 15)$ MeV, with $\Gamma = (120 \pm 25)$ MeV, to be added to the narrow $f_0(980)$ and the broad backgroundlike $f_0(1370)$. This state was labelled as $f_0(1500)$. Several speculations about its glueball nature have been proposed in the last decade [11,143]; more information about this topic will be given in Section 6.4.

Nonetheless, a contribution from a tensor state in the same mass region seemed to be required as well to get satisfactory results, so some doubts raised on the correct spin-parity assignment and on the identification of the observed signal. Ref. [142] reports, for the tensor state, a mass of about 1522 MeV; for annihilations at rest into $3\pi^0$ its weight on the whole Dalitz plot volume accounts for about 17%, to be compared to the 12% quoted for $f_0(1500)$.

The first hint for the presence of a double contribution was obtained by a reanalysis of the first sample of $\bar{n}p \to \pi^+\pi^+\pi^-$ events collected by OBELIX [144], with a renewed method taking into account the different formalism needed for in-flight annihilation. Care must be taken in this case, as the helicities (along the beam direction) are conserved, therefore the total amplitude is given by the incoherent sum over the helicity components of the initial states [121], differently from what happens for annihilations at rest.

The best fit was obtained adding to the already ascertained tensor state [123,139] a scalar one of lower mass. Quantitative results could however be achieved only when the complete statistics were available.

The OBELIX $\bar{n}$ data had the unique feature of allowing a selection of the total sample in several enough populated subsamples as a function of the $\bar{n}$ momentum. Data with different momentum have been collected at the same time and in the same experimental configuration, therefore systematic effects due to the sum of different samples are totally absent. As can be inferred from Figs. 44 and 46 the shape of the spectra varies with the available energy. Therefore, the production fractions of the intermediate states included in the amplitude may be evaluated for the different samples and eventually some trends may be deduced. This is of particular interest for the signal at 1500 MeV: if the hypothesis that it is given by the superimposition of two states with different spins is acceptable, different production intensities of each of them should be observed as a function of the available energy. The analysis performed on all the collected data [121] pointed out indeed the presence of definite trends for the production of the two states, as can be seen in Fig. 47.

The scalar state, parametrized by a non-interacting Breit–Wigner function, to which the fit assigns a mass and a width, respectively, $m = (1522 \pm 25)$ MeV and $\Gamma = (108 \pm 33)$ MeV, is produced with

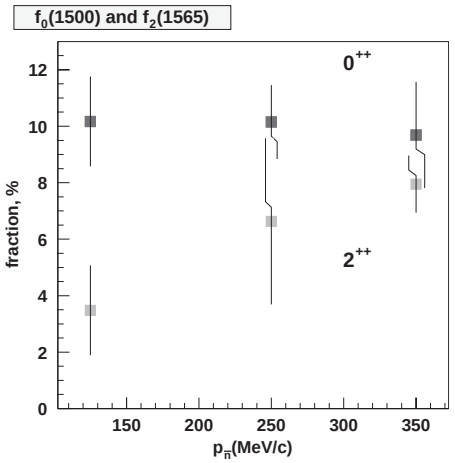

Fig. 47. Branching fractions for the production of $f_0(1500)$ (black squares) and $f_2(1565)$ (grey squares) in the $\bar{n}p \to 2\pi^+\pi^-$ reaction as a function of the $\bar{n}$ momentum.

an intensity of about 10% without dependence on the $\bar{n}$ momentum. On the other hand, the tensor signal, again a Breit–Wigner function peaking at $m = (1575 \pm 18)$ MeV, (119 ± 24) MeV wide, is produced with an intensity increasing with the $\bar{n}$ momentum, from about 3% for lower momenta up to about 8% for the highest ones. This observation is in agreement with the general notion that higher energies should favor the production of higher spin states.

In a spin-parity analysis the decay branching ratios are usually evaluated from the fit parameters (integrating the amplitudes over the full available phase space) without taking into account interference effects. Similar trends have been obtained in the same analysis for the production of other intermediate states as well as for the initial wave sources intensities, shown in Fig. 48a. The S-wave strength is about 1/3 of the P-wave one—the errors are too large to infer any particular trend in the initial states production as a function of the available energy. The "total" P-wave, however, comes from the combination of the two trends reported in Fig. 48b, which refer to the two hyperfine P-wave sublevels allowed for this annihilation reaction: the $^3P_1$ source strength is dominant but decreasing, while for $^3P_2$ it increases with the $\bar{n}$ momentum.

Due to the in-flight annihilation, the interference between the initial states arises only between the ± 1 helicity components of $^3P_1$ and $^3P_2$ waves, and was evaluated to account to less than 3% over the full Dalitz plot (as shown in Fig. 48a, open circles), almost independent on the reaction energy.

The dependence on the energy of both the production and decay branching ratios of each intermediate state imposed the use of a large number of free parameters, which prevented the application of a K-matrix approach, though more correct. The P-vector formalism was used instead to account for the production mechanism [145].

Some interesting features emerge from the inspection of Fig. 49, where the annihilation cross sections into the intermediate states inserted in the analysis are reported. These cross sections can be compared to those reported in Table 2. To fix a gauge, the cross section for $(\rho^0\pi^+)$ is, at least at higher momenta, a little less than the $(\omega\pi^+)$ one, while for $(f_2(1270)\pi^+)$ the strength is almost the same. They are reported pictorially since, differently from the values in Table 2 which come

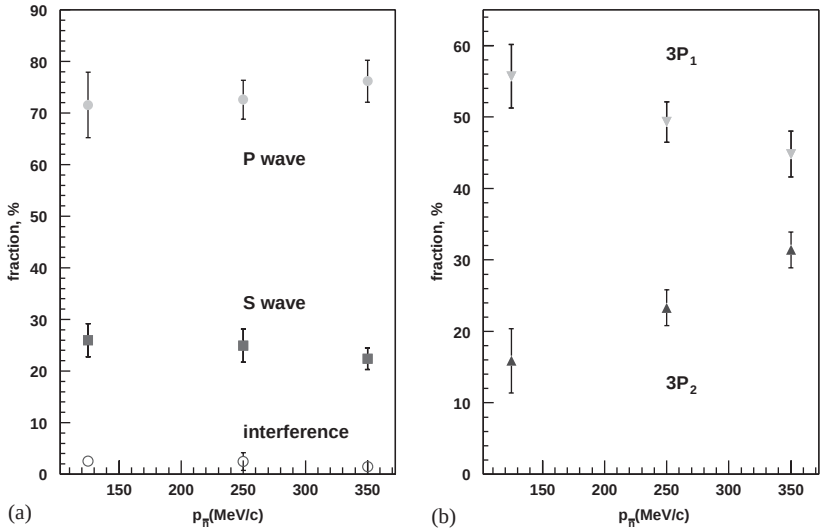

Fig. 48. Initial states contributions in $\bar{n}p \to 2\pi^+\pi^-$ as a function of the $\bar{n}$ momentum. (a): Contributions from S- (black squares) and P-wave (grey circles), and from interference between initial partial waves (open circles); (b) Contributions of $^3P_1$ (downward triangles) and $^3P_2$ (upward triangles) hyperfine levels.

from direct measurements, in this case the values are obtained by a spin-parity fit. Actually, the reported cross sections are based on branching fractions evaluations, which have been obtained out of a de-convolution of the single initial wave production, as a function of the available energy, and the hadronic branching ratio for the annihilation into the three charged pions final state, that in principle is energy-dependent just as well.

As observed by ASTERIX, the production trend of $f_2(1565)$ exhibits the same pattern as for $f_2(1270)$, strongly increasing in this case with the P-wave content, in the OBELIX case with the $\bar{n}$ momentum rise. The dominance of the $f_2(1270)$ signal over the full spectrum is confirmed, with a production branching fraction in the range (10–37)%. For the other scalar amplitudes, namely the σ for which a partial K-matrix was used [146] and the $f_0(1370)$, that was parametrized following Ref. [146] as a simple Breit–Wigner, the errors on the production branching fraction are rather sizeable and prevent to infer any conclusion about their possible trend as a function of energy. The relative annihilation frequency for σ ranges from a minimum of 10 to 30%. The fit assigns to $f_0(1370)$ a mass $m = (1280 \pm 55)$ MeV, and a width $\Gamma = (323 \pm 13)$ MeV. Its weight is almost as for σ. Due to its broadness, this amplitude can be interpreted as a sort of background, taking the place of a direct three-pion production amplitude, that in this analysis was not introduced.

The vector mesons inserted in the total amplitudes are the $\rho^0(770)$ and a possible ρ', that was required in other analyses [141,147] to get satisfactory fits (and was labelled as $\rho(1450)$). In this case its contribution was found not to exceed 15%; its best fit mass and width are $m = (1348 \pm 33)$ MeV, $\Gamma = (275 \pm 10)$ MeV. The trend of both the vector states branching fractions has the same pattern, with a maximum corresponding to the central $\bar{n}$ momentum interval. The ρ^0 contribution does not exceed 20%, in agreement with the observations of Ref. [131].

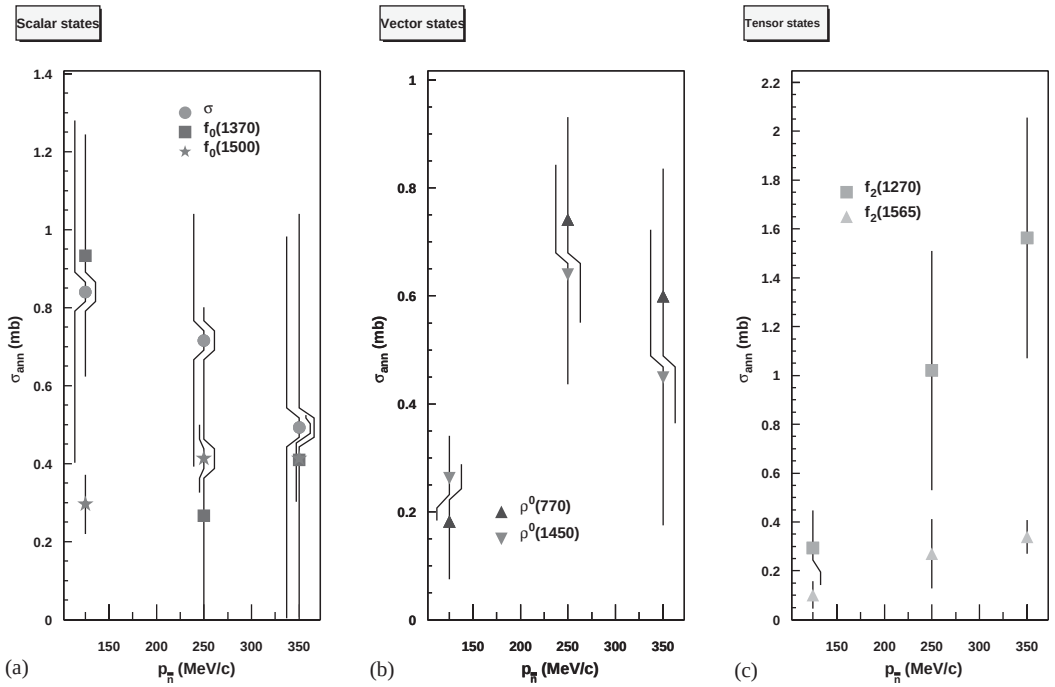

Fig. 49. Annihilation cross sections for several two-body intermediate states in $\bar{n}p \to 2\pi^+\pi^-$ as a function of the $\bar{n}$ momentum. The interferences effects have been omitted in the calculations. The states have been grouped in the pictures according to their spin and parity: (a) Scalar states: $\bar{n}p \to \sigma\pi^+$ (full circles), $\bar{n}p \to f_0(1370)\pi^+$ (full squares), $\bar{n}p \to f_0(1500)\pi^+$ (stars); (b) Vector states: $\bar{n}p \to \rho^0\pi^+$ (upward triangles), $\bar{n}p \to \rho'^0\pi^+$ (downward triangles); (c) Tensor states: $\bar{n}p \to f_2(1270)\pi^+$ (squares), $\bar{n}p \to f_2(1565)\pi^+$ (triangles).

6.3. *The* $(\pi^+\pi^+)$ *spectrum: hints for a* $I = 2$ *state at* 1420 MeV

Fig. 46e–h shows the invariant mass spectra for the $(\pi^+\pi^+)$ system, for $\bar{n}p \to 2\pi^+\pi^-$ events selected in $\bar{n}$ momentum intervals. Their shape does not show any peculiar irregularity, except for an enhancement at about 1 GeV which becomes more marked when higher $\bar{n}$ momenta are selected. However, this enhancement is not due to any dynamics but it's just the consequence of the kinematic reflection of the $f_2(1270)$ signal, which becomes indeed stronger for higher momenta. A more interesting feature of this distribution can be observed when considering the squared invariant mass plot, reported in Fig. 50 for the complete data sample, that shows more clearly a strong enhancement at low values, corresponding in the reaction Dalitz plots to the region along the plot border where the two $f_2(1270)$ bands are crossing. Even in this case, whether the enhancement is just a kinematic reflection or it is due to some underlying dynamics can be questioned. A possible contribution for a $(\pi^+\pi^+)$ resonant state, part of an isospin two multiplet, could show up in such a way. First hints at the possibility of observing such an object in $(\bar{n}p)$ annihilation were given in Ref. [148].

The possible presence of an isospin two multiplet at low masses is not so remote, even if the experimental observations of such states are very scarce. An isospin two object could be, for instance,

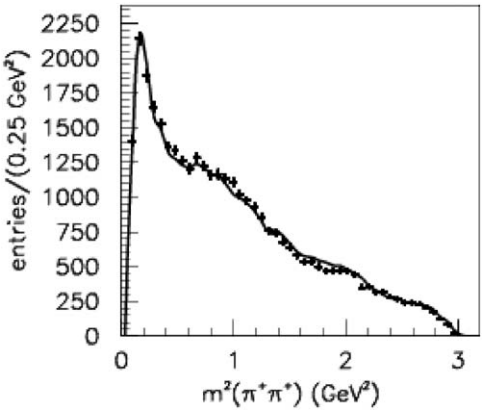

Fig. 50. $(\pi^+\pi^+)$ squared invariant mass distribution. The curve superimposed to the experimental data represents the best fit solution, obtained inserting a $(\pi^+\pi^+)$ scalar resonant state at 1420 MeV (corresponding to $m^2(\pi^+\pi^+) = 2.02\,\mathrm{GeV}^2$). The peak close to threshold is due to the kinematic reflection of $f_2(1270)$ bands. No peak appears in the spectrum at about 1420 MeV due to the weak strength of the isospin two signal. From Ref. [122].

a good candidate as a multiquark state. Namely, the representation in form of multiplet 27 of flavor SU(3) corresponds to a state with charge $Q = \pm 2$ and even spin, of $(\bar{q}q + \bar{q}q)$ structure [149].

Also according to MIT bag model [150] even spin and isospin multiplets should exist close to the vector–vector (VV) meson production threshold; therefore their observation in the VV channel should be easier. Their decay into two pseudoscalars should be suppressed due to a sort of OZI mechanism. The diquark cluster model [151] confirms, adopting a different approach, these expectations, foreseeing an isospin two $(qq\bar{q}\bar{q})$ multiplet in the (1350–1500) MeV mass range decaying preferentially in multipionic final states.

The only observation, so far, for an isospin two state was reported by the CELLO [152] and ARGUS [153] Collaborations for the state labelled by PDG as $X(1600)$, to which $J^P = 2^+$ was assigned. The evidence was based on an enhancement observed in the $\gamma\gamma \to \rho^0\rho^0$ cross section close to threshold, that hadn't any correspondence in the $\gamma\gamma \to \rho^+\rho^-$ channel. This particular decay pattern is compatible with the interference of at least two members of a same isospin two multiplet [154].

In the first analysis of $\bar{p}n \to \pi^-\pi^-\pi^+$ [131] an isospin two amplitude, either in the form of a Breit–Wigner or of an effective range expansion, was indeed inserted, and was shown to have a non-marginal role in the fits (as big as about 47%). This observation could not be conclusive due to the few available statistics; moreover, the determination of the $I = 2$ phase shift from this analysis was in disagreement with the general expectation from pion production reactions, that claims it to be small and negative [155]. According to recent theoretical predictions based on chiral models, it should lie in the range $-(0.027\text{–}0.005)m_\pi^{-1}$. The introduction of this "exotic" (and artificial) amplitude to get a good description of the data was sharply criticized, as already mentioned.

From that time on, no other attempt was made to insert isotensor intermediate states in the fits, up to a new try performed by OBELIX on the complete collected statistics [122,125, 156–158]. Only Crystal Barrel, later on, attempted as well to insert an isotensor amplitude in the fit of their $\bar{p}d \to \pi^-\pi^-\pi^+p_s$ data [159], but without obtaining remarkable results about the presence of new states.

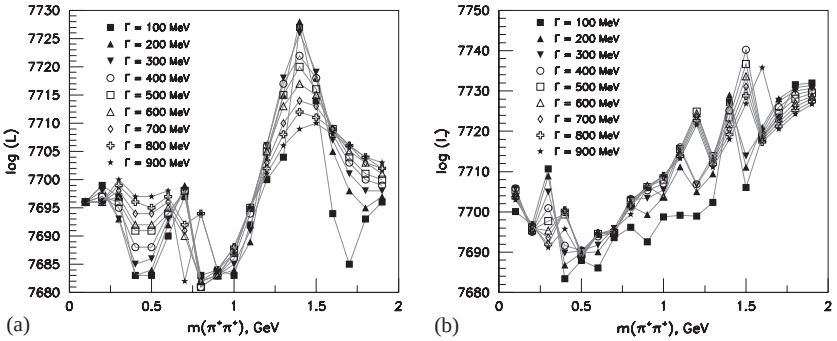

Fig. 51. log(likelihood) values for best fit solutions as a function of $(\pi^+\pi^+)$ invariant mass and for fixed values of the width of a possible isospin two resonant state, in the two cases (a) of a scalar resonance (b) of a tensor one. From Ref. [122].

OBELIX analysis was based on a scan on a discrete grid of masses and widths for a possible isotensor resonant state, parametrized by means of a Breit–Wigner function, with spin 0 and 2, in order to see whether a new state could be accommodated to get a better description of the data. Only the $|I, I_3\rangle = |2, +2\rangle$ component was inserted, as the strength of the neutral one, in comparison, is suppressed due to isospin Clebsh–Gordan composition. Contrary to expectations, some strong statistical indications for the existence of a new scalar state at 1420 MeV emerge from a collection of all the performed fits. The trends of the log(likelihood) as a function of the mass of the resonant state and for different widths in the two spin hypotheses are shown in Fig. 51: a clear peak is seen for the scalar hypothesis, corresponding to $m = (1420 \pm 20)$ MeV and $\Gamma = (160 \pm 10)$ MeV; no indication comes in the tensorial case.

However, the effect of the introduction of this signal in the amplitude is not visible in the invariant mass spectra, due to its weakness. Integrating over the full Dalitz plot, one can just fix an upper limit to its weight, which does not exceed 4×10^{-3}. A suppressed production strength is compatible with the expectations from the MIT bag model, as well as the diquark cluster one. If confirmed, this could be considered as the first observation of a scalar exotic meson in a mass region where some other exotic states, often interpreted as hybrids, are claimed to have been seen: for instance, the 1^{-+} exotic state observed at BNL by E852 [160] and at LEAR by Crystal Barrel, close to 1400 MeV [161,162].

Introducing an effective range expansion, the best fit value occurs for $a_2^0 = -(0.025 \pm 0.005)m_\pi^{-1}$; however the fit sensitiveness is too small to quote this value as a reliable estimation [158].

6.4. *Annihilation into the exclusive* $(3\pi^+2\pi^-)$ *channel and interpretation of the* $(2\pi^+2\pi^-)$ *mass spectrum*

The $\bar{n}p \to \pi^+\pi^+\pi^+\pi^-\pi^-$ exclusive reaction had been also studied to some extent, to get insight about the presence of possible resonant states decaying into four pions. The early bubble chamber $(\bar{n}p)$ experiment could single out 31 events belonging to the channel [69]. Including the sample in their coupled channel analysis, the Authors concluded that the final state is dominated by ρ^0 production (10% for single, 55% for double production). Their analysis was especially aimed to find

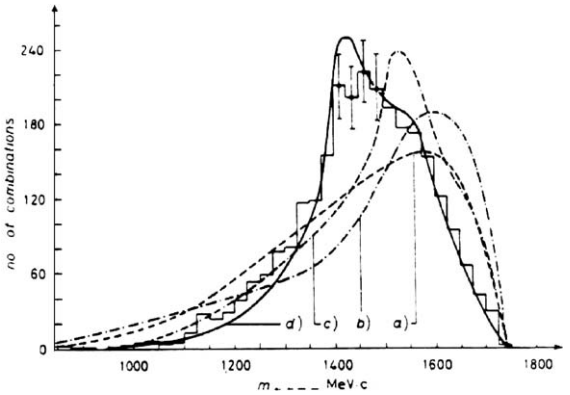

Fig. 52. Invariant mass spectrum for the $(2\pi^+2\pi^-)$ system, from Ref. [163]. The superimposed curves represent some fits to the data under several hypotheses, explained in the original reference.

some distortions in the four pions invariant mass spectrum (both for five and six pions final states) to confirm the observation of $X(1600)$; no new evidence was found.

However, even with just a few data, it became evident that the shape of the $(2\pi^+2\pi^-)$ invariant mass spectrum could not be simply explained resorting to phase space, but some more complicated dynamics had to be present. In the earliest work no resonant interpretation was given, rather it was suggested that probably the most enhanced resonance production should occur in final states where neutral pions as well are present [68]. Later, with more statistics, it was however shown that the five charged pions final state can only be interpreted by a multiple resonance production, in a rather complicated way due to the large combinatorial effects; the matter is still open.

In the late 1960s, in deuterium bubble chamber, the charge conjugated reaction $\bar{p}n \to 2\pi^+3\pi^-$ was studied [163]. The deformation of the neutral 4π invariant mass spectrum was explained as due to a scalar resonance with $(\rho^0\rho^0)$ dominant decay, to which a mass $m = 1490$ MeV and a width $\Gamma = 90$ MeV were assigned. As can be seen from Fig. 52, the 4π invariant mass spectrum shows a bump, but at a higher mass and with a larger width than the one quoted in Ref. [163].

Twenty years later the resonance was confirmed in a new bubble chamber experiment [164,165], at 1477, 166 MeV wide, and was dubbed $\zeta(1490)$. The fit was performed on the so-called difference spectrum, obtained by subtracting from the $(2\pi^+2\pi^-)$ invariant mass spectrum the $(3\pi^-\pi^+)$ distribution, in which, seemingly, no dynamic structure and kinematic reflections are present. In the hypotheses of charge symmetry and parity conservation, in this way one can grossly move the contribution of the combinatorial background off the data. The fitted spectrum is reported in Fig. 53. The scalar assignment of the first observation was superseded in Ref. [164] by the tensor identification, which at that time could appear more suggestive in the search of $\bar{N}N$ quasi-nuclear bound states [47]. Were this spin assignment confirmed, this state might be identified with the $f_2(1565)$, seen in a decay channel different from $(\pi^+\pi^-)$ (see Section 6.2).

However, in the following years, some more elaborated spin-parity analyses performed by Gaspero [166], based on a final state interaction approach, suggested again the quantum numbers $J^P = 0^+$. The Breit–Wigner function used to fit the data at best was considerably wider ($m = 1386$ MeV,

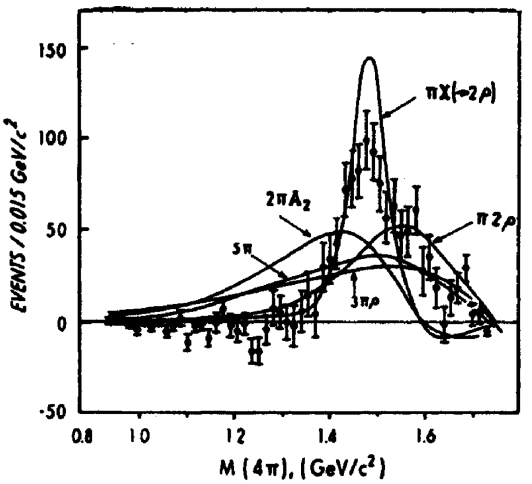

Fig. 53. Difference spectrum (difference between the spectra for the $(2\pi^+2\pi^-)$ and $(3\pi^-\pi^+)$ systems) for the $\bar{p}n \to 3\pi^-2\pi^+$ reaction, from Ref. [164]. The curves superimposed represent some fits to the data under several hypotheses, explained in the original reference.

$\Gamma = 310$ MeV), and the $(\sigma\sigma)$ decay channel played a dominant role. In Ref. [166] the decay branching ratio for this channel is reported to be 61%.

Nonetheless, the possibility that this huge resonance could be given by the superimposition of more than one state was put forward, as the analyses on three pion final states started to point out the existence of new structures in the same mass region, as already mentioned in Section 6.2.

The total statistics collected by OBELIX in this channel amounts to 26271 exclusive events, with $\bar{n}$ momentum up to 405 MeV/c, selected as already described for the exclusive three pion sample, mainly by applying the 4C kinematic fit. The estimated annihilation cross section for this channel, with $p_{\bar{n}}$ up to 405 MeV/c, is $\sigma_{ann} = (10.76 \pm 0.60)$ mb. The invariant mass of the $(\pi^+\pi^+\pi^-\pi^-)$ system for these data is reported in Fig. 54; the superimposed hatched histogram corresponds to pure phase space Monte Carlo events, expected in absence of any dynamic effect. The deviation of the experimental spectrum shape from the Monte Carlo one is evident, therefore an analysis in terms of resonant amplitudes is mandatory.

First analyses of partial samples confirmed the issues of Ref. [166], at least as far as the mass, the width and the spin of the large resonance are concerned [123,124]. About the decays, the branching fraction for the $(\sigma\sigma)$ channel is of course very sensitive to the parametrization chosen for the $(\pi\pi)$ interaction. In Ref. [166] a phenomenological parametrization of the available $(\pi\pi)$ phase shifts and inelasticities was applied; it can be considered accurate enough to reproduce the features of the two low mass $(\pi\pi)$ non resonant systems in which a 4π bound state might decay.

A broad state of this kind, at about 1400 MeV, can easily be identified with the $f_0(1370)$. The nature and the real features of this meson are anyhow not very clear, as it is in general always reported together with a very wide background-like cloud, known in general as $f_0(400–1200)$. On the other hand, if the $f_0(1500)$ is really a glueball, it should show up somehow even in the 4π decay channel. Therefore, some attempts were made to understand whether the large structure in the 4π mass spectrum could be explained as the superimposition of (at least) two scalar signals.

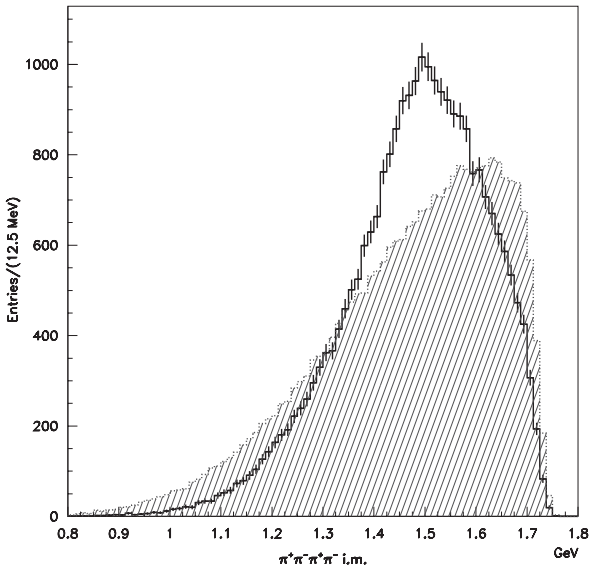

Fig. 54. Plot with errors: invariant mass spectrum of the $(\pi^+\pi^+\pi^-\pi^-)$ system for $\bar{n}p \to 3\pi^+2\pi^-$ exclusive events collected by OBELIX. Hatched histogram: same invariant mass distribution for pure phase space Monte Carlo events.

The most convincing proof for the existence of a $f_0(1500) \to 4\pi$ decay channel was given by Crystal Barrel [167,168], especially in the analysis of the $\bar{p}d \to \pi^- 4\pi^0 p_s$ annihilation at rest, where only one $4\pi^0$ combination is possible [167]. Using for the σ state the K-matrix parameters out of the three-body final state analyses, a narrower $f_0(1370)$ was found (with $m = 1395$ MeV and $\Gamma = 275$ MeV), as well as a second scalar state fully compatible with the $f_0(1500)$ features ($m = (1490 \pm 30)$ MeV, $\Gamma = (140 \pm 40)$ MeV). Both have dominant $(\sigma\sigma)$ decay, but while $f_0(1370)$ decays almost exclusively in four pions, for $f_0(1500)$ the 4π decay mode accounts just for half its total width. An important contribution is given as well by the $(\pi(1300)\pi)$ decay mode of both the resonant states (especially of $f_0(1500)$). With these resonances parameters a satisfactory fit can be obtained for the $\bar{p}p \to 5\pi^0$ channel as well, whose analysis is harder due to the large combinatorics.

Even in the $\bar{n}p \to 3\pi^+2\pi^-$ channel the combinatoric background is rather huge; moreover, more initial states must be included due to the in-flight annihilation pattern, bringing another complication to the analysis. In the most recent reanalyses [125], the broad resonance found in Ref. [124] with $(m, \Gamma) = ((1359 \pm 17), (425 \pm 30))$ MeV and dominant $(\sigma\sigma)$ decay splits into two states as well, the heavier of which is again fully compatible with the $f_0(1500)$. Preliminary results indicate that $(\pi(1300)\pi)$ is its favorite decay channel. A sizeable contribution is played by single ρ^0 production, recoiling against a σ system.

The possibility of existence, besides the dominant scalar amplitude, of a tensor signal at high mass values was tested as well. The reason was that in a first analyzed sample, with $\bar{n}$ momentum up to 300 MeV/c, a narrow structure seemed to emerge in the difference spectrum at about 1640 MeV, see Fig. 55 [120,123,144].

A rough analysis of the decay angles for events belonging to the mass slice around 1600 MeV pointed out a slight preference for a spin 2 resonance [123], to which a fit by a non-interfering

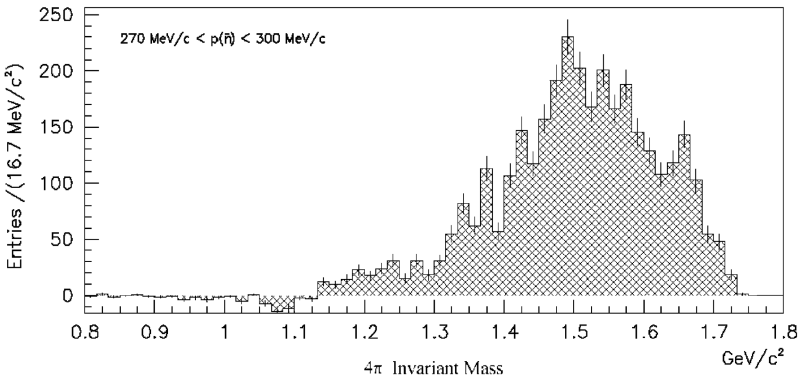

Fig. 55. Observation of an enhancement toward 1600 MeV in the five pions difference spectrum, OBELIX data selected in the $\bar{n}$ momentum range (270–300) MeV/c. From Ref. [144].

Breit–Wigner assigned the values $m=(1647\pm7)$ MeV, $\Gamma=(58\pm20)$ MeV. Some interest raised about it since two previous observations had been made for a narrow state in the same mass region, by GAMS [169] and by VES [170] in the $\omega\omega$ decay channel. Yet, with more statistics, and increasing the maximum $\bar{n}$ momentum, the signal faded away. The possibility that it could have been overwhelmed by the huge hadronic background and the tails of other resonances was tested adding a spin two resonance amplitude in the fit, but the hypothesis was rejected, both in the regions around 1600 and 1250 MeV (the latter was tested to check a possible 4π decay of the $f_2(1270)$). It seems plausible that the signal observed for $p_{\bar{n}} < 300$ MeV/c is, most likely, a statistical fluctuation.

6.5. Hints on annihilation into final states with kaons

The statistics collected by the OBELIX experiment could allow to perform for the first time ever some qualitative studies about the properties of specific final states with the presence of one or more kaons. Unfortunately the number of events surviving the selection cuts is too little to allow a complete spin-parity analysis to study the features of the resonances produced in the intermediate states.

As already mentioned, no other samples for the following reactions may be found in the literature. Only for $\bar{n}p \to K^+K^-\pi^+$ some issues of the charge-conjugated reactions $\bar{p}n \to K\bar{K}\pi$ on deuterium exist [171,172].

The $\bar{n}p \to K^+K^-\pi^+$ reaction provides perhaps the most interesting hints as, in spite of the limited statistics, a clear indication for the presence of a narrow state around 1500 MeV has been obtained. The observation of a clear di-kaon decay mode of the $f_0(1500)$ is of particular importance, to shed light on its decay pattern and confirm the flavor-blindness properties it should exhibit, were it a *glueball*. Fig. 56 reports the invariant mass of the (K^+K^-) system, for a sample of 241 events selected out of 1.29×10^6 three prong events by imposing very tight cuts, requiring both kaons to be identified by means of dE/dx and/or TOF measurements.

The bump at about 1500 MeV may be considered as one of the cleanest examples of a possible $f_0(1500)$ decay into two kaons. This plot ought to be compared to the analogous one obtained with $\bar{p}p \to K^+K^-\pi^0$ annihilation data, shown in Fig. 57 and taken from Ref. [118]. In this case the sample

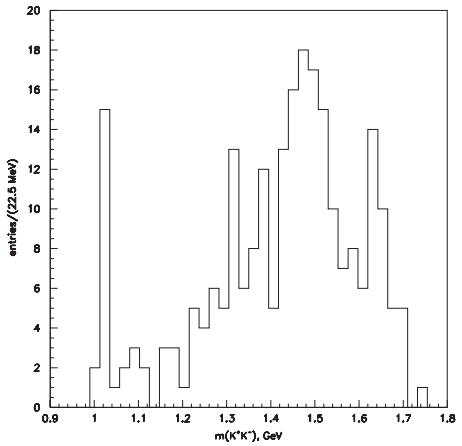

Fig. 56. Invariant mass of the (K^+K^-) system, with events with both kaons identified by means of OBELIX specific ionization and/or time of flight measurements. The peaks due to $\phi(1020)$ and possibly $f_0(1500)$ are clearly visible.

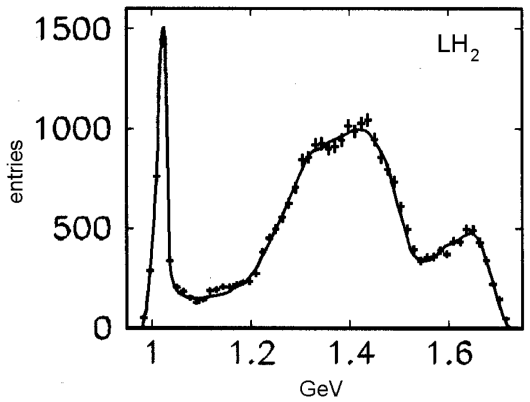

Fig. 57. Invariant mass of the (K^+K^-) system for the $\bar{p}p \to K^+K^-\pi^0$ reaction in liquid hydrogen target. OBELIX data, from Ref. [118]. The solid line represents the best fit to the spectrum.

was selected applying particle identification criteria for the two kaons, as well as a 1C kinematic fit to identify the missing π^0. The enhancement centered at about 1400 MeV is very broad. Even the narrow structure visible at about 1600 MeV, that can be probably identified with the $f_0(1720)$, corresponds to a much larger bump in the (K^+K^-) invariant mass spectrum obtained with the $\bar{p}$ data.

Using antineutron annihilation reactions one could moreover get some interesting additional hints about the features of the systems decaying into $\bar{K}K\pi$ (adding some new information to the long-debated E/ι puzzle [173]), with much stringent ties on the achievable quantum numbers. For instance, the $\bar{n}p \to K^{\pm}K^0_L\pi^{\mp}\pi^+$ annihilation proceeds only from P wave initial states, due to G-parity and isospin conservation. Therefore, an axial meson with $(K\bar{K}\pi)$ decay could be produced, recoiling against a π^+, only in $^3P_1$ and $^3P_2$ initial states, while a pseudoscalar meson could be produced

only in $^3P_1$. This could suggest that the observation of the axial meson might be favored at higher $\bar{n}$ momenta, where the probability of attaining an higher relative angular momentum between the meson and the recoiling pion is presumably larger. Unfortunately the statistics collected by OBELIX is not enough to draw any conclusion on this subject.

6.6. Issues of the search for narrow resonances in formation reactions: the $(3\pi^+2\pi^-\pi^0)$ case

The search for baryonium states had been one of the most appealing subjects in the study of $\bar{\mathcal{N}}\mathcal{N}$ interactions since the bubble chamber times [49,50]. Since the late Seventies a number of theoretical predictions had been suggesting the existence of narrow $\bar{\mathcal{N}}\mathcal{N}$ states, required for instance by $\bar{\mathcal{N}}\mathcal{N}$ potential models [174]. The observation in formation in $\bar{\mathcal{N}}\mathcal{N}$ annihilations of several candidates had been claimed, but none of them was confirmed by later experiments with larger statistics. A well known example is the $S(1936)$ [175], seen by some experiments as an enhancement, 3–20 MeV wide, in the $(\bar{p}p)$ total and annihilation cross section.

Evidences for states of this kind were suggested in $(\bar{n}p)$ and $(\bar{p}n)$ annihilations as well [176]; $(\bar{n}p)$ (and its charge conjugated reaction) could be particularly suitable to observe such states due to the isospin selection. Based on an analysis of the $(\bar{n}p)$ bubble chamber data, indirect indications for the existence of two isospin 1 states were found: a G_1 resonance at a mass (1986 ± 1) MeV, ~ 8 MeV wide, with dominant decay in channels with kaons, and a G_2 one at $m = (1975 \pm 1)$ MeV (width $\leqslant 2$ MeV), dominantly decaying in channels with an odd number of pions. The existence of the first resonance was inferred from the observation of a dip in the $(\bar{n}p)$ annihilation cross section at $p_{\bar{n}} = 0.685$ GeV/c. The G_2, on the contrary, was seen as a peak at $p_{\bar{n}} = 0.645$ GeV/c, that emerged more clearly when considering the ratio $r = \sigma(\bar{n}p \to \text{odd pions})/\sigma(\bar{n}p \to \text{even pions})$. Those observation were never ever confirmed due to the lack of $\bar{n}$ beams of enough energy.

OBELIX could perform indeed such measurements, but the maximum mass value for a possible $\bar{n}p$ system in this case is 1.92 GeV. In the mass window covered by OBELIX data, on the other hand, some evidences of new anomalies have been reported: the E687 experiment at FNAL observed, for instance, the presence of a dip in the mass spectrum of the $(3\pi^+3\pi^-)$ final state produced by diffractive photoproduction [177], reported in Fig. 58.

It was interpreted as generated by the destructive interference between the continuum background and a narrow resonant state, with $m = (1.91 \pm 0.04 \pm 0.01)$ GeV and $\Gamma = (29 \pm 11 \pm 4)$ MeV, to which the $J^{PC} = 1^{--}$, $G = +1$, $I = 1$ quantum numbers were assigned. Some signals of a similar activity were observed as well in the photoproduction of the 4π final state. Moreover, older observations of a dip with the same features were reported in $e^+e^- \to 6\pi$ by the DM2 experiment.

The formation of a similar object could be observed as well in the $\bar{n}p \to 3\pi^+2\pi^-\pi^0$ annihilation [178]. This final state can proceed from both $^3S_1$ and $^1P_1$ waves, so in the first case a 1^- object could in principle be formed. With $(\bar{n}p)$ annihilation in flight one must however take into account that the fractions of annihilations proceeding from each of the initial states vary as a function of energy, as already mentioned in Section 5.2. Given a decreasing trend for the annihilations from S-wave following Dover–Richard model, integrating over the $\bar{n}$ momentum spectrum and taking into account the population of hyperfine levels (supposedly statistical), a dominance of S-wave production of this final state is expected (about 80%). The analysis was performed applying the same method adopted by E687 to fit the distribution obtained by the ratio of the energy spectrum for $\bar{n}p \to 3\pi^+2\pi^-\pi^0$ exclusive events and the same spectrum obtained by all the available inclusive odd prong events

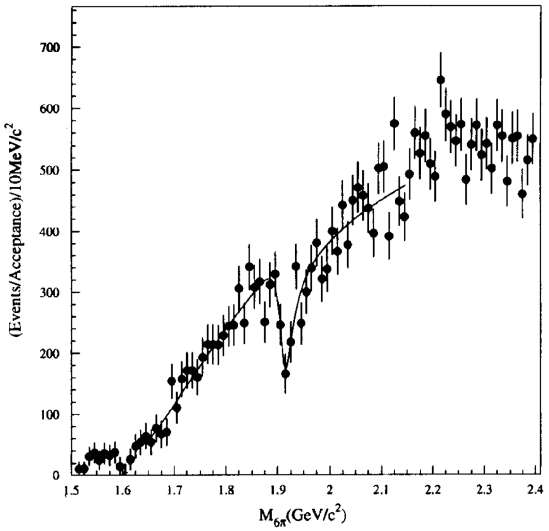

Fig. 58. 6π invariant mass for photoproduction events collected by the E687 experiment. From Ref. [177].

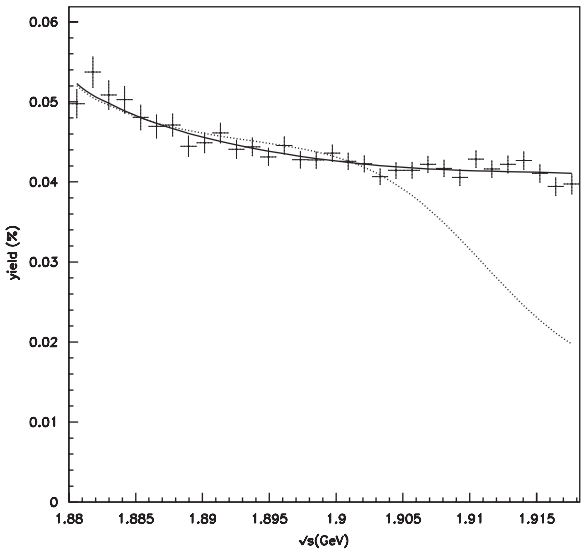

Fig. 59. Yield for $\bar{n}p \to 3\pi^+ 2\pi^- \pi^0$ events as a function of the total c.m. energy, normalized to the total number of inclusive three- and five-prong events. The line is the trend expected if a resonance with the parameters and weight as suggested by E687 is formed in the ($\bar{n}p$) annihilation. From Ref. [178].

(with more than three prongs). The "ratio" spectrum, that can be interpreted as a yield since the geometrical acceptances and efficiencies for the two samples are essentially the same, is shown in Fig. 59. The six pions exclusive data set was selected out of the five prong bulk by applying, as usual, proper energy-momentum cuts, as well as cuts on the missing mass distribution to single out

events with a single neutral pion and a 1C kinematic fit to test the $\bar{n}p \to 3\pi^+2\pi^-\pi^0$ hypothesis. With these selections, the residual background is at the level of 16%. The $\bar{n}p \to \omega 2\pi^+\pi^-$ events, which contribute to about 6%, have been removed from the sample.

The spectrum shows no particular deviation from a flat trend. Applying a model in compliance to E687 analysis to reproduce the data, one should expect a markedly decreasing distribution, as shown by the curve in the picture. A fit with a free weight to account for a possible contribution of the observed state excludes that it could account for more than 1.5% over the full spectrum, against a $\sim 31\%$ contribution quoted by E687. A similar flat trend is observed considering the exclusive channel $\bar{n}p \to 2\pi^+\pi^-\pi^0$.

The absence of a signal in this mass region of course does not disprove the anomaly observed by E687, as the underlying mechanism for its formation can be of completely different nature; moreover, in this case a different component of the $I = 1$ resonance multiplet should show up, and it might do it differently even because of the hadronic environment. However, its absence in $(\bar{n}p)$ data indicates that the dip observed in photoproduction cannot be identified as a form of baryonium.

6.7. *Summary of meson spectroscopy with* $\bar{n}$*'s*

From a general point of view one cannot state that $\bar{n}$'s may compete with $\bar{p}$'s in meson spectroscopy studies as far as results' completeness and, most of all, available statistics are concerned. Due to the different beams' flux intensities (of almost four order of magnitudes, even though sometimes the experimental limitation on the acquisition rates of the complex detectors used dumps this feature), the statistics that may be collected with $\bar{p}$ beams are much larger.

However in some cases it was shown (precisely, by OBELIX) that with $\bar{n}$ it is possible to achieve comparable or even better results as compared to $\bar{p}$'s, due to the peculiar cleanliness of the data, for final states composed by charged particles only. A typical example is the $\bar{n}p \to \pi^+\pi^+\pi^-$ channel, in which two important issues were observed. The analysis of the $(\pi^+\pi^-)$ invariant mass system showed some of the features of the neutral dipion system observed in the $\bar{p}p \to 3\pi^0$ annihilation at rest [140]. From a very careful analysis of the $3\pi^0$ Dalitz plot, composed by some 10^5 events, it was found that the signal corresponding to a peak centered around 1500 MeV was actually due to a superimposition of two states, a scalar and a tensor one. The same approach was followed in the analysis of the exclusive $\bar{n}p \to \pi^+\pi^+\pi^-$ data sample. This sample could moreover be distributed in sub-sets as a function of the $\bar{n}$ momentum. In all the cases the presence of both the 0^{++} and the 2^{++} states was required to get good fits, but the momentum dependence showed very clearly that the production intensity for the scalar state was flat, while for the tensor one it was increasing with $\bar{n}$ momentum, in agreement with the expectation that a momentum increase favors the production of higher spin states.

Another very interesting result was obtained by analyzing, in the same data sample, the $(\pi^+\pi^+)$ invariant mass spectrum. Statistical evidences for an isotensor scalar state at $M = (1420 \pm 20)$ MeV, with $\Gamma = (160 \pm 10)$ MeV, were found; a state of this kind should clearly have an exotic $(\bar{q}^2q^2)$ structure. The only, previous observations of a $I=2$ state, at 1600 MeV, were reported by experiments on $\gamma\gamma \to \rho\rho$.

The hypothesis that the scalar state observed at 1500 MeV could be a manifestation of the lightest glueball of the spectrum found several confirmations, since it had been observed, over the years, to decay into different channels. A many body decay for the $f_0(1500)$ has also been observed, as

was also shown in the analysis of the $\bar{n}p \to 3\pi^+2\pi^-$; the broad enhancement seen in the neutral 4π invariant mass system could accommodate both the $f_0(1500)$ signal, with a mass and width fully compatible with the values fixed from its two body decays, and, possibly, the $f_0(1370)$, whose decay in four pions seems to be favored.

The $\bar{n}p$ annihilation reactions studied by OBELIX, with $p_{\bar{n}}$ up to 405 MeV/c could cover, in formation, a total energy range of about 40 MeV. In this energy window, from 1.88 to 1.92 GeV, nothing in principle prevents the formation of a bound state, long sought for since bubble chambers times. Quite recently, right in this mass region, the E687 Experiment observed the presence of a narrow dip in 6π photoproduction events. OBELIX could not confirm the existence of such a state in $\bar{n}p \to 6\pi$ data, excluding that the signal observed by E687 might be a baryonium form.

7. Nuclear physics with antineutrons

There were no specific experiments designed to study the interaction of $\bar{n}$'s with nuclei, in spite of the advantage that the ($\bar{n}$-Nucleus) annihilation is simpler as compared to the ($\bar{p}$-Nucleus) one due to the absence of Coulomb interaction, which entails very important corrections to ($\bar{p}$-Nucleus) data in order to extract the hadronic contributions. The Coulomb corrections are not always easy to calculate in a precise way. Nonetheless, the difficulty of operating $\bar{n}$'s beams discouraged to perform specific ($\bar{n}$-Nucleus) experiments.

The information on ($\bar{n}$-Nucleus) interaction comes therefore from ancillary or parasitic measurements of other observables. Often in the literature some Authors report σ_{abs}, which includes, besides the dominant σ_{ann} for annihilation, also the contribution of other non-elastic processes, like charge exchange, inelastic scattering, nucleon knock-out. Since all these contributions amount only to a few percent of σ_{ann}, and are usually smaller than the quoted errors, we will use in the following σ_{ann} for simplicity.

The first measurement of σ_{ann} for $\bar{n}$ on C was performed by Gunderson et al. [20]. The choice of C was determined by the circumstance that they needed the value of $\sigma_{ann}(\bar{n}C)$ in order to extract $\sigma_{ann}(\bar{n}p)$ by means of a subtraction technique, from the transmission through the heptane-based liquid scintillator target. Data were collected at four momenta and are affected by very large errors (70% at the lower momentum).

There is a considerable amount of data on Fe (natural isotopic composition), without any particular nuclear physics argument for such a preference, but simply because Iron was a favorite converter in the monitors and detectors described in Sections 2.4 and 2.5. A first determination of σ_{ann} on Fe at 220 MeV/c, with a $\sim 70\%$ error was given by Brückner et al. [23].

A quite complete and reliable determination of $\sigma_{ann}(\bar{n}Fe)$ from 100 to 531 MeV/c was performed by Agnello et al. [179] by a clever analysis of the logarithmic decrease of the $\bar{n}$ annihilation stars in the 10-layered $\bar{n}$ monitor of PS178 Experiment [35], in 11 different $\bar{n}$ momentum bands. The errors are of the order of 15–25% and this is the first reliable measurement of ($\bar{n}$-Nucleus) interaction. The data could be well fitted to a simple expression $\sigma_{ann}[\text{barn}] = a + b/p_{lab}$ (with p_{lab} in GeV/c), with $a = (0.891 \pm 0.168)$ barn and $b = (0.233 \pm 0.036)$ barn $\cdot$ GeV/c, with a χ^2 of 0.298 (C.L. > 0.995). By comparing $\sigma_{ann}(\bar{n}Fe)$ with a proper average of $\sigma_{ann}(\bar{n}\mathcal{N})$, the Authors found that a A^x scaling law with $x = (0.614 \pm 0.033)$, consistent with $A^{2/3}$, gave a good representation of the data over the full momentum range. The $\bar{n}$ annihilation was essentially a surface process, as expected.

In a later paper the PS178 Collaboration [180] presented an analysis of the multiplicity and angular distribution of charged pions emitted following $\bar{n}$ annihilation on Fe, in the momentum range (100–531) MeV/c. The average charged pion multiplicity $\langle N_{\pi^\pm} \rangle$ was ~ 2.85, constant with the $\bar{n}$ momentum and somehow lower than the elementary ($\bar{n}\mathcal{N}$) averaged multiplicity. The angular distributions at the different momenta show similar behaviors: an increase of the number of tracks in the forward direction, a slight depletion around $\theta = \pi/2$, a slight rise in the backward direction. Both observations are consistent with a dominant $\bar{n}\mathcal{N} \to m\pi$ annihilation mechanism, suggested by the $\sim A^{2/3}$ scaling law.

The method introduced by Agnello et al. [180] was applied later even by Barbina et al. [181], PS199 Experiment, to analyze the logarithmic decrease of the number of reconstructed annihilations in the series of Iron converters of the PS199 $\bar{n}$ detectors described in Section 2.5. They measured the ($\bar{n}$Fe) absorption cross section in the momentum interval between 125 and 780 MeV/c, obtaining a good description of the data by means of a $\sigma_{\text{ann}} = a + b/p_{\bar{n}}$ law, with $a = (0.680 \pm 0.051)$ barn and $b = (0.228 \pm 0.024)$ barn $\cdot$ GeV/c.

All σ_{ann} and parametrizations mentioned so far are shown in the figures in the following section.

7.1. The annihilation cross section of antineutrons in nuclei

Only $\sim 30\%$ of the $\bar{n}$'s produced by the PT of OBELIX annihilated in the central LH_2 target, producing the bulk of data presented in Sections 3–5. It was then decided to put a second disk-shaped, solid, nuclear target at a distance of ~ 30 cm from the center of the LH_2 one.

The method was first tested with the earlier version of the $\bar{n}$ beam (LH_2 PT 15 cm long, $p_{\bar{p}} = 313$ MeV/c), and with the LH_2 RT empty. 2×10^4 annihilation events were collected with targets of C, Al, Cu, Sn and Pb (natural isotopic composition). The data followed a clear $A^{2/3}$ scaling law. We will not discuss them here, since they are embedded in the ~ 50 times larger statistics data bank discussed in the following. Details on such measurements can be found in Ref. [182].

The encouraging results obtained by this first experiment convinced the OBELIX Collaboration to put a nuclear target downstream the LH_2 RT during all $\bar{n}$ data taking runs. Events corresponding to annihilations in the LH_2 target or in the nuclear target could be easily recognized thanks to the vertex reconstruction (see Fig. 60).

In this way more than 10^7 raw annihilation events on targets of C, Al, Cu, Ag, Sn and Pb nuclear targets could be collected. A careful analysis of these events allowed a systematic and precise study of σ_{ann} in Nuclei, whose results were presented in detail in Ref. [24,183,184].

Fig. 61 represents a three-dimensional plot of the measured $\sigma_{\text{ann}}(p_{\bar{n}}, A)$, as a function of $p_{\bar{n}}$ and A. The data show a smooth behavior everywhere; the lines represent the projection of the best-fit surface described in the following for values $A = \text{const}$, $p_{\bar{n}} = \text{const}$ corresponding to the experimental data.

The whole data set has been fitted to the expression:

$$\sigma_{\text{ann}}(p_{\bar{n}}, A) = \sigma_0(p_{\bar{n}}) A^x \tag{23}$$

in which the different contributions have been considered as independent and have thus been factorized. Following previous experiments [179,181] a power scaling law has been assumed for the A dependence, while for the momentum dependence the functions

$$\sigma_0(p_{\bar{n}}) = a + b/p_{\bar{n}} \tag{24}$$

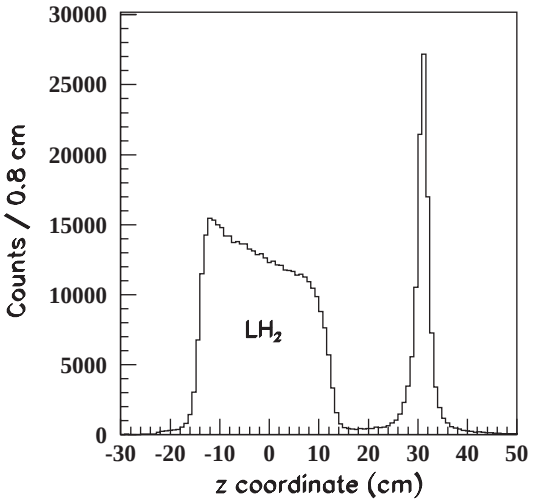

Fig. 60. Distribution of the annihilation vertex z-coordinate for data taken with LH_2 and Ag nuclear targets in series, OBELIX Experiment. The tower from -14 to $+14$ cm, with exponentially decreasing top, is due to annihilations in the LH_2 target, the peak centered at 30 cm to annihilations in the Ag target. From Ref. [24].

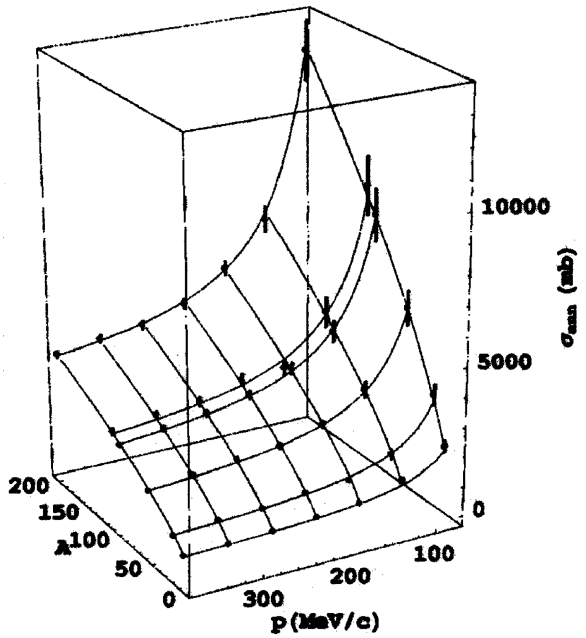

Fig. 61. Three-dimensional plot of the measured $\sigma_{\mathrm{ann}}(p_{\bar{n}}, A)$, as a function of $p_{\bar{n}}$ and A. The lines represent the projection of the best-fit surface (23) with the momentum dependence parametrization (24) for values A=const, $p_{\bar{n}}$=const corresponding to the experimental data. From Ref. [24].

Table 3
Parameters and reduced χ^2 of the fit of the cross section values to function (23) assuming for the momentum dependence functions (24) and (25), first and second column, respectively. From Ref. [24]

Parameter	Fit with Eq. (24)	Fit with Eq. (25)
a (mb)	66.5 ± 3.0	88.4 ± 4.7
b (mb MeV/c)	$(1.987 \pm 0.086) \times 10^4$	$(9.9 \pm 1.7) \times 10^3$
c (mb MeV$^2/c^2$)		$(9.9 \pm 1.6) \times 10^5$
x	0.6526 ± 0.0060	0.6515 ± 0.0053
χ^2	1.228	0.700

previously used in the literature [179,181] and

$$\sigma_0(p_{\bar{n}}) = a + b/p_{\bar{n}} + c/p_{\bar{n}}^2 \tag{25}$$

have been used.

The results of the fitting procedure are reported in Table 3, together with the reduced χ^2 value. We may see that both fits with formulas (24) and (25) can be considered acceptable, according to the χ^2 test laws. However, a closer inspection on how the two parametrizations describe the data indicates that the parametrization (25) is better. Anyway, independently on the chosen momentum parametrization $\sigma_0(p_{\bar{n}})$, the result of the fit indicates clearly that the A dependence is fully consistent (within 2%) with an $A^{2/3}$ scaling law over the whole momentum range (Fig. 61).

Since recent theoretical approaches [185–187] examined the possible behavior of σ_{ann} for $\bar{p}$ at low momenta (< 100 MeV/c) in complex nuclei, having at disposal for comparison the experimental σ_{ann} on Ne at $p_{\bar{p}} = 57$ MeV/c, affected however by a huge error (50% at 1σ), the A dependence was investigated more carefully—in particular to check whether the 50 MeV/c binning could mask some different trends, especially at low momenta. To this purpose a distribution over 10 MeV/c wide momentum bins was made and for each bin σ_{ann} was fitted to a $\sigma_{ann} = \sigma_0(p)A^x$ expression. The results are reported in Fig. 62. It appears that the values of x so obtained, obviously affected by errors larger than in the previous evaluation due to the larger statistical errors affecting each value of σ_{ann} in a 10 MeV/c bin, are nicely distributed across a weighted mean value $x = (0.651 \pm 0.004)$, compatible with the results of the above described fits, without any indication of anomalous trends in the full momentum range. It is possible to conclude that an $A^{2/3}$ scaling law describes, within 2%, the full set of data, showing that the $\bar{n}$ annihilation process in complex nuclei is purely a surface effect down to $p_{\bar{n}} = 50$ MeV/c, in agreement to the fact that the $\bar{N}$ annihilation is a localized hadronic interaction with a high cross section.

A further confirmation of this hypothesis may be inferred from a direct comparison between the A-scaled cross section data and an appropriate sum over the elementary ($\bar{n}n$) and ($\bar{n}p$) annihilation cross sections, $\sigma_{ann}^{\bar{n}n}(p_{\bar{n}})$ and $\sigma_{ann}^{\bar{n}p}(p_{\bar{n}})$. To this purpose the parametrization of $\sigma_{ann}^{\bar{n}p}(p_{\bar{n}})$ deduced from the experimental data in Ref. [57] was used while the best fits to the ($\bar{p}p$) annihilation data from Ref. [89] ($p_{\bar{p}} > 180$ MeV/c) and from Ref. [76] ($p_{\bar{p}} < 180$ MeV/c) have been used to parametrize $\sigma_{ann}^{\bar{n}n}(p_{\bar{n}})$, obviously assuming charge symmetry. Fig. 63a shows how the fits to $\sigma_{ann}^{\bar{n}p}(p_{\bar{n}})$ and to $\sigma_{ann}^{\bar{n}n}(p_{\bar{n}})$ compare with the scaled cross section $\sigma_0(p_{\bar{n}})$. The points represent the weighted mean value obtained from the six measured scaled cross section, and the line labelled by (3) the fit corresponding to the parametrization (25).

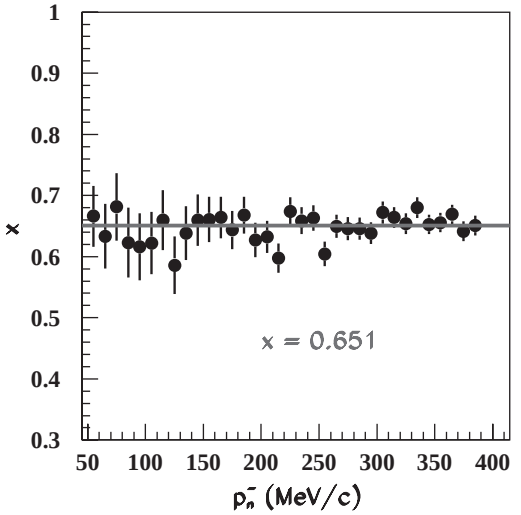

Fig. 62. Exponent expressing the dependence of the ($\bar{n}$-Nucleus) annihilation cross section on the target mass number, $\sigma_{ann} = \sigma_0(p)A^x$, evaluated for 10 MeV/$c$ wide bins of the incoming $\bar{n}$ momentum. The horizontal line indicates the weighted mean value $x = (0.651 \pm 0.004)$. From Ref. [24].

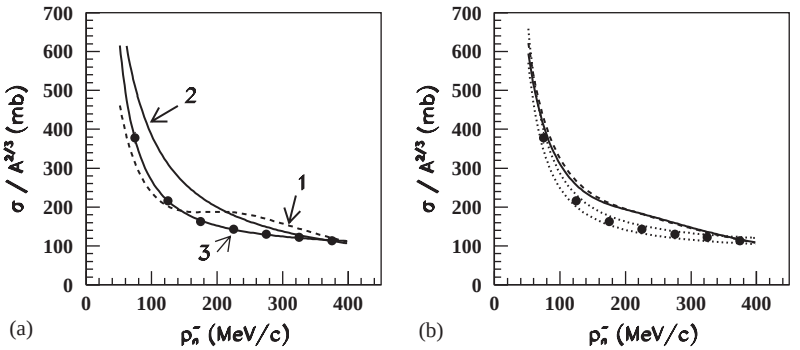

Fig. 63. (a) Comparison among the $A^{2/3}$ scaled cross section data of Ref. [24], averaged over the six nuclei (points), and the elementary ($\bar{n}$p) (curve 1) and ($\bar{n}$n) (curve 2) cross section parametrizations; curve 3 represents the momentum dependence as in formula (25) for scaled data. (b) Comparison among $A^{2/3}$ scaled cross section data of Ref. [24], averaged over the six nuclei (points) and the sum $\alpha\sigma^{\bar{n}p}_{ann}(p_{\bar{n}}) + (1-\alpha)\sigma^{\bar{n}n}_{ann}(p_{\bar{n}})$ for $\alpha = 0.5$ (dashed curve) and 0.4 (solid curve); the dotted band represent the uncertitude in the normalization of all $\sigma_{ann}(p_{\bar{n}}, A)$. From Ref. [24].

The weighted mean of the cross sections deduced in Ref. [24] can be more meaningfully compared to the sum $\alpha\sigma^{\bar{n}p}_{ann}(p_{\bar{n}}) + (1-\alpha)\sigma^{\bar{n}n}_{ann}(p_{\bar{n}})$, where α ($\alpha = Z/A$) may assume the two extreme values 0.5 (carbon) and 0.4 (lead). The comparison is shown in Fig. 63b, in which the dashed line represents the sum for α=0.5, the continuous one for $\alpha = 0.4$ and the dotted band represents the uncertainty in the normalization of all $\sigma_{ann}(p_{\bar{n}}, A)$.

We remark that there is an overall agreement within 20% between the experimental values and the predicted one. We believe that it can be considered satisfactory, if we take into account that

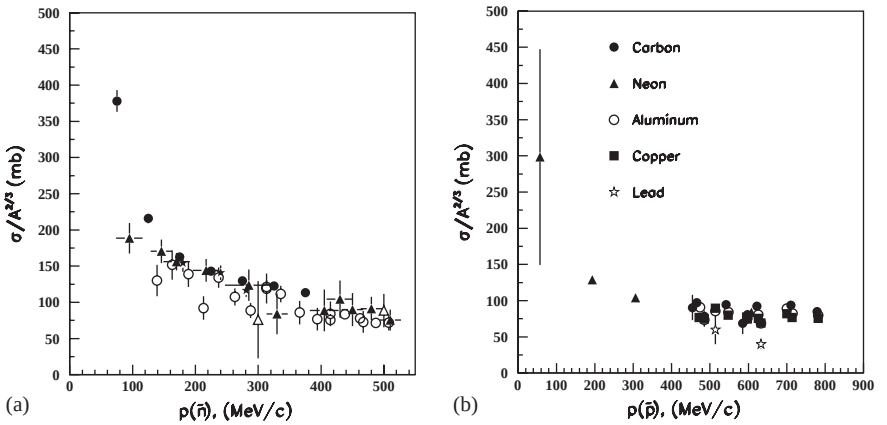

Fig. 64. (a) Comparison among the $A^{2/3}$ scaled cross section data of Ref. [24], averaged over the six nuclei (full circles), and previous results, scaled too. The experimental points are from the following references: Open circles: Barbina et al., Ref. [181]; Full stars: Ableev et al., Ref. [182]; Full triangles: Agnello et al., Ref. [179]; Open triangles: Gunderson et al., Ref. [20]. For the data of Ableev et al. [182] the weighted mean values of the scaled cross section have been plotted. All data are reported with statistical and systematic errors added quadratically. (b) $A^{2/3}$ scaled cross section data for the ($\bar{p}$-Nucleus) annihilation process in the momentum interval below 800 MeV/c. The experimental points are from the following references: full circles, carbon: Agnew et al. [188], Aihara et al. [189], Nakamura et al. [190]; full triangles, neon: Balestra et al. [191], Bianconi et al. [192]; open circles, aluminum: Aihara et al. [189], Nakamura et al. [190], Ashford et al. [193]; full squares, copper: Aihara et al. [189], Nakamura et al. [190], Ashford et al. [193]; open stars, lead: Ashford et al. [193]. Both pictures are from Ref. [24].

all nuclear structure effects, like Fermi motion of nucleons, shadowing, different values of α at the surface of the nucleus, where the interaction occurs, have not been considered.

In Fig. 64a the results of Ref. [24] are compared with the previous ones reported in the literature [20,179,181,182]. The comparison is done on the scaled cross section, since different targets were used in different experiments. For the data of Ableev et al. [182] the weighted mean values of the scaled cross section have been plotted. A general agreement within 20% is observed. It can be considered acceptable, if we take into account the fact that the measurements were performed with quite different experimental techniques and that all the other experiments had a lower limit on $p_{\bar{n}}$ at about 100 MeV/c. The major discrepancy occurs for the scaled value of Ref. [24] below 100 MeV/c and that by Agnello et al. ($\sim 30\%$) [179].

In Fig. 64b we report the ($\bar{p}$-Nucleus) scaled cross section data available below 800 MeV/c. The scarcity of data in the momentum region covered by OBELIX is evident: there are only three data points on Ne. On the contrary, there are several measurements in the momentum range (500–800) MeV/c, showing a quite flat behavior around a value of (70–80) mb, consistent with the value of the $\bar{n}$ scaled cross sections at 500 MeV/c.

In Fig. 65 the $p_{\bar{n}}$ parametrizations given by Agnello et al. [179], Barbina et al. [181] and Astrua et al. [24] are reported. The upper and lower lines of the same type are representative of the errors in the parameters given by Refs. [179,181] and by the normalization errors affecting the parametrization of Ref. [24]. Again a general agreement within 20% is observed.

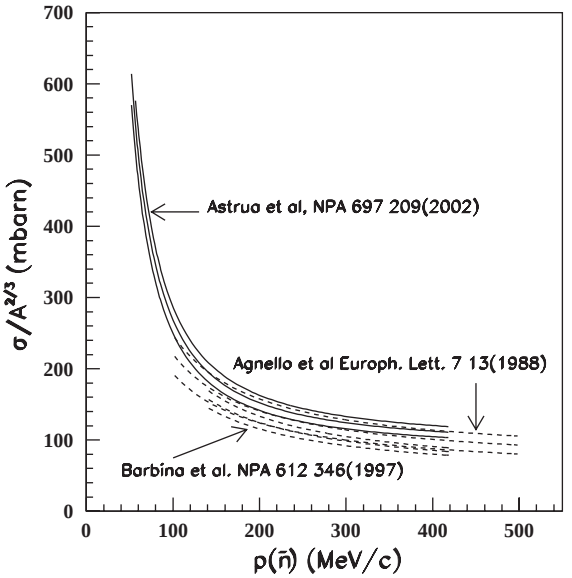

Fig. 65. Comparison among the momentum dependence best parametrization of Ref. [24] for $A^{2/3}$ scaled $\sigma_{\mathrm{ann}}(p_{\bar{n}}, A)$ (continuous lines) and those available in literature for Fe target, scaled too: Agnello et al. [179] (dotted lines) and Barbina et al. [181] (dashed lines). Upper and lower lines of the same type are representative of the errors in the parameters given by Refs. [179,181] and by the normalization errors affecting the parametrization (25). From Ref. [24].

The full bulk of data is represented very well by a simple parametrization in which the A dependence is, within 2%, consistent with $A^{2/3}$ and the $p_{\bar{n}}$ dependence, is represented within 20%, by a weighted sum of the measured elementary cross sections for ($\bar{n}$p) and ($\bar{n}$n) annihilation processes. This behavior is well consistent with the picture that, as a consequence of the fact that the ($\bar{\mathcal{N}}$ Nucleus) annihilation is a well localized interaction on a single nucleon with a large cross section ($\sim$ 200 mb), the nucleus behaves as a simple assembly of independent nucleons. Only the surface nucleons contribute to the interaction and the interaction of the nucleons is quite the same as in free space. In some sense this process can be considered as a textbook example of simple nuclear physics.

7.2. Inclusive particle spectra following antineutron annihilation in nuclei

OBELIX was not very well suited to study the spectra of all particles emitted in the $\bar{n}$ annihilation.

The annihilation products in Nuclei can be distinguished in primary products, which are the mesons produced in the elementary $\bar{\mathcal{N}}\mathcal{N}$ annihilation, and secondary products which are the emitted protons (p), deuterons (d) and the other nuclear fragments coming from the interaction of the primary products with the residual nucleus. In OBELIX the charged products of the annihilation could be identified using the relationship between the velocity β and the momentum; only particles as light as π's, K's, protons and deuterons could be recognized, because the apparatus was not designed to detect heavier nuclear fragments: just inclusive information could thus be obtained. Furthermore, for $\bar{n}$ annihilation studies massive solid targets were used, and they introduced the necessity of

Table 4
Average knock-out p kinetic energy T_0 evaluated by exponential and Maxwell–Boltzmann fit of the experimental kinetic energy spectra. From Ref. [195]

	C	Al	Cu	Ag	Pb
T_0 (MeV) exp. fit	95.70 ± 0.08	91.09 ± 0.10	88.97 ± 0.06	86.84 ± 0.08	83.30 ± 0.11
T_0 (MeV) MB fit	77.27 ± 0.13	73.91 ± 0.15	72.48 ± 0.10	71.23 ± 0.11	68.87 ± 0.16

important corrections on the spectra, as well as of different detection thresholds. A further difficulty was related to the eccentric position of the nuclear target. Results of partial analyses may be found in Refs. [183,194,195].

Concerning the primary products, the ratio of their total number to the total number of annihilations, i.e. the multiplicity over the whole detected momentum range, is constant with A (or slightly decreasing as if due to an increasing energy loss). The π and K production seems thus to scale as $A^{2/3}$, as expected for a surface production reaction: in fact, π absorption processes on $\mathcal{N}$ leading to Δ formation, highly probable because of the mean momentum of the emitted π's, and its subsequent decay, affect only slightly their total number. No strangeness production enhancement is observed: the K/π ratio turns out to be $\sim 3\%$, very similar to the value for free $\bar{\mathcal{N}}\mathcal{N}$ annihilation, and it does not vary with A; also the K^+/K^- ratio, reflecting the influence of the final state interaction, is constant with A. The inclusive momentum spectra have been obtained for both primary and secondary products; the statistics for K's and d's is poorer than for π's and p's and the distortion and the low momentum cuts imposed by the detector acceptance are quite important: ~ 100 MeV/c for π's, ~ 200 MeV/c for K's, ~ 350 MeV/c for p's and ~ 400 MeV/c for d's; the measured spectra for π^+'s and π^-'s reflect the different behavior of the total $(\pi^+\mathcal{N})$ and $(\pi^-\mathcal{N})$ cross sections between ~ 200 and ~ 500 MeV/c.

Concerning the secondary products, the overall multiplicity shows an increasing and saturating trend of the production of p and d with A, signature of a not surface origin. The d/p ratio is (3–4)%, less than the values reported in literature (10–15% [196,197]) for $\bar{p}$ annihilation in nuclei, and it is probably due to the low-energy cuts.

The p kinetic energy spectra are affected by the detector acceptance distortion below ~ 80 MeV, so only the high energy contribution from direct π-$\mathcal{N}$ knock-out was considered, neglecting the low energy evaporation effect. A statistical analysis of these spectra was made by fitting the high energy decreasing tail with exponential and Maxwell–Boltzmann—like functions, aiming to determine the average energy of the emitted p's [195]. Table 4 reports the evaluated average energy values for the two different parametrizations: a decreasing trend with A is present in both the cases but the exponential fit introduces a mean increase of ~ 20 MeV with respect to the Maxwell–Boltzmann one.

The reduction of T_0 could be interpreted in terms of a larger number of interactions of the primordial π's with p's, of a higher proton binding energy or of a larger scattering probability for the emitted proton with A increase. This simple statistical analysis accounts quite satisfactorily for the data and the Maxwell–Boltzmann parametrization seems to be preferable. Comparing T_0 values by OBELIX with those available in literature [196–199], a fair agreement is found with Refs. [199] and [196] for the exponential fit and with Ref. [198] for the Maxwell–Boltzmann one, while Ref. [197] underestimates T_0 of ~ 30 MeV.

The multiplicity distributions per annihilation event have been evaluated as well: for d's and K's no A dependence is evident while for π's a slightly decreasing trend could be seen (~ 5–6%) for A varying from 12 to 207, complementary to a slight increase for p's, as if increasing the nucleon number in the target the fraction of high energy π's knocking-out a high energy proton could increase as well.

In conclusion, not surprising results were found from the analysis of the inclusive spectra: it was confirmed that the $\bar{n}$ annihilation on a Nucleus is a surface process occurring on single nucleons.

7.3. Summary of nuclear physics with $\bar{n}$'s

Nuclear physics results obtained with $\bar{n}$'s did not show unexpected or puzzling results. The systematic measurement of the total annihilation cross section and charged particle spectra performed by OBELIX is the most complete and precise achieved up to now, and is also superior to the total amount of data collected on $\bar{p}$ annihilation in nuclei. The data bank of OBELIX spans the full mass number range (from 12 to 206) over the 50–405 MeV/c momentum range. This data set is very well parametrized by a simple scaling law, indicating that the annihilation process is essentially a localized interaction on single nucleons at the nucleus surface. However we feel that this data bank must be the reference one for any microscopic theoretical calculation aiming to describe $\bar{\mathcal{N}}$-Nucleus interaction.

8. Main achievements in antineutron physics and future perspectives

8.1. Summary of main achievements in antineutron physics

We report here the main physics results, summarized more in detail at the end of each of the previous sections, obtained by the experiments, and in particular by OBELIX, exploiting $\bar{n}$ beams.

The most important observation in the analysis of the $(\bar{n}p)$ total and annihilation cross sections is the presence of a dip in σ_T at about 80 MeV, with a statistical significance of $\sim 3.5\sigma$, not present in σ_{ann}, and attributable to a dip in the elastic $(\bar{n}p)$ cross section. The presence of structures in $\bar{\mathcal{N}}\mathcal{N}$, both total and annihilation, cross sections was searched for by several Groups, in particular at low momenta, as a signature of quasi-nuclear $(\bar{\mathcal{N}}\mathcal{N})$ states. However no experiment except OBELIX was able to perform a scan below 100 MeV/c. The possibility that the dip might be due to systematic effects seems to be excluded by the techniques applied for each measurement, different and independent for $\sigma_T(\bar{n}p)$ and for $\sigma_{\text{ann}}(\bar{n}p)$. The fact that the dip appears in $\sigma_{el}(\bar{n}p)$ and not in $\sigma_{\text{ann}}(\bar{n}p)$ excludes the possibility that it might be due to a near-threshold resonance in the $I=1$ $(\bar{\mathcal{N}}\mathcal{N})$ system. A naive explanation can be given resorting to the Ramsauer–Townsend effect for low energy elastic scattering of electron off atoms.

The most interesting results obtained by OBELIX in the study of two-body $\bar{n}p$ annihilation is the clear-cut observation of a strong dynamical selection rule for the $(\phi\pi^+)$ channel which strongly violates (a factor of ~ 35) the OZI rule, which generally applies to hadron interactions. The $\bar{n}p \to \phi\pi^+$ annihilation proceeds only ($\geqslant 98\%$) from the $^3S_1$ initial state, and not from the $^1P_1$ which in principle is not forbidden by general selection rules. The presence of such a dynamical selection rule is particularly evident by observing the decreasing trend of the cross section as a function of the

S-wave content in the initial state. Further evidence is provided by the shape of the angular distributions. We remark that no other experiment measured the $\bar{p}p \to \phi\pi^0$ annihilation channel with $\bar{p}$'s in flight. An interesting explanation for such an effect is provided by the hypothesis of the presence of $(\bar{s}s)$ pairs in the nucleon wave function, already confirmed at higher energies by experiments on deep inelastic scattering of leptons off nucleons. A mechanism involving $(\bar{s}s)$ rearrangement explains well the experimental observations.

The most interesting and unexpected result obtained by OBELIX with $\bar{n}$'s in the meson spectroscopy field is the statistical evidence for an $I = 2$ state, established by a careful analysis of the $\bar{n}p \to \pi^+\pi^+\pi^-$ channel. The observation of such a state is out of reach for antiproton induced reactions in final states with few pions. The result could be achieved in this case even thanks to the extreme cleanliness of the large sample of collected events, selected through a powerful 4C kinematic fit, which reduced the background to a few 10^{-3}—in other measurements performed by OBELIX and by other experiments with $\bar{p}$'s the background level for events surviving kinematic fit (usually 1C) cuts was one or even two orders of magnitude larger. The new state required by the maximum likelihood fits, with $M = (1420 \pm 20)$ MeV and 160 MeV wide, is only compatible with an exotic nature $(\bar{q}\bar{q}qq)$. The only previous observation for an $I = 2$ state of similar nature, at 1600 MeV, was reported in $\gamma\gamma$ interactions at DESY.

Also the study of the behavior of the two resonances observed in the $(\pi^+\pi^-)$ invariant mass system (f_0 at 1500 MeV and f_2 at 1565 MeV) delivered very interesting results. Both the states were found to contribute to the bump observed at around 1500 MeV. A different production trend for the two resonant states was observed as a function of $\bar{n}$ momentum, flat for f_0, increasing for f_2, compatible to expectations. The measurement of a modulation of the production intensities as a function of the available energy was a unique result, in this momentum region.

Further studies of $\bar{n}p$ annihilations in many pions showed that the $f_0(1500)$ is a good candidate as the lightest glueball, since its decay into four pions, anambiguosly observed in $\bar{n}p$ annihilations, adds to the several decay modes already known.

Finally, the data bank for $\bar{n}$-Nucleus annihilation provided by OBELIX is by far the most complete in the A and in the $\bar{n}$ momentum range under examination. Analogous data with $\bar{p}$'s are scarce, of poor statistics and obtained on a limited number of targets, mainly at low A. No anomalous behavior or trends were found. We believe that this data bank will be the reference one for any further microscopic theoretical investigation on ($\bar{N}$-Nucleus) interaction.

8.2. Perspectives of antineutron physics at future machines

After this survey on the nice and interesting results achieved so far in $\bar{n}$ physics, it is useful to propose some suggestions for the future taking into account the problems still left open and the potentialities at new machines which are under construction or discussed for approval. Looking at the present results, there are at least three items that deserve further experimental efforts for their physics potential.

The first one is a direct measurement of $d\sigma/d\Omega$ for elastic scattering of $\bar{n}$ off protons, from 200 (or at least 100) MeV/c down to $\sim$ 30 MeV/c. The physics interest is to confirm the existence of the dip–bump structure around 80 MeV/c, and understand its origin with a careful analysis of the differential cross sections. The experiment is relatively simple and unexpensive. A scheme of principle to perform such a measurement was already sketched in Ref. [18], but we think that it is

perhaps too simplified to perform clean measurements. We believe that the best way would be to use the tagged $\bar{n}$ beam technique [21], with $\bar{p}$'s of $\sim 200\,\mathrm{MeV}/c$ stopping in a ~ 3 cm thick LH_2 target. Another LH_2 target, some cm thick and with a diameter of (15–20) cm, could be used as scatterer. The $\bar{n}$ would be detected by a tracking calorimeter like those described in Section 2.5. Due to the low energies involved, all distances could be quite reduced to ~ 1 m, still ensuring a good selection of the energies by TOF. A compact neutron detector made of scintillating fibres headed on multianode PM's could be the best solution for localizing the neutrons with a precision of some mm, i.e. one order of magnitude better the one achieved in Ref. [26]. In the same experiment also $\sigma_T(\bar{n}p)$ could be measured parasitically, for calibration with the previous data. The whole data taking period would not exceed a few weeks.

The second experiment that would be useful to perform in a systematic way is a measurement of $\sigma_{ann}(\bar{n}p)$ from $\sim 700\,\mathrm{MeV}/c$ down to $\sim 50\,\mathrm{MeV}/c$, possibly with the same detector and at the same time of a $\sigma_{ann}(\bar{p}p)$ measurement. The physics reason is a determination of their ratio, and consequently of the ratio $\sigma_{ann}(I=0)/\sigma_{ann}(I=1)$, that does not appear to be monotonic as one could expect; there is however a suspect that this behavior could just be an effect of the combination of the results of at least three different experiments. The set-up to detect the $\bar{N}$ annihilations in a H_2 target is quite obviously non-magnetic, with the only requirement of a good angular coverage (at least 2π). Differences in the charged prong annihilation frequencies between $\bar{n}$ and $\bar{p}$ can be quite easily accounted for by accurate Monte Carlo simulations and calibrations. More care must be devoted to the beam that should ideally impinge (be it a $\bar{p}$'s or $\bar{n}$'s one) on the same Reaction Target in the detector. While for the $\bar{p}$ beam there are obviously no problems, for the $\bar{n}$ beam a ~ 3 cm thick LH_2 Production Target would be installed some meters upstream the Reaction Target, surrounded by suitable arrays of scintillators for trigger. With a filled production target the $\bar{n}$ beam could be obtained by CEX at 0°. Rates of a few $\bar{n}/10^6$ $\bar{p}$ may be expected from 700 to $\sim 200\,\mathrm{MeV}/c$. The non-interacting $\bar{p}$ beam must be swept out from the target by a magnet. At $\sim 200\,\mathrm{MeV}/c$ the $\bar{p}$ would stop in the target and provide a beam of characteristics similar to those described in Section 2.

For the reaction target in the detector, a unique LH_2 target ~ 1 cm thick could be used both for $\bar{p}$ and $\bar{n}$, down to $\sim 200\,\mathrm{MeV}/c$. At lower energies, gaseous H_2 targets would be considered, due to the $\bar{p}$ energy loss in the target.

Even such a measurement would not be so much time-consuming, apart from the time required for the changes and tuning of the incident $\bar{p}$ momentum values at the machines.

Finally, in the meson spectroscopy field, the hints for very clear spectra that may be expected with kaons in the final state suggest for a continuation of such an effort. This would require a more intense $\bar{n}$ beam, by at least a factor of 10, and a powerful magnetic detector (like the old OBELIX or Crystal Barrel) for the detection of all the annihilation products.

Let us now briefly remind where the $\bar{p}$ beams necessary to produce $\bar{n}$'s could be available in the future. The most ambitious facility foreseen for the future for Hadron Physics is the Japan Hadron Joint project (JHJ). It was initially proposed as an accelerator complex at the KEK site (Tsukuba) consisting of a 200 MeV Linac, a 3 GeV synchrotron and a 50 GeV synchrotron, the last ones providing high intensity proton beams of 0.6 and 0.5 MW power respectively, used for the production of various secondary particle beams [200]. The project was afterwards merged into a joint project KEK–JAERI, with some modifications, mainly linked to the increased power required by JAERI for the study of nuclear transmutation and other items relevant to Nuclear Engineering.

The site was moved from Tsukuba to the JAERI laboratory at Tokai and further modifications were done on the design of the accelerator complex due to space limitations. The project was staged into two Phases, and Phase I was approved with a construction budget starting on April 1, 2001. It is expected that Phase I will be completed in 2006 and provide first beams in April 2007. Phase I of the accelerator complex consists of a 400 MeV Linac, a 3 GeV Proton Synchrotron and a 50 GeV one with a beam power of 0.75 MW (0.15 μA). Budget constraints allow only a limited number of experiments for the slow-extracted proton beams in the initial experimental Hall, which is only half as long as the final one.

In Phase I there are no $\bar{p}$ beams explicitly mentioned; the main emphasis is on kaon beams. There is however the intention of operating $\bar{p}$ in Phase II, using the cooling techniques pioneered at CERN LEAR. Actually, the magnets of the dismantled Antiproton Accumulator were already sent from CERN to Japan just in view of their future use.

Another major Accelerator Facility for Beams of Ions and Antiprotons was recently proposed as a big extension of the present UNILAC/SIS complex at G.S.I. (Darmstadt, Germany). The accelerators complex as well as the physics program are considerably different from those at the JHJ. The heart of the proposed new facility is a double ring synchrotron of 100–200 Tm (SIS 100/200), with a system of associated storage rings for beam collection, cooling, phase space optimization and experimentation. Large use of innovative technologies (rapidly cycling superconducting magnets, electron cooling at high energies) is foreseen. There will be a large variety of beams delivered by this facility to different users communities (ion beams, 25 GeV/u Au, radioactive beams, antiproton beams) [201].

The conceptual design of the facility for the production, accumulation and acceleration of antiprotons is basically determined by the luminosity requirements for antiproton–proton collisions in the proposed high energy storage ring HESR. The design is aimed at a luminosity of 2×10^{32} cm^{-2} s^{-1} for collisions between stored and cooled $\bar{p}$'s (from 0.8 to 14.5 GeV) and an internal Hydrogen gas or pellet target. This goal corresponds to a $\bar{p}$ consumption rate of 2×10^{7} s^{-1}, which has to be compensated by a corresponding net rate of $\bar{p}$ accumulation. Among the rings foreseen to this purpose, one of them, called NESR (new experimental storage ring) could be used for experiments with low-energy $\bar{p}$'s in an external target area. The intensity of this beam is expected to be larger than the LEAR one: in this case all the experiments previously mentioned could be effectively performed.

References

[1] B. Cork, et al., Phys. Rev. 104 (1956) 1193. ***
[2] O. Chamberlain, et al., Phys. Rev. 100 (1955) 947.
[3] P.S. Eastman, et al., Nucl. Phys. B 51 (1973) 57.
[4] C.B. Dover, et al., Prog. Part. Nucl. Phys. 29 (1992) 87. ***
[5] T. Ueda, Prog. Theor. Phys. 72 (1979) 1670.
[6] T. Bressani, B. Minetti, in: U. Gastaldi, R. Klapisch (Eds.), Physics at LEAR with Low-Energy Cooled Antiprotons, Plenum Press, N.Y. and London, 1984, p. 781.
[7] M. Cresti, et al., Phys. Lett. B 177 (1986) 206.
[8] M. Cresti, et al., Phys. Lett. B 200 (erratum) (1986) 587.
[9] K. Hagiwara, et al., Phys. Rev. D 66 (2002) 010001.

[10] T. Bressani, F. Iazzi, in: C. Amsler, D. Urner (Eds.), Physics at SUPERLEAR, Institute of Physics Conference Series No. 124, Bristol, 1992, p. 193.
[11] C. Amsler, Phys. Lett. B 541 (2002) 22.
[12] T. Bressani et al., in: U. Gastaldi, R. Klapisch, J.M. Richard, J. Tran Thanh Van (Eds.), Physics with Antiprotons at LEAR in the ACOL Era, Frontières, Gif-sur-Yvette, 1988, p. 265.
[13] L. Pinsky, in: U. Gastaldi, R. Klapisch, J.M. Richard, J. Tran Thanh Van (Eds.), Physics with Antiprotons at LEAR in the ACOL Era, Frontières, Gif-sur-Yvette, 1988, p. 275.
[14] L. Pinsky, in: C. Amsler, et al., (Eds.), Physics at LEAR with Low Energy Antiprotons, Harwood Academic Publishers, Chur, 1988, p. 255.
[15] T. Bressani, in: S. Costa, G. Orlandini, C. Schaerf (Eds.), Proceedings of the VII Course of the International School of Intermediate Energy Nuclear Physics, World Scientific, Singapore, 1992, p. 313.
[16] A. Adamo, et al., Nucl. Phys. A 553 (1993) 651c.
[17] F. Iazzi, in: M.C. Birse, G.D. Lafferty, J.A. McGovern (Eds.), HADRON'95 Proceedings, World Scientific Publishing Co. Pte. Ltd, Singapore, 1996, p. 99.
[18] S. Marcello, Nucl. Phys. A 655 (1999) 107c.
[19] T. Brando, et al., Nucl. Instr. and Meth. 180 (1981) 461.
[20] B. Gunderson, et al., Phys. Rev. D 23 (1981) 587.
[21] L. Cugusi, et al., Nucl. Instr. and Meth. A 270 (1988) 354. ***
[22] R.P. Hamilton, et al., Phys. Rev. Lett. 44 (1980) 1179.
[23] W. Brückner, et al., Phys. Lett. B 169 (1987) 569. ***
[24] M. Astrua, et al., Nucl. Phys. A 697 (2002) 209. ***
[25] K. Nakamura, et al., Phys. Rev. Lett. 53 (1984) 885.
[26] M.P. Macciotta, et al., IEEE Trans. Nucl. Sci. NS-33 (1986) 374.
[27] T. Bressani, et al., in: C. Amsler, et al., (Eds.), Physics at LEAR with Low Energy Antiprotons, Harwood Academic Publishers, Chur, 1988, p. 267.
[28] T. Armstrong, et al., Phys. Rev. D 36 (1987) 659. ***
[29] R. Armenteros et al., Proposal CERN/PSSC/86-A (1986).
[30] M. Agnello, et al., Nucl. Instr. Meth. A 399 (1997) 11. ***
[31] A. Adamo et al., Sov. J. Nucl. Phys. 55 (11) 1732.
[32] H. Gordon, et al., Nucl. Instr. Meth. 196 (1982) 303.
[33] F. Iazzi, in: T. Bressani, F. Iazzi, G. Pauli (Eds.), Proceedings of the 1st Workshop on Intense Hadron Facilities and Antiproton Physics, Torino, 1989. (SIF Conference Proceedings 26 Compositori, Bologna, 1990, p. 171).
[34] T. Bressani, et al., IEEE Trans. Nucl. Sci. NS-32 (1985) 733.
[35] T. Bressani, et al., Nucl. Instr. and Meth. A 292 (1990) 563. **
[36] M. Baldo-Ceolin, et al., Z. Phys. C 63 (1994) 409.
[37] K. Nakamura, et al., Phys. Rev. C 31 (1985) 31.
[38] A. Antonelli, et al., Nucl. Instr. and Meth. A 337 (1993) 34.
[39] A. Martin, et al., Nucl. Instr. and Meth. A 346 (1994) 257.
[40] R. Birsa, et al., Nucl. Phys. B 403 (1993) 25.
[41] M. Lamanna, et al., Nucl. Phys. B 434 (1995) 27.
[42] E. Fermi, Prog. Theor. Phys. 5 (1950) 570.
[43] C. Ghesquiére et al., in: Symposium on $N\bar{N}$ Interactions, CERN 74-18, Geneva, 1974.
[44] W.H. Barkas, et al., Phys. Rev. 105 (1957) 1037.
[45] C.J. Hamer, Nuovo Cimento 12A (1972) 162.
[46] R.A. Bryan, R.J.N. Phillips, Nucl. Phys. B 5 (1968) 201.
[47] C.B. Dover, et al., Phys. Rev. C 43 (1991) 379.
[48] J. Côté, et al., Phys. Rev. Lett. 48 (1982) 1319.
[49] J.M. Richard, Nucl. Phys. B Proc. Suppl. 86 (2000) 361.
[50] J.M. Richard, in: T. Bressani, A. Feliciello, A. Filippi (Eds.), Proceedings of the Workshop on Hadron Spectroscopy, Frascati (1999); Frascati Physics Series 15 (1999) 413.
[51] C.B. Dover, J.M. Richard, Phys. Rev. C 21 (1980) 1466. **
[52] M.A. Alberg, et al., Phys. Rev. D 27 (1983) 536.

[53] M. Kohno, W. Weise, Nucl. Phys. A 454 (1986) 429. **
[54] B.O. Kerbikov, et al., Sov. Phys. Usp. 32 (1989) 739.
[55] C. Amsler, F. Myhrer, Annu. Rev. Nucl. Part. Sci. 41 (1991) 219.
[56] J. Mahalanabis, et al., Nucl. Phys. A 485 (1988) 546. **
[57] A. Bertin, et al., Nucl. Phys. B (Proc. Suppl.) 56A (1997) 227. **
[58] W.W. Buck, et al., Ann. Phys. 121 (1979) 70.
[59] C.B. Dover, J.M. Richard, Ann. Phys. 130 (1980) 70.
[60] C.B. Dover, et al., Ann. Phys. 130 (1980) 70.
[61] T. Armstrong, et al., Phys. Lett. B 175 (1986) 383.
[62] OBELIX Collaboration, F. Iazzi, et al., Phys. Lett. B 475 (2000) 378. ***
[63] D.V. Bugg, et al., Phys. Lett. B 194 (1987) 563.
[64] F. Iazzi, Nucl. Phys. A 654 (1999) 505c.
[65] OBELIX Collaboration, A. Feliciello, Nucl. Phys. 655A (1999) 224c.
[66] F. Balestra, et al., Nucl. Phys. A 481 (1989) 572.
[67] Bombay-CERN-Neuchâtel-Tokyo Collaboration, R. Hamatsu, et al., Nucl. Phys. B 137 (1978) 283.
[68] Bombay-Chandigarh-Jammu-Tokyo Collaboration, S. Banerjee, et al., Z. Phys. C 28 (1985) 163.
[69] Bombay-Chandigarh-Jammu-Tokyo Collaboration, S. Banerjee, et al., Z. Phys. C 32 (1986) 163. **
[70] G.S. Mutchler, et al., Phys. Rev. D 38 (1988) 742. *
[71] E. Amaldi, E. Fermi, Phys. Rev. 50 (1936) 899.
[72] E. Fermi, La Ric. Sci. 7 (1936) 13.
[73] T.E. Kalogeropoulos, G.S. Tzanakos, Phys. Rev. C 17 (1980) 215.
[74] H.J. Pirner, et al., Z. Phys. A 338 (1991) 111.
[75] I.L. Grach, et al., Sov. J. Nucl. Phys. 48 (1988) 546.
[76] A. Zenoni, et al., Phys. Lett. B 461 (1999) 405.
[77] L.R.B. Elton, Introductory Nuclear Theory, Sir Isaac Pitman and Sons Ltd., London, 1959.
[78] C. Ramsauer, Ann. Phys. 66 (1921) 542.
[79] N.F. Mott, H.S.W. Massey, Theory of Atomic Collisions, 2nd Edition, Clarendon Press, Oxford, 1950, p. 201
[80] J.M. Peterson, Phys. Rev. 125 (1962) 955.
[81] T. Bressani, in: J. Bediaga, J. Miranda, A. Reis (Eds.), Proceedings V Conference on Heavy Quarks at Fixed Targets, Frascati Physics Series, Vol. 20, 2001, pp. 363 **.
[82] W. Brückner, et al., Phys. Lett. B 166 (1986) 113.
[83] W. Brückner, et al., Phys. Lett. B 158 (1985) 180.
[84] D.E. Caro, et al., Nucl. Phys. B 90 (1975) 221.
[85] S.J. Orfanidis, V. Rittenberg, Nucl. Phys. B 59 (1973) 570.
[86] OBELIX Collaboration, A. Bertin, et al., Phys. Lett. B 410 (1997) 344. ***
[87] OBELIX Collaboration, A. Filippi, et al., Nucl. Phys. A 655 (1999) 453. ***
[88] OBELIX Collaboration, A. Filippi, et al., Phys. Lett. B 471 (1999) 263. ***
[89] W. Brückner, et al., Z. Phys. A 335 (1990) 217.
[90] C. Batty, Nucl. Phys. A 601 (1996) 425.
[91] OBELIX Collaboration, G. Bendiscioli, et al., Nucl. Phys. A 686 (2001) 317.
[92] A. Filippi, Nucl. Phys. A 691 (2001) 336c. *
[93] S. Okubo, Phys. Lett. B 188 (1981) 317.
[94] G. Zweig, CERN Report 8419/TH412, 1964.
[95] I. Iizuka, Prog. Theor. Phys. Supp. 37–38 (1966) 21.
[96] OBELIX Collaboration, V.G. Ableev, et al., Phys. Lett. B 334 (1994) 237.
[97] ASTERIX Collaboration, J. Reifenröther, et al., Phys. Lett. B 267 (1991) 299.
[98] Crystal Barrel Collaboration, C. Amsler, et al., Nucl. Phys. A 594 (1995) 375.
[99] A. Filippi, Acta Phys. Polonica B 31 (2000) 2459.
[100] R. Bizzarri, et al., Nucl. Phys. B 14 (1969) 169.
[101] F. Gilman, R. Kauffman, Phys. Rev. D 36 (1987) 2761.
[102] Crystal Barrel Collaboration, C. Amsler, et al., Phys. Lett. B 294 (1992) 1732.
[103] A. Filippi, Nucl. Phys. A 655 (1999) 167c.

[104] J. Vandermeulen, Z. Phys. C 37 (1988) 563.
[105] OBELIX Collaboration, A. Alberico, et al., Phys. Lett. B 438 (1998) 430.
[106] OBELIX Collaboration, A. Bertin, et al., Phys. Lett. B 338 (1996) 450.
[107] C.B. Dover, P.M. Fishbane, Phys. Rev. Lett. 62 (1989) 2917.
[108] S.I. Bityukov et al., IFVE OEF 86-242.
[109] M.P. Locher, et al., Z. Phys. A 347 (1994) 281.
[110] M.P. Locher, et al., Z. Phys. A 351 (1995) 83.
[111] D. Buzatu, et al., Phys. Lett. B 329 (1994) 143.
[112] J. Ellis, et al., Phys. Lett. B 353 (1995) 319.
[113] J. Ellis, et al., Nucl. Phys. A 673 (2000) 256.
[114] V.E. Markushin, Eur. Phys. J. A 8 (2000) 389.
[115] OBELIX Collaboration, V. Alberico, et al., Phys. Lett. B 438 (1998) 430.
[116] Crystal Barrel Collaboration, C. Amsler, et al., Eur. Phys. J. C 23 (2002) 29.
[117] P.D. Barnes, et al., Phys. Rev. C 54 (1996) 2831.
[118] OBELIX Collaboration, A. Alberico, et al., Phys. Lett. B 438 (1998) 430.
[119] S. Godfrey, J. Napolitano, Rev. Mod. Phys. 71 (1999) 1411.
[120] A. Adamo, et al., Phys. Lett. B 368 (1992) 368. ∗
[121] OBELIX Collaboration, A. Bertin, et al., Phys. Rev. D 57 (1998) 55. ∗∗∗
[122] OBELIX Collaboration, A. Filippi, et al., Phys. Lett. B 495 (2000) 284. ∗∗∗
[123] OBELIX Collaboration, A. Adamo, et al., Nucl. Phys. A 558 (1993) 13c. ∗∗
[124] OBELIX Collaboration, V. Ableev, et al., in: M.C. Birse, G.D. Lafferty, J.A. McGovern (Eds.), HADRON'95 Proceedings, World Scientific Publishing Co. Pte. Ltd., Singapore, 1996, p. 337. ∗
[125] OBELIX Collaboration, A. Filippi, in: D. Amelin, A.M. Zaitsev (Eds.), Hadron Spectroscopy: Ninth International Conference, Protvino, 2001, American Institute of Physics, 2002, p. 582 ∗.
[126] K.M. Watson, Phys. Rev. 88 (1952) 1163.
[127] G. Veneziano, Nuovo Cimento 47A (1967) 642.
[128] For a general review on Veneziano model applications, see: A.B. Kaidalov, Sov. Phys.-Usp. 14 (1972) 600.
[129] Ch. Lovelace, Phys. Lett. B 26 (1968) 264.
[130] G. Altarelli, H.R. Rubinstein, Phys. Rev. 183 (1969) 1469.
[131] P. Anninos, et al., Phys. Rev. Lett. 20 (1968) 402.
[132] T.E. Kalogeropoulos, et al., Phys. Rev. D 24 (1981) 1759.
[133] ASTERIX Collaboration, B. May, et al., Phys. Lett. B 225 (1989) 450. ∗
[134] C. Zemach, Phys. Rev. 140 (1965) B97.
[135] C. Zemach, Phys. Rev. 140 (1965) B109.
[136] S.U. Chung, Spin formalisms, CERN Yellow Report CERN 71-8, 1971.
[137] V. Filippini, et al., Phys. Rev. D 51 (1995) 2247.
[138] Crystal Barrel Collaboration, E. Aker, et al., Phys. Rev. B 260 (1991) 249.
[139] A. Adamo, et al., Phys. Lett. B 287 (1992) 368.
[140] Crystal Barrel Collaboration, C. Amsler, et al., Phys. Lett. B 342 (1995) 433.
[141] OBELIX Collaboration, A. Bertin, et al., Phys. Lett. B 408 (1997) 476.
[142] Crystal Barrel Collaboration, C. Amsler, et al., Phys. Lett. B 355 (1995) 425.
[143] C. Amsler, F.E. Close, Phys. Lett. B 353 (1995) 385.
[144] OBELIX Collaboration, V.G. Ableev et al., in: G. Kernel, P. Krizan, M. Mikuz (Eds.), Proceedings of the Third Biennal Conference on Low-Energy Antiproton Physics, Bled (1994), World Scientific Singapore *, 1995, p. 75.
[145] S.U. Chung, et al., Ann. Phys. 4 (1995) 404.
[146] D.V. Bugg, et al., Nucl. Phys. B 471 (1996) 59.
[147] P. Salvini, Nucl. Phys. A 692 (2001) 340c, and references therein.
[148] T. Bressani, et al., Nuovo Cimento 103A (1990) 949.
[149] S.U. Chung et al., BNL preprint BNL-QGS-01-0501, 2001.
[150] B.A. Li, K.F. Liu, Phys. Rev. D 30 (1984) 613.
[151] Y. Uehara, et al., Nucl. Phys. A 606 (1996) 357.

[152] H. Albrecht, et al., Phys. Lett. B 217 (1989) 205.
[153] H.-J. Behrend, et al., Phys. Lett. B 218 (1989) 493.
[154] N.N. Achasov, et al., Z. Phys. C 27 (1985) 99.
[155] W. Hoogland, et al., Nucl. Phys. B 69 (1974) 266.
[156] A. Filippi, in: T. Bressani, A. Feliciello, A. Filippi (Eds.), Proceedings of the Workshop on Hadron Spectroscopy, Frascati, 1999; Frascati Physics Series, Vol. 15, 1999, p. 133.
[157] A. Filippi, in: G.G. Bonsignori, M. Bruno, A. Ventura, D. Vretenar (Eds.), Proceedings of the Bologna 2000 Conference, Structure of the Nucleus at the Dawn of the Century—Hadrons, Nuclei and Applications, World Scientific, Singapore, 2001, p. 150.
[158] A. Filippi, Nucl. Phys. A 692 (2001) 287c. ∗
[159] Crystal Barrel Collaboration, A. Abele, et al., Phys. Lett. B 450 (1999) 275.
[160] D.R. Thompson, et al., Phys. Rev. Lett. 79 (1997) 1630.
[161] Crystal Barrel Collaboration, A. Abele, et al., Phys. Lett. B 423 (1998) 175.
[162] Crystal Barrel Collaboration, A. Abele, et al., Phys. Lett. B 446 (1999) 349.
[163] A. Bettini, et al., Nuovo Cimento 42A (1996) 695.
[164] D. Bridges, et al., Phys. Rev. Lett. 56 (1986) 215.
[165] D. Bridges, et al., Phys. Rev. Lett. 57 (1986) 1534.
[166] M. Gaspero, Nucl. Phys. A 562 (1993) 407. ∗
[167] Crystal Barrel Collaboration, A. Abele, et al., Eur. Phys. J. 19 (2001) 667.
[168] Crystal Barrel Collaboration, A. Abele, et al., Eur. Phys. J. C 21 (2001) 261.
[169] D. Alde, et al., Phys. Lett. B 216 (1989) 451.
[170] G.M. Beladidze, et al., Z. Phys. C 54 (1992) 367.
[171] L. Gray, et al., Phys. Rev. D 27 (1983) 307.
[172] Crystal Barrel Collaboration, S. Wallis-Plachner, Nucl. Phys. A 692 (2001) 326c.
[173] A. Lanaro, Nucl. Phys. B (Proc. Suppl.) 56A (1997) 136.
[174] I.S. Shapiro, Phys. Rep. 35C (1978) 129.
[175] R.P. Hamilton, et al., Phys. Rev. Lett. 44 (1980) 1182.
[176] A. Subramanian, in: Proceedings of the 3rd European Symposium on Antinucleon–Nucleon Interactions, Stockholm, 1976, p. 51.
[177] E687 Collaboration, P.L. Frabetti, et al., Phys. Lett. B 514 (2001) 240.
[178] M. Agnello, et al., Phys. Lett. B 527 (2002) 39. ∗∗∗
[179] M. Agnello, et al., Europhys. Lett. 7 (1) (1988) 13.
[180] M. Agnello, et al., Nucl. Phys. A 516 (1990) 13.
[181] C. Barbina, et al., Nucl. Phys. A 612 (1997) 346.
[182] V.G. Ableev, et al., Nuovo Cimento 107A (1994) 943.
[183] E. Botta, Nucl. Phys. A 692 (2001) 39c.
[184] E. Botta, in: G.G. Bonsignori, M. Bruno, A. Ventura, D. Vretenar (Eds.), Proceedings of Bologna 2000 Conference, Structure of the Nucleus at the Dawn of the Century—Hadrons, Nuclei and Applications, World Scientific, Singapore, 2001, p. 158. ∗∗
[185] A. Bianconi, et al., Phys. Lett. B 483 (2000) 353.
[186] A. Gal, et al., Phys. Lett. B 491 (2000) 219.
[187] C.J. Batty, et al., Nucl. Phys. A 689 (2001) 721.
[188] L.E. Agnew, et al., Phys. Rev. 118 (1960) 1371.
[189] H. Aihara, et al., Nucl. Phys. A 360 (1981) 291.
[190] K. Nakamura, et al., Phys. Rev. Lett. 52 (1984) 731.
[191] F. Balestra, et al., Nucl. Phys. A 452 (1986) 573.
[192] A. Bianconi, et al., Phys. Lett. B 481 (2000) 194.
[193] V. Ashford, et al., Phys. Rev. C 31 (1985) 663.
[194] E. Botta, in: I. Iori, B. Moroni (Eds.), Proceedings of the XXXIX International Winter Meeting on Nuclear Physics, Ric. Scientifica ed Educazione Permanente (Suppl.) Vol. 117, 2001, p. 332.
[195] OBELIX Collaboration, E. Botta, in: E. Norman et al. (Eds.), Proceedings of the International Nuclear Physics Conference INPC2001, A.I.P. Conference Proceedings, 2001, p. 385.

[196] A.S. Sudov, et al., Nucl. Phys. A 554 (1993) 378.
[197] D. Polster, et al., Phys. Rev. C 51 (1995) 223.
[198] J. Riedlberger, et al., Phys. Rev. C 40 (1989) 2717.
[199] P. Hofman, et al., Nucl. Phys. A 512 (1990) 669.
[200] See, e.g. K. Imai, Nucl. Phys. A 691 (2001) 451c.
[201] An International Accelerator Facility for Beam of Ions and Antiprotons, Conceptual Design Report—GSI, 2001.